Cryo-electron microscopy structural studies of a bacterial multi-drug efflux pump involved in antibiotic resistance

Marie Glavier

To cite this version:

Marie Glavier. Cryo-electron microscopy structural studies of a bacterial multi-drug efflux pump involved in antibiotic resistance. Human health and pathology. Université de Bordeaux, 2018. English. NNT : 2018BORD0239 . tel-01961910

HAL Id: tel-01961910
https://theses.hal.science/tel-01961910

Submitted on 20 Dec 2018

THÈSE PRÉSENTÉE

POUR OBTENIR LE GRADE DE

DOCTEUR DE

L'UNIVERSITÉ DE BORDEAUX

ÉCOLE DOCTORALE DES SCIENCES DE LA VIE ET DE LA SANTÉ

SPÉCIALITÉ : BIOCHIMIE

Par Marie GLAVIER

Études structurales par cryo-microscopie électronique d'un système d'efflux multi-drogues bactérien, impliqué dans la résistance aux antibiotiques.

Cryo-electron microscopy structural studies of a bacterial multi-drug efflux pump involved in antibiotic resistance.

Sous la direction de : Laetitia DAURY

Soutenue le 26 Novembre 2018

Membres du jury :

M. PICARD, Martin	Directeur de Recherche	Université Paris Diderot	Rapporteur
M. LEVY, Daniel	Directeur de Recherche	Institut Curie	Rapporteur
Mme BAYER, Emmanuelle	Chargée de Recherche	Université de Bordeaux	Examinateur
M. GLEIZES, Pierre-Emmanuel	Professeur	Université de Toulouse	Président

Titre

Études structurales par cryo-microscopie électronique d’un système d’efflux multi-drogues bactérien, impliqué dans la résistance aux antibiotiques.

Résumé long

L'apparition croissante de bactéries pathogènes multi-résistantes à la plupart des antibiotiques disponibles apparaît comme un problème mondial de santé publique. Suite à leur découverte à la fin des années 1920, les antibiotiques ont été utilisés de manière efficace pour lutter contre les infections bactériennes. Malheureusement, un usage excessif à la fois en médecine humaine et animale a conduit à l’apparition de souches résistantes à la plupart des antibiotiques disponibles sur le marché, y compris pour les plus récents. Et, de plus, on observe aujourd’hui l’émergence de souches multi-résistantes dont le nombre ne cesse de croître ce qui pose un réel problème de santé publique.

Il est donc urgent de mieux comprendre les mécanismes mis en place par les bactéries pour résister aux antibiotiques afin de trouver des solutions pour combattre les souches multi-résistantes et également de limiter leur apparition. Dans ce contexte, le sujet de la thèse vise à mieux comprendre les bases moléculaires de l’efflux actif de drogues chez *Pseudomonas aeruginosa*, qui est un des plus importants mécanismes utilisés par la bactérie pour lutter contre l’action de plusieurs antibiotiques. *Pseudomonas aeruginosa* est un pathogène opportuniste qui engendre de nombreuses maladies nosocomiales, notamment, chez les patients atteints par la mucoviscidose. Les systèmes d’efflux forment des complexes

protéiques situés dans la paroi de la bactérie et expulsent de manière active une grande variété de composés dont les antibiotiques avant même qu'ils n'aient pu atteindre leur cible intracellulaire, les rendant ainsi inactif.

L'étude structurale se focalise sur le système RND (Resistance-Nodulation and cell Division) MexA-MexB-OprM qui est constitutivement exprimé chez la bactérie sauvage et est surexprimé chez les souches résistantes. Ce complexe tripartite est reconnu comme étant un système prototypique des systèmes tripartites, composé d'un transporteur inséré dans la membrane interne, d'une protéine canal insérée dans la membrane externe et d'une protéine adaptatrice périplasmique. Cette dernière relie les deux autres protéines pour former un conduit étanche traversant le périplasme et ainsi permettant d'expulser l'antibiotique à l'extérieur de la bactérie. Pour mieux comprendre le mécanisme d'efflux, il est nécessaire de déterminer la structure de ce complexe tripartite dont on a qu'une connaissance partielle. En effet, bien que la structure de chaque partenaire MexA, MexB et OprM ait été déterminée par cristallographie des rayons X, la structure du complexe entier n'est pas encore accessible car sa purification s'avère jusqu'à lors infructueuse. Face à cette difficulté à obtenir le complexe entier, l'objectif de la thèse a été de développer une stratégie originale pour reconstituer *in vitro* le complexe entier dans un environnement lipidique à partir des trois composants natifs produits séparément.

Les deux protéines transmembranaires, MexB et OprM ont été insérées dans deux minidisques lipidiques appelé Nanodisque qui miment la bicouche lipidique et dont la taille est contrôlée par une protéine de ceinture. L'assemblage du complexe tripartite est réalisé en mélangeant MexB et OprM en Nanodisque avec MexA. La caractérisation structurale de ce complexe tripartite a été réalisée par cryo microscopie électronique qui est la méthode de choix pour déterminer la structure des protéines à des résolutions quasi atomiques. La spécificité de cet échantillon a nécessité une mise au point fine des conditions de préparation des grilles de microscopie et l'optimisation des collectes d'images sur différents types de microscopes électroniques haute résolution. L'approche dite des particules isolées a été utilisée pour déterminer la structure tridimensionnelle (3D) du complexe à l'aide de plusieurs logiciels d'analyse d'images. A l'issue d'un protocole classique d'analyse, un volume 3D a été calculé avec une résolution inférieure à 4 Å ce qui a permis de construire un modèle atomique du complexe tripartite assemblé entre deux Nanodisques lipidiques.

Le complexe tripartite est composé d'OprM formant un trimère, de MexB formant également un trimère et de MexA formant un hexamère autour de MexB et en interaction avec OprM. Cette stœchiométrie 3 :6 :3 a également été observée pour un système tripartite homologue chez *E. coli* renforçant l'hypothèse d'un mode d'organisation conservé entre les espèces. Ces données ont permis de résoudre la structure complète de MexA dans le complexe qui s'avère différente de celle obtenue dans le cristal et aussi de résoudre la partie N-terminale jusqu'alors inconnue car trop flexible. De par l'organisation de MexA autour de MexB, ce segment N-terminal apparaît étendu et en contact avec la membrane lipidique du Nanodisque décrivant pour la première fois l'ancrage de MexA dans une membrane lipidique. Les changements conformationnels sont observés sur OprM et MexB lorsqu'ils sont engagés dans le complexe. OprM subit une importante modification conformationnelle avec l'ouverture de son extrémité périplasmique permettant une interaction bout à bout avec les domaines « hairpin » des six molécules de MexA. Comme pour OprM, les changements conformationnels de MexB résultent de l'interaction avec MexA mais sont cependant plus minimes et concernent principalement le basculement d'une boucle permettant d'établir un contact supplémentaire avec MexA.

Pour replacer cette structure tripartite dans le cycle d'efflux de l'antibiotique, celle-ci décrit un état qui s'apparente probablement à un état au repos, sachant qu'aucun ligand spécifique n'a été ajouté au cours de l'assemblage. De plus, étant donné la conformation ouverte d'OprM, le complexe forme un canal ouvert à son extrémité extracellulaire, fournissant le conduit pour évacuer les drogues pris en charge par le transporteur MexB qui utilise la force protomotrice comme source d'énergie.

Ce travail ouvre la perspective à des études structurales d'autres états conformationnels du système d'efflux en condition « énergisé » pour compléter la compréhension du mécanisme du cycle d'efflux. Par ailleurs, la connaissance de cette première structure du complexe natif tripartite constitue le premier pas vers le développement de molécules capables de bloquer l'assemblage du complexe à des fins thérapeutiques. En effet, de telles molécules inhiberaient l'efflux actif et restauraient l'efficacité perdue des antibiotiques actuels.

Mots clés

Cryo-microscopie électronique, Analyse d'image et reconstruction 3D, Systèmes d'efflux, Protéines membranaires, Nanodisques

Titre

Études structurales par cryo-microscopie électronique d’un système d’efflux multi-drogues bactérien, impliqué dans la résistance aux antibiotiques.

Résumé court

L'apparition croissante de bactéries pathogènes multi-résistantes à la plupart des antibiotiques disponibles apparaît comme un problème mondial de santé publique. Malheureusement, un usage excessif à la fois en médecine humaine et animale a conduit à l’apparition de souches multi-résistantes à la plupart des antibiotiques disponibles sur le marché. Il est donc urgent de mieux comprendre les mécanismes mis en place par les bactéries pour résister aux antibiotiques afin de trouver des solutions pour combattre les souches multi-résistances.

Dans ce contexte, le projet de la thèse vise à mieux comprendre les bases moléculaires de l’efflux actif de drogues chez *Pseudomonas aeruginosa*, qui est un des plus importants mécanismes utilisés par la bactérie pour lutter contre l’action de plusieurs antibiotiques. Les systèmes d’efflux forment des complexes protéiques situés dans la paroi de la bactérie et expulsent de manière active les antibiotiques avant même qu’ils aient pu atteindre leur cible intracellulaire, les rendant ainsi inactif.

L’étude structurale se focalise sur le système RND (Resistance-Nodulation and cell Division) MexA-MexB-OprM qui est constitutivement exprimé chez la bactérie sauvage et est surexprimé chez les souches résistantes. Ce complexe tripartite est composé d'un transporteur inséré dans la membrane interne, d'une protéine canal insérée dans la

membrane externe et d’une protéine adaptatrice périplasmique qui relie les deux autres protéines pour former un conduit étanche traversant le périplasme. En l’absence de la connaissance de la structure du complexe tripartite, l’objectif de la thèse a été de développer une stratégie originale pour reconstituer *in vitro* le complexe entier dans un environnement lipidique à partir des trois composants natifs produits séparément.

L’assemblage du complexe tripartite est réalisé en mélangeant MexB et OprM en Nanodisque avec MexA mimant les deux bicouches lipidiques. La structure de ce complexe tripartite a été obtenu en combinant la cryo microscopie électronique et à l’approche dite ‘des particules isolées’. La structure tridimensionnelle du complexe calculée à une résolution inférieure à 4 Å a permis de construire un modèle atomique du complexe tripartite assemblé entre deux Nanodisques.

Le complexe tripartite est composé d’un trimère d’OprM, d’un trimère de MexB et d’un hexamère de MexA entourant MexB et en interaction avec OprM. Ces données ont permis de résoudre la structure complète de MexA dans le complexe dont la partie N-terminale jusqu’alors inconnue car trop flexible et décrivent pour la première fois l’ancrage de MexA dans une membrane lipidique. Les changements conformationnels sont observés sur OprM et MexB lorsqu’ils sont engagés dans le complexe avec l’ouverture de l’extrémité périplasmique d’OprM et le basculement d’une boucle de MexB permettant d’établir un contact supplémentaire avec MexA.

Pour replacer cette structure tripartite dans le cycle d’efflux de l’antibiotique, celle-ci décrit un état qui s’apparente probablement à un état au repos, sachant qu’aucun ligand spécifique n’a été ajouté au cours de l’assemblage. De plus, le complexe forme un canal

ouvert à son extrémité extracellulaire, fournissant le conduit pour évacuer les drogues transportées par MexB qui utilise la force protomotrice comme source d'énergie.

Ce travail ouvre la perspective à des études structurales d'autres états conformationnels du système d'efflux en condition « énergisé » pour compléter la compréhension du mécanisme du cycle d'efflux. Par ailleurs, la connaissance de cette première structure du complexe natif tripartite constitue le premier pas vers le développement de molécules capables de bloquer l'assemblage du complexe à des fins thérapeutiques. En effet, de telles molécules inhiberaient l'efflux actif et restauraient l'efficacité perdue des antibiotiques actuels.

Mots clés

Cryo-microscopie électronique, Analyse d'image et reconstruction 3D, Systèmes d'efflux, Protéines membranaires, Nanodisques

Title

Cryo-electron microscopy structural studies of a bacterial multi-drug efflux pump involved in antibiotic resistance.

Short abstract

The increasing appearance of multi-drug-resistant pathogenic bacteria to most available antibiotics is emerging as a global public health problem. Unfortunately, excessive use in both human and animal medicine has led to the emergence of multi-drug-resistant strains for most antibiotics available on the market. It is therefore urgent to better understand the underlying mechanisms by which bacteria resist to antibiotics to combat multi-resistance strains. In this context, this work aims at better understanding the molecular basis of active drug efflux in Pseudomonas aeruginosa, which is one of the most important mechanisms used by the bacterium to resist to several antibiotics. Efflux systems form protein complexes in the bacterial wall and actively expel antibiotics even before they reach their intracellular target, rendering them inactive. The structural study focuses on the MexA-MexB-OprM RND (Resistance-Nodulation and cell Division) system that is constitutively expressed in wild-type bacteria and is over-expressed in resistant strains. This tripartite complex is composed of a transporter inserted into the inner membrane, a channel protein inserted in the outer membrane and a periplasmic adapter protein that connects the other two proteins to form a sealed conduit through the periplasm. In the absence of knowledge of the structure of the tripartite complex, the aim of the thesis was to develop an original strategy to reconstitute the whole complex *in vitro* in a lipid environment from the three native components produced separately.

The assembly of the tripartite complex is made by mixing MexA with MexB and OprM in Nanodisc mimicking the two lipid bilayers. The structure of this tripartite complex was obtained by combining cryo electron microscopy and the so-called 'isolated particles' approach. The three-dimensional structure of the complex, calculated at a resolution of less than 4 Å, was used to build an atomic model of the tripartite complex assembled between two Nanodiscs. The tripartite complex is composed of an OprM trimer, a MexB trimer and a MexA hexamer surrounding MexB and interacting with OprM. We solve the complete structure of MexA whose N-terminal part hitherto unknown because of a high flexibility and describe for the first time the anchoring of MexA in a lipid membrane. The conformational changes are observed on OprM and MexB when they are assembled in the complex with the opening of the periplasmic end of OprM and the spatial re-orientation of a MexB loop to establish additional contact with MexA.

To integrate this tripartite structure into the antibiotic efflux cycle, it describes a state that is probably a resting state, knowing that no specific ligand was added during assembly. In addition, the complex forms an open channel at its extracellular end, providing the conduit to evacuate the drugs carried by MexB that uses the proton motive force as a source of energy. This work opens new perspective for structural studies of other conformational states of the efflux system in "energized" conditions to fulfill our understanding of the efflux cycle mechanism. Moreover, the knowledge of this first tripartite native complex structure constitutes the first step towards the development of molecules capable of blocking the assembly of the complex for therapeutic uses. Indeed, such molecules would inhibit active efflux and restore the lost efficiency of current antibiotics.

Key words:

Cryo-electron microscopy, Single particle analysis, Membrane proteins, Lipid Nanodisc

Unité de recherche

[CBMN-Chimie et Biologie des Membranes et Nano-objets, CNRS UMR 5248, 14 Allée Geoffroy Saint-Hilaire, 33600 Pessac, France]

Remerciements

Le temps passe cent fois plus vite qu'on ne croit.
Georges Brassens

Je remercie le Docteur Martin PICARD et le Docteur Daniel LEVY de m’avoir fait l’honneur d’accepter d’être rapporteurs de ce travail de thèse. Un grand merci pour l’enthousiasme dont vous m'avez fait part concernant la lecture et vos retours respectifs concernant ce manuscrit. Je souhaite également remercier chaleureusement le Docteur Emmanuelle BAYER et le Professeur Pierre-Emmanuel Gleizes d’avoir accepté d’être examinateurs.

Le travail présenté dans ce manuscrit a été réalisé à l’Institut de Chimie et de Biologie des Membranes et des Nano-objets dirigé successivement par le Docteur Eric DUFOURC, et le Docteur Sophie LECOMPTE, que je remercie pour leur accueil au sein du laboratoire.

Je remercie ma directrice de thèse, le Docteur Laetitia Daury, et notre chef d’équipe, le Docteur Olivier LAMBERT de m’avoir donné l’opportunité de travailler sur ce projet passionnant en cryo-EM.

Je souhaite remercier le Docteur Olivier LAMBERT et le Professeur Jean-Christophe TAVEAU ainsi que Sisareuth TAN, et le Docteur Marion DECOSSAS pour nos nombreuses discussions scientifiques.

Merci au Docteur Marie-Christine GERBOD-GIANNONE pour ses conseils de pédagogie et son écoute.

Merci aux Docteurs Guy SCHOEHN et Isabelle BROUTIN pour leur expertise lors de nos collaborations. Nos échanges m’ont beaucoup apporté.

Merci à Patricia DULOR, Karine LANUSSE et Audrey CHANCEL pour leur fabuleux soutien à travers toutes les démarches administratives imaginables.

Merci aux membres de l’équipe Lang pour leur soutien et leur bienveillance.

Merci à mes collègues de bureau, Laurence, Dimitri, Narek, Christine, Valentine et Lisa pour leur bonne humeur, les gâteaux et cafés partagés et tous les bons moments passés en leur compagnie.

Merci aux autres membres du laboratoire pour les bons moments lors de nos pique-niques, fêtes de Noël et vendredi-midis pizza.

Merci à mes amies, Gabrielle et Audrey de m’avoir soutenue moralement ces trois dernières années et d’avoir eu le courage de m’aider pour la relecture de mon manuscrit.

Merci à ma famille d’être là pour moi.

Merci à mes parents de m’avoir préparée aux obstacles de la vie.

Merci Oma d’avoir toujours cru en moi et d’avoir été là.

Merci à mon prince charmant de partager ma vie et de m’avoir portée.

Merci à ceux qui arborent un sourire.

Acknowledgments

Time passes a hundred times faster than you think.
Georges Brassens

I would like to thank Dr. Martin PICARD and Dr. Daniel LEVY for doing me the honor of reviewing this thesis work. Many thanks for showing enthusiasm for reading this manuscript and for your respective feedback. I would also like to warmly thank Dr. Emmanuelle BAYER and Professor Pierre-Emmanuel Gleizes for agreeing to be examiners.

The work presented in this manuscript was carried out at the Institute of Chemistry and Biology of Membranes and Nano-objects directed successively by Dr. Eric DUFOURC, and Dr. Sophie LECOMPTE, whom I thank for their hospitality in the laboratory.

I thank my PhD supervisor, Dr. Laetitia Daury, and our team leader, Dr. Olivier LAMBERT for giving me the opportunity to work on this exciting project in cryo-EM.

I would like to thank Dr. Olivier LAMBERT and Professor Jean-Christophe TAVEAU as well as Sisareuth TAN, Dr. Marion DECOSSAS and Armel BEZAULT for our numerous scientific discussions.

Thank you to Dr. Marie-Christine GERBOD-GIANNONE for her advice on teaching and listening.

Thanks to Doctors Guy SCHOEHN and Isabelle BROUTIN for their expertise during collaborations. Our exchanges have brought me a lot.

Thanks to Patricia DULOR, Karine LANUSSE and Audrey CHANCEL for their fabulous support through all imaginable administrative procedures.

Thanks to the Lang team members for their support and kindness.

Thanks to my office colleagues, Laurence, Dimitri, Narek, Christine, Valentine and Lisa for their good mood, shared cakes and cafes and all the good moments spent with them.

Thanks to the other members of the laboratory for the good moments during our picnics, Christmas parties and Friday pizza lunch.

Thank you my friends, Gabrielle and Audrey for having supported me morally these last three years and for their courage to help reviewing my manuscript.

Thank you my family for being there for me.

Thank you my parents for preparing me for the obstacles of life.

Thank you Oma for always believing in me and for being there.

Thank you my prince charming, for sharing my life and for having encouraged and supported me.

Thanks to those who smile.

List of abbreviations

A

Å :	Angstrom
ABC :	ATP-binding cassette
ABE :	Access-Binding-Extrusion
AbgT :	Antimetabolite transporters
AcrA :	Acridine resistance protein A
ApoA-1 :	Apolipoprotein A-1

B

βOG :	n-Octyl-β-D-glucoside

C

C3 :	Axial symmetry 120° rotation
CCD :	Charge Coupled Device
Cryo-EM :	Cryo-Electron Microscopy
CTF :	Contrast Transfer Function

D

DARPin :	Designed Ankyrin Repeat protein
DDD :	Direct electron Detector Device
DQE :	Detector Quantum Efficiency
DMPC :	1,2-dimyristoyl-sn-glycero-3-phosphocholine
DMT :	Drug/Metabolite Transporter
DOPC :	1,2-dioleoyl-*sn*-glycero-3-phosphocholine
DPPC:	1,2-dipalmitoyl*sn*-glycero-3-phosphocholine
DOGS-NTA(Ni) :	1,2-dioleoyl-*sn*-glycero-3-[(N-(5-amino-1-carboxypentyl)iminodiacetic acid)succinyl] nickel salt

E

EC : Electron Counting

ESRF : European Synchrotron Radiation Facility

F

FSC: Fourier Shell Correlation

G

Gctf : Real time CTF estimation and correction

GO : Graphene Oxide

H

HAE1 : Multidrug hydrophobic/Amphiphilic Efflux 1

His-tag : Histidine-tag

HTH : Helix-Turn-Helix

HME : Heavy Metal Efflux

I

IM : Inner-membrane

IPTG : Isopropyl β-D-1 thiogalactopyranoside

L

L state : Loose state

LB : Lysogeny *Broth*

M

MATE : Multidrug And Toxic compound Extrusion

Mex : Multi-drug EffluX pump

MDR : Multi-Drug Resistance

MFP : Membrane Fusion Protein

MFS : Major Facilitator Superfamily

MIC :	Minimum Inhibitory Concentration
MOP:	Multidrug/Oligosaccharidyl-lipid/Polysaccharide
MSP :	Membrane Scaffold Protein

N

ND :	Nanodisc

O

O state :	Open state
OD :	Optical Density
OM :	Outer-membrane
OMF :	Outer-Membrane Facilitator protein

P

PaβN :	Phenyl-arginine-beta-naphthylamide
PACE :	Proteobacterial Antimicrobial Compound Efflux transporters
P. aeruginosa :	*Pseudomonas aeruginosa*
PDB :	Protein Data Bank
PE-NBD :	L-α-Phosphatidylethanolamine-N-(7-nitro-2-1,3-benzoxadiazol-4-yl)
PE-RB :	L-α-Phosphatidylethanolamine-N-(lissamine rhodamine B sulfonyl)
pET28a :	Plasmid Expression Transfection 28a vector
PMBN :	PolyMyxin B Nonapeptide
POPC :	1-palmitoyl-2-oleoyl-sn-glycero-3-phosphocholine

R

RELION:	REgularised LIkelihood OptimisatioN
RND :	Resistance Nodulation cell Devision
rpm :	rotation per minute

S

SEC :	Size Exclusion Chromatography
SDS-PAGE :	Sodium Dodecyl Sulfate PolyacrylAmide Gel Electrophoresis
SMR :	Small Multidrug Resistance

T

T state :	Tight state
TEV :	Tobacco Etch Virus
TM :	Transmembrane Membrane
PMSF :	PhenylMethylSulfonyl Fluoride
3D :	Three-dimension
2D :	Two-dimension

List of Figures

Table of contents

Annexes

General considerations

The project of my PhD thesis was designed to get a better understanding of the molecular mechanisms of multidrug efflux complexes involved in antibiotic resistance. My supervisor, Laetitia Daury, had recently developed a method to reconstitute *in vitro* tripartite membrane complexes from *Escherichia coli* and *Pseudomonas aeruginosa* belonging to RND efflux system responsible for drug export out of the bacteria. The originality of the complex reconstitution relied on the use of lipid Nanodisc capable of stabilizing the three membrane proteins between two Nanodiscs. The next challenge was to solve the structure of this complex at a high resolution to describe in detail the protein-protein interactions and also to get some clues on the assembly process.

The recent advanced single particle cryo-electron microscopy was well-suited to determine the 3D structure of MexA-MexB-OprM at a quasi-atomic resolution. Before considering cryo-EM experiments, the main bottleneck was related to the complex stability at high concentration. To overcome this drawback, I have revisited the protocol of the formation tripartite complex for preparing sample amenable for cryo-EM analysis, and optimized grid preparation, data collection using three high resolution electron microscopes. The results are presented in the following chapters.

Chapter 1 covers the state of the art about the RND efflux systems including the well-studied MexA-MexB-OprM from *Pseudomonas aeruginosa*, and AcrA-AcrB-TolC from *Escherichia coli* thus the reader will get introduced to the biological sample which will be further studied.

In chapter 2, the use of Nanodiscs with exogenous lipids stabilizing separately purified protein partners for *in vitro* tripartite complex reconstruction will be presented. In addition, an original method for stabilizing membrane proteins is presented and summarized in an article submitted for publication: “Minimal Nanodisc without exogenous lipids for stabilizing membrane proteins in detergent-free buffer”.

In chapter 3, two methods for preparing cryo-EM grids are presented. First, a new grid preparation method is based on the formation of functionalized lipid bilayers. The second method uses graphene oxide support adapted for low concentrated samples.

Chapter 4 will cover the single particle cryo-EM analysis and highlight the critical criteria for recording high quality images needed for 3D reconstruction at near-atomic resolution.

Finally, in chapter 5 the structural insights of the 3D reconstruction of the tripartite MexA-MexB-OprM from *Pseudomonas aeruginosa* will be discussed and compared to its homologue AcrA-AcrB-TolC from *Escherichia coli*. It allows establishing a hypothetic assembly mechanism of the tripartite efflux system.

Chapter 1

1. Introduction

Nosocomial infections are considered as hospital-acquired or hospital-associated infections. The term “nosocomial” point out diseases which are usually acquired by immuno-depressed patient under medical care. The prolonged hospitalisation of these patients is considered to be a major risk factor of infections which could lead to serious health issues or even death (Brusaferro *et al.*, 2015). However asymptomatic infections which could affect patients, medical staff or visitors are considered as nosocomial infections when pathogens are detected in blood or other body fluids. The most common nosocomial infection sites are urinary tract, surgical and soft tissue, gastrointestinal tract, meninges and respiratory tracts (Raka *et al.*, 2006). Several microbes could cause nosocomial infections such protozoans, fungi, viruses, mycobacteria and bacteria. From all these pathogens, bacteria are responsible of 90% of the nosocomial infections in healthcare. The major role are held by bacterial genus Enterococcus and bacterial species Staphylococcus aureus, Gram-positive bacteria, *Escherichia coli* and *Pseudomonas aeruginosa*, Gram-negative bacteria (Eades *et al.*, 2017). These infections were commonly treated with antibiotics since the 60’s, leading to a severe increase of healthcare cost by an increase in hospitalizations, by over medication and broad-spectrum antibiotic use. Studies showed in 2002 that 5-10% of hospitalization resulted in nosocomial infection in North America and Europe, whereas 40% in Latin America, Sub-Saharan Africa and Asia (Girard *et al.*, 2002). The broad-spectrum antibiotic use leaded progressively to antibiotic multi-drug resistance (MDR) development in bacteria and finally resulted in elevated morbidity and mortality of patients.

Pseudomonas aeruginosa is a current pathogen which contributes by 11% to nosocomial infections in medical healthcare. Contamination is caused by non-sterile environment during healthcare and affects mostly immuno-depressed patients. The urinary system and respiratory system are generally affected. The *P. aeruginosa* causes respiratory infection in declared diseases such as cystic fibrosis and pneumonia. Medical treatments against them are getting less and less efficient due to development of MDR in bacteria. The different mechanisms identified in MDR are the drug uptake restriction, the drug inactivation or modification, drug target alteration and active efflux systems (Li and Nikaido, 2009; Nikaido and Takatsuka, 2009; Piddock, 2006; Poole, 2007; Davin-Regli *et al.*, 2008; Pagès *et al.*, 2008) (Figure 1).

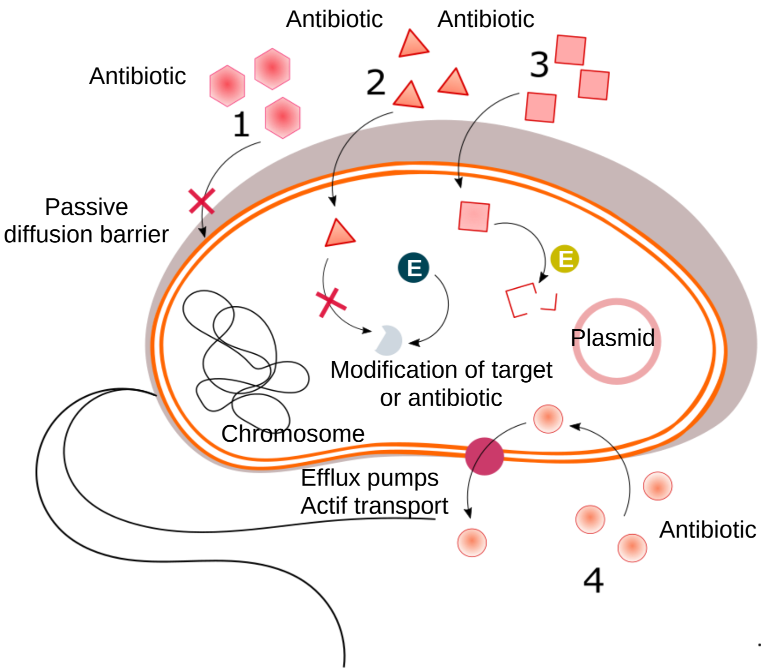

Figure 1- Antibiotic resistance mechanisms of Gram-negative bacteria

The schematic representation of Gram-negative bacteria presents antibiotic resistance mechanisms: (1) Blockage of passive diffusion; (2) Enzymatic target modification; (3) Enzymatic antibiotic degradation; (4) Efflux. Adapted from Levy and Marshall, 2004.

The increasing resistance makes ineffective the drug treatment by cephalosporins, trimethoprim, macrolides, chloramphenicol, tetracyclines and fluoroquinolones (Ma *et al.*, 1993). The MDR in bacteria emerges as a severe worldwide healthcare issue and a better understanding of antibiotic resistance mechanisms is required for developing an adequate medical treatment.

2. State of the art

2.1. Secretion systems in Gram-negative bacteria

Bacteria possess several secretion systems contributing to their high adaptability to their environment. In Gram-negative bacteria nine secretion systems are known. The first six secretion systems (type I-VI) are secreting a multitude of substrates, which are small molecules, proteins or even DNA. The seventh mechanism is a mycobacterial secretion system (Lai *et al.*, 2018; Lopez and Feldman, 2018). All of them are involved in the regulation of biological processes of bacteria such as cell-adhesion, adaptation, pathogenicity as well as survival. In Gram-negative bacteria, the secretion systems are sub-divided into two categories. The first category of secretion systems are single-membrane spanning secretion systems, with the secretion systems spanning only the outer membrane (OM) or the inner membrane (IM) (Palmer and Berks, 2012). The OM single-membrane spanning secretion system comprises T5SS secretion system, chaperone–usher pathway and pili type I or P and curli which are self-assembled cell surface appendages. The pili are long appendages which are present on the surface of Gram-negative bacteria. The pili allow the bacterial attachment, motility and inter-bacterial communication. The curli are extracellular amyloidlike protein fibres which provide the capability of adhesion and biofilm formation as well as surface colonization.

The second category of secretion systems are double-membrane-spanning secretion systems (Figure 2), which are spanning through the bacterial envelop from the IM to the OM. Those systems are the type I secretion system (T1SS), T2SS, T3SS, T4SS and T6SS (Costa *et al.*, 2015) and the multidrug transporters which are classified into seven super-families comprising the resistance nodulation cell division (RND) super-family.

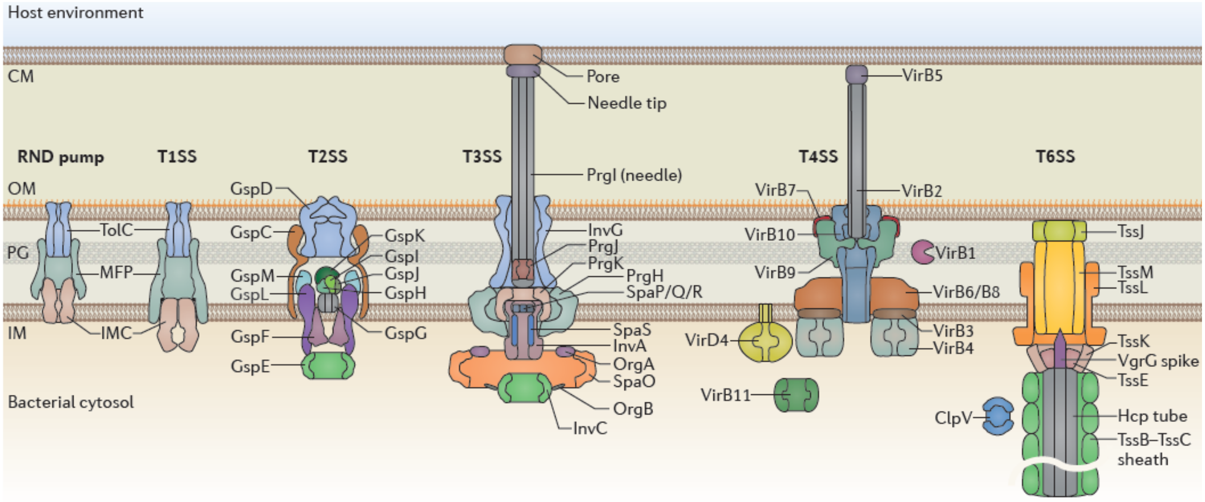

Figure 2- Double membrane spanning secretion systems

Schematic representation of RND complex, T1SS, T2SS, T3SS, T4SS and T6SS double membrane spanning secretion systems. Adapted from (Costa *et al.*, 2015).

The substrate secretion depends on the type of secretion system used by the bacteria. The substrates can have three destinations. First, the substrate could remain associated to the OM of bacteria. Second, the substrate could be extruded into extracellular space. Third, the substrate could be injected into a target cell of prokaryotic or eukaryotic origin.

The substrates are secreted across the bacterial envelope by secretion systems following a one-step or a two-step secretion mechanism (Delmar *et al.*, 2014). Most of the double-membrane-spanning secretion systems (T1SS, T3SS, T4SS and T6SS) are using a one-step secretion mechanism. It consists in transporting the substrate directly from the bacterial cytoplasm into the extracellular space or into a target cell. The two-step secretion mechanism is adopted by the OM-spanning secretion systems and the double-membrane-spanning secretion system T2SS. It is based on translocation of the substrate by the IM-spanning transporter from the cytoplasm to the periplasm. The translocation of the substrates is performed by SecYEG translocon or the Tat system (Palmer and Berks, 2012) into the periplasmic space where the substrate is extruded by the OM-spanning secretion system into the extracellular space. The substrates that are unfolded or partially folded are in majority extruded by OM-spanning and double-membrane-spanning secretion systems. There is an exception for T2SS, T6SS and the chaperone–usher pathway, which are able to export folded or partially folded substrates. The double-membrane-spanning secretion systems are not constitutively active. The secretion is probably stirred by host recognition through adhesion-receptor interaction.

The T1SSs export a broad range of substrates from small molecules to proteins. The secretion could be accompanied by nutrient uptake and bacterial virulence (Kanonenberg *et al.*, 2013). To the contrary, the RND pumps expel small exogenous and endogenous molecules, which are mainly antibacterial compounds. The extrusion of these compounds contributes to antibiotic resistance (Piddock, 2006).

2.2. Multidrug efflux transporters

The efflux systems are characterized by their transporter comprising seven superfamilies: (i) ATP-binding cassette (ABC) (Higgins, 1992); (ii) The major facilitator superfamily (MFS) (Pao *et al.*, 1998); (iii) The drug/metabolite transporter (DMT) containing the small multidrug resistance (SMR) family (Jack *et al.*, 2001); (iv) The multidrug/oligosaccharidyl-lipid/polysaccharide (MOP) exporter with the multidrug and toxic compound extrusion (MATE) family (Hvorup *et al.*, 2003); (v) The resistance-nodulation-cell division (RND) (Tseng *et al.*, 1999) (vi) The antimetabolite transporters (AbgT family) (Delmar and Yu, 2016); (vii) The proteobacterial antimicrobial compound efflux transporters (PACE family) (Hassan *et al.*, 2015).

2.3. The resistance-nodulation and cell division Superfamily

The RND superfamily is typically described as tripartite double-membrane-spanning efflux system. The efflux pumps of the RND superfamily play an important role in multidrug resistance. The most known RND transporters are AcrB of *Escherichia coli* and MexB of *Pseudomonas aeruginosa*. Both have an intrinsic elevated expression level which contributes to the multidrug resistance. These RND efflux pumps form a tripartite complex, characterized by the association of RND transporter, an OM channel TolC of *E. coli* and OprM of *P. aeruginosa* and periplasmic adaptor protein AcrA of *E. coli* and MexA of *P. aeruginosa*. Each component of the RND efflux pumps is essential in the tripartite efflux system formation and the drug efflux, even the absence of only one component renders the tripartite pump completely non-functional (Ma *et al.*, 1993; Ma *et al.*, 1995).

My PhD thesis focused on the structural study of MexA-MexB-OprM system. The next paragraphs will describe RND efflux systems using the knowledge of two well-studied systems, MexA-MexB-OprM and AcrA-AcrB-TolC.

2.3.1. The role of outer-membrane barrier in antibiotic resistance

The preservation of an intact OM barrier allows maintaining an efficient multidrug efflux which seems to play a major role in antibiotic resistance at a clinically relevant level. The first reports on multidrug efflux pumps in Pseudomonadaceae were based on clinical isolates from *P. aeruginosa* and in the 1990s the efflux-based resistance concerned a broad range of antibiotics including β-lactams. And only recently, these efflux-based resistance was recognized to contribute actively in multidrug resistance of Enterobacteriaceae (Pagès *et al.*, 2009).

The efflux pumps work in synergy with the outer membrane barrier (Davin-Regli *et al.*, 2008; Li and Nikaido, 2009). The efflux pump activity of *P. aeruginosa* is much more effective because of the low permeability of the outer membrane (Nikaido and Pagès, 2012). Indeed, the OprF channel is the major outer membrane protein of *P. aeruginosa* with a possible role as a porin (Rawling *et al.*, 1998). Its permeability is about two orders of magnitude lower than that of *E. coli* OmpF (Sugawara *et al.*, 2006; Yoshimura *et al.*, 1983). The synergy of both mechanisms is more effective at higher intrinsic resistance levels in *P. aeruginosa* for most classes of antibiotics, in comparison with *E. coli*.

3. Structural insights of RND efflux compounds

3.1. The transporter MexB and its homologue AcrB

The RND transporters are characterised by their substrate specificity and are sub-divided into five groups (Nikaido, 2018). The two first groups which were named heavy metal efflux (HME) and multidrug hydrophobic/amphiphilic efflux 1 (HAE1) are well-known (Nikaido and Pagès, 2012).

Here, we will mainly focus on AcrB from *E. coli* and MexB from *P. aeruginosa* which are both multidrug HAE1 -RND transporter and homologues. They present sequence similarity of 83.2% among respectively 1049 and 1046 amino acid residues for AcrB and MexB. Both transporters use proton motive forces for drug extrusion.

3.1.1. Structural insights of RND transporter

The first structure of AcrB solved by X-ray crystallography at a resolution of 3.5 Å was obtained by Murakami *et al.*, (2002) and revealed a homotrimer with three symmetric subunits. Later on, the structure of MexB was solved by X-ray crystallography at a resolution of 3 Å (Sennhauser *et al.*, 2009) and an asymmetric trimer. Each protomer is composed of three domains which are the transmembrane domain (TM) followed by the pore domain and the Outer Membrane Fusion protein (OMF) docking domain present in the periplasmic space (Figure 3).

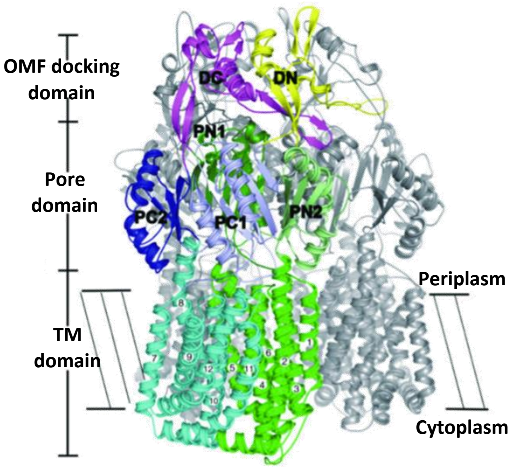

Figure 3- Crystal structure of MexB

The ribbon representation of the MexB crystal structure shows three main domains (OMF docking domain, pore domain, TM domain) and the respective subdomains of the OMF docking domain and the pore domain (DC and DN; PN1 and PC2, PN2 and PC1). The IM is represented by the dashed zone. Adapted from Sennhauser *et al.*, 2009.

The transmembrane domain is composed of 36 α-helices and is about 50 Å thick. Each protomer present an integral segment of 12 trans-membrane helices TM1-TM12 (Figure 4). Together the transmembrane segments of the three protomers delimitate a central cavity which is accessible from the cytoplasmic space. The N- and C-terminal domains are cytoplasmic. The TM domain of each protomer consists of two 6-helix parallel repeats (TM1-TM6 and TM7-TM12) which are linked by a cytoplasmic extra-membrane α-helix between TM6 and TM7 (Figure 4). The TM helices 4 and 10 contribute by their charged amino acid residues to proton translocation. The involved residues of MexB and AcrB are the Asp407, Asp408 in TM4 and Lys 939 and Lys940 in TM10. The latter performs salt-bridging with the two charged residues of TM4. The 12 trans-membrane helices of each protomer are loosely packed which suggests that interstices could be filled with phospholipids and contribute to structural flexibility.

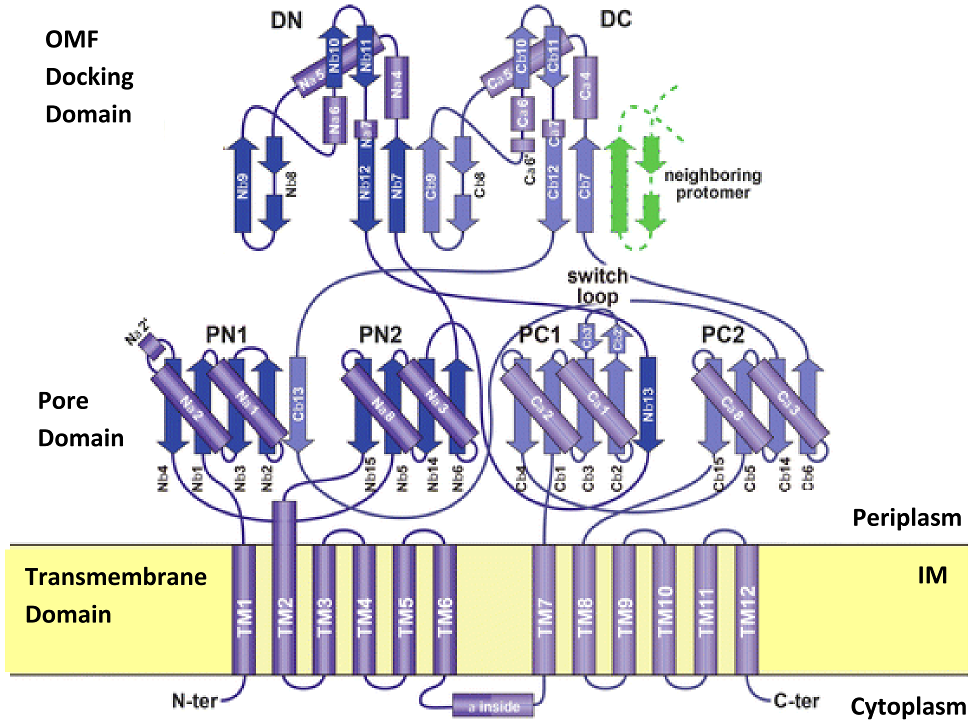

Figure 4- Topologic representation of a single AcrB protomer

The topologic representation of AcrB presents the TM domain composed of two segments the TM1-TM6 and TM7-TM12. The periplasmic domain of the AcrB composed of pore and OMF docking domain are represented by long loops of 70 Å which respectively emerge from the TM1-TM2 and TM7-TM8 helices (Murakami *et al.*, 2002, Yamaguchi *et al.*, 2015). Adapted from Yamaguchi *et al.*, 2015.

The pore domain has a large funnel-like shape and has an internal diameter about 30-40 Å. This domain is subdivided into four tight domains: PN1, PN2, PC1 and PC2 (Figure 4). The pore subdomains between TM1-TM2 and TM7-TM8 helices are respectively PN1, PN2 and PC1 and PC2. Each subdomain has a characteristic structural motif, a β-strand-α-helix-β-stand repeat. The subdomains PN1 and PC1 present both five β-strands. PN2 and PC2 present both an interruption in between their structural motif by the OMF docking domain with respectively the DN and DC subdomains. The subdomains of the pore domain are presenting the α-helices toward the periplasmic space and the β-strands are tightly packed together toward the center of the transporter protein in order to form the funnel like shape (Figure 5).

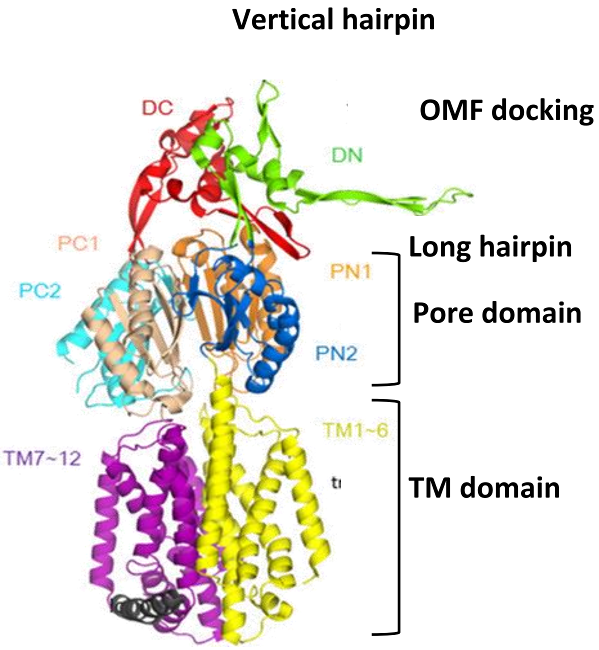

Figure 5- Ribbon diagram of the different subdomains of one AcrB protomer

The representation of AcrB protomer highlights the subdomains from the three domains. The TM domain presents 12 TM helices, the pore domain presents the four subdomains PN1, PN2, PC1, PC1 and the docking domain presents the DC subdomain and the DN subdomain with the long hairpin. Adapted from Yamaguchi *et al.*, 2015.

The OMF docking domain presents two subdomains, the DN and DC domains which are interconnected by a loop (Figure 4). The DN subdomain has a long hairpin about 35 Å (Figure 5) which allows interaction of two protomers by structural interpenetration. This type of interaction provides a strong interaction between two protomers and stabilizes the docking domain of the RND transporter.

3.1.2. Mechanistic insights of RND transporter

The upstream described crystal structure of AcrB was the first and had the particularity to be a homotrimer (Murakami *et al.*, 2002). Further investigations revealed crystal structures of asymmetric trimers at higher resolution, 2.9 Å and 2.8 Å which were respectively achieved by Seeger *et al.*, (2006) and Murakami *et al.*, (2006). Each subunit has a peculiar conformation that was used to unveil a drug transport mechanism. The 2.54 Å crystal structure of AcrB stabilized with Designed Ankyrin Repeat proteins (DARPin) from Sennhauser *et al.*, (2007) confirmed previous results. The DARPin are crystallization aids which are small proteins of high specific binding affinity. They were selected by their high binding affinity studied in Surface Plasmon Resonance and their faculty to inhibit the AcrB activity *in vivo*. The crystal AcrB structure showed two DARPins stabilizing the protomers in different conformational state. The trimer showed a distinct conformational state for each protomer. The pore domain presents a large tunnel which shows different conformation depending of each protomer. The conformation changes seem to be triggered by pivotal movements of the PN1 subdomain. The distinct conformational arrangements of each protomer suggest three functional states which could explain a transport cycle.

The previous results suggest that each protomer of the RND transporter could undergo conformational changes independently. The ability of a protomer to change conformation suggests a three-state mechanism by succeeding access of the substrate in “loose” (L) state, the substrate binding in the “tight” (T) state and the substrate release in “open” (O) state (Figure 6). The conformational changes are correlated to energy supply for functioning. In the case of the RND transporter a proton gradient drives rearrangements of the protomers for the substrate extrusion (Nikaido and Pagès, 2012). The mechanisms from substrate recognition are mediated by the pore domain (Seeger *et al.*, 2008; Takatsuka and Nikaido, 2009). The conformational changes are similar to peristaltic pump mechanism (Murakami *et al.*, 2006; Seeger *et al.*, 2006).

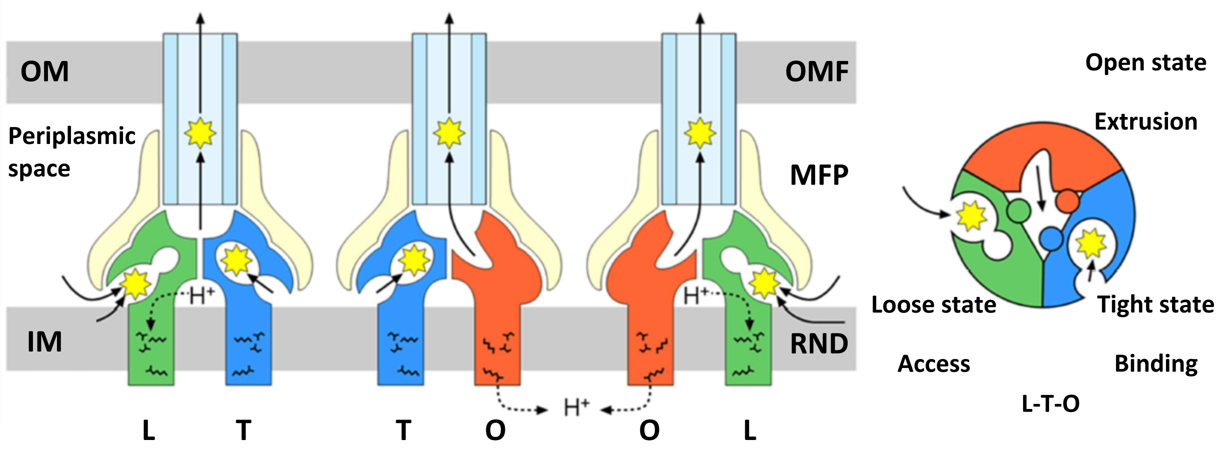

Figure 6- Functional rotating mechanism of RND transporter

The schematic representation of the sliced RND efflux pump presents the functional rotation transport mechanism with cycling in loose-tight-open state conformation. The respective conformational states of the RND transporter are represented with the access (green), binding (blue) and extrusion (red) of substrate. The substrate transition from binding to extrusion implies structural changes and proton translocation (represented with a dashed arrow at the protomer in extrusion state). Adapted from Yamaguchi *et al.*, 2015.

3.1.2.1 Conformational states of RND transporter: The loose state

The loose state is characterized by the conformation in which the substrate has the possibility to enter by three entry points. The latter were called vestibule, periplasmic cleft and tunnel (Figure 7).

The **vestibule** (Murakami *et al.*, 2006; Seeger *et al.*, 2008a), the first access point is a hydrophobic cavity which is situated 15 Å above the IM. That highly accessible cavity is located between TM8 and TM9. The hydrophobic property of the cavity suggests that only highly hydrophobic substrates coming from the outer leaflet of the IM could access the vestibule. In the loose state only the first cavity, the proximal pocket, is able to access. The substrate cannot bind to the deep binding pocket because a switch loop occludes it. The switch loop contains three amino acid residues (Phe615, Gly616, Phe617) which favour hydrophobic substrate interaction. The amino acid residues could be protonated and thus induce substrate release and a conformational change of the switch loop giving access to the deep pocket.

The **periplasmic cleft** (Seeger *et al.*, 2006) is located between PC1 and PC2 and lead to the proximal pocket. This entry point is probably taken by substrates which are less hydrophobic and soluble in the periplasm (Nakashima *et al.*, 2011; Eicher *et al.*, 2012).

The **tunnel** (Nakashima *et al.*, 2011) conformation is characterized by linkage of the large central cavity to the binding pocket through the tunnel. The binding pocket is connected to the OMF docking domain. The PN2 and PC1 of the pore domain are strongly interacting which leads to the formation of a hydrophobic pocket at their interface. This conformational state seems to have low substrate affinity.

3.1.2.2. Conformational states of RND transporter: The tight state

The tight state is characterized by conformational changes of the PN2 and PC1 subdomain from the pore domain. They induce an expansion of the hydrophobic binding pocket by repelling the PN2/PC1 from PN1/PC2 subdomains. The binding pocket is occulted at the top by the tilted α-helix of the PN1 subdomain from the adjacent protomer. The cavity stays partially open to the periplasm. The protonation of the switch loop leads to substrate release and induces changes in position of that latter occluding the access to the periplasm. This state has a high substrate affinity.

3.1.2.3. Conformational states of RND transporter: The open state

Next, the substrate is extruded actively by peristaltic movement which requires energy coming from the proton gradient (Seeger *et al.*, 2008; Pos, 2009).

Thus, the lateral entrance of the hydrophobic binding pocket open in loose state (Figure 7) and accessible in tight state will be closed in the open state by conformational changes of the PN1 and PC2. The PN2 and the PC1 move backward to the PN1 and PC1 subdomains. The substrate is pushed out by constriction of the hydrophobic cavity. The PN1 subdomain is tilting by 12-15° and opens at the central cavity in the funnel-like domain. The substrate is released into the duct of the efflux system. The substrate access from the periplasm is blocked during the open state.

After substrate release, the protomer changes from O to L state and re-exposes the binding site to the periplasm.

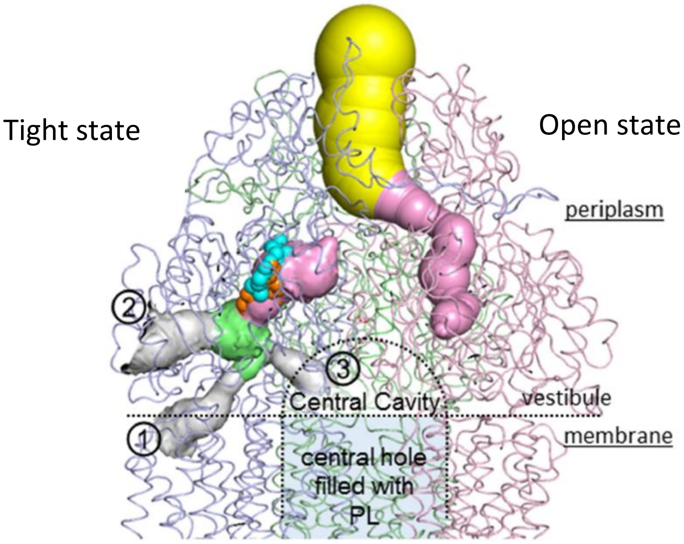

Figure 7- Substrate access and pathway in RND transporter

The solid surface representation of the intramolecular water-accessible channels in the AcrB trimer (Nakashima *et al.*, 2011). The substrate access is represented by: (1) vestibule/ inner membrane entrance, (2) periplasmic entrance, (3) tunnel/central cavity entrance. The represented protomers are in two distinct cycling states: the tight state and open state. The cavities of the two protomers are the proximal pocket (green), distal pocket (pink), entrances (gray) and funnel-like exit (yellow). Adapted from Yamaguchi *et al.*, 2015.

The initial elucidated crystal structure of AcrB showed a homotrimeric conformation in the loose state (Murakami *et al.*, 2002). It was suggested, that the trimer adopts this conformational arrangement in absence of substrate. Thus the conformational configuration was considered as resting state (Pos, 2009).

In the presence of substrate the trimer undergoes cycling mechanism. Each protomer can adopt independent distinct conformational state, as proven by the crystallization studies from Sennhauser *et al.*, (2007) with the stabilized AcrB-DARPin crystal structure which were previously described. Thus, different combinations of conformational states could be adopted by the trimer. The loose-tight-open state is likely the conformational arrangement which requires the lowest energy (Seeger *et al.*, 2006).

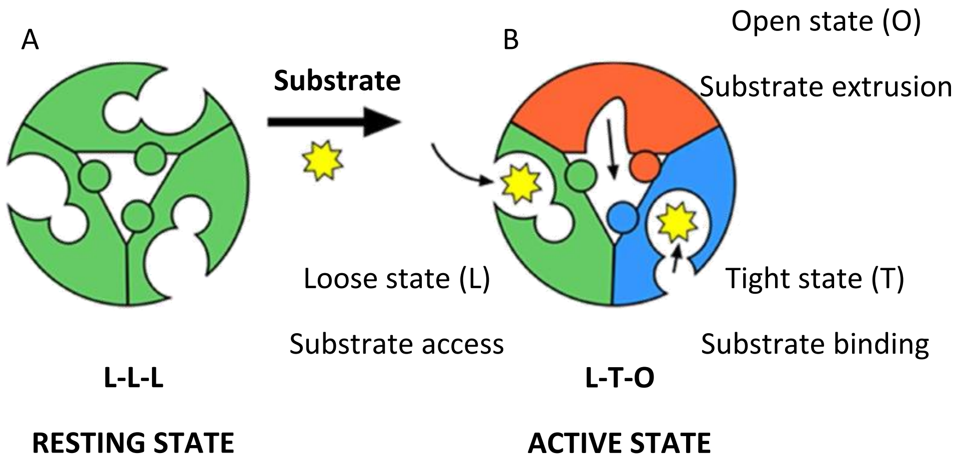

Figure 8- Resting and active states of the RND transporter

The schematic representation of the sliced RND transporter protein shows resting state in absence of substrate (A) and loose-tight-open state in presence of substrate (B). Adapted from Murakami *et al.*, 2006.

Another scenario could be considered due to interfacing of the pore subdomains of the protomers. The trimer undergoes different operating states conferring them an asymmetric nature, which suggests that the protomers are conformationally coupled (Pos, 2009). Effectively, AcrB transport kinetics (Nagano and Nikaido, 2009; Lim and Nikaido, 2010) showed that two protomers are acting in synergy, which allowed to elaborate a bi-site activation model (Pos, 2009).

The conformational cycling mechanism could induce different conformational configurations of the RND transporter. The previous described conformational states were the resting state in absence of substrate and the active state LTO with a two sequential substrate uptakes (Figure 8 and 9). The conformational cycling mechanism could lead in presence of one substrate to LLT configuration. In presence of two substrates the LLL state

RND transporter could undergo cycling and adopt LTT conformation. The protomers which are in tight state could switch in the presence of proton(s) binding to the open state. The conformational conversion from open to loose state is not known. However, the RND transporter could not adopt a conformation with two protomers in the open state. The protomers would induce a sterical clash between the PN1 subdomain of the open state protomer and the PN2 subdomain of the tight state protomer. In the presence of a third substrate the LTT conformation could undergo TTT conformation. The latter conformation is representative of high substrate concentration. One of the protomers in TTT conformation could undergo conformational changes by protonation of tight protomer to open protomer (TTO), deprotonation leads the conversion of the open state to loose state (LTT) and finally protonation of one tight state to open state leads to LTO formation.

The cycling mechanism is supported by crystallization experiments and cross-linking studies in *E. coli* membranes which reveal respectively predominant symmetric AcrB crystal structure in LLL and TTT conformational states and conformer formations which adopt a TTL and LLT conformation.

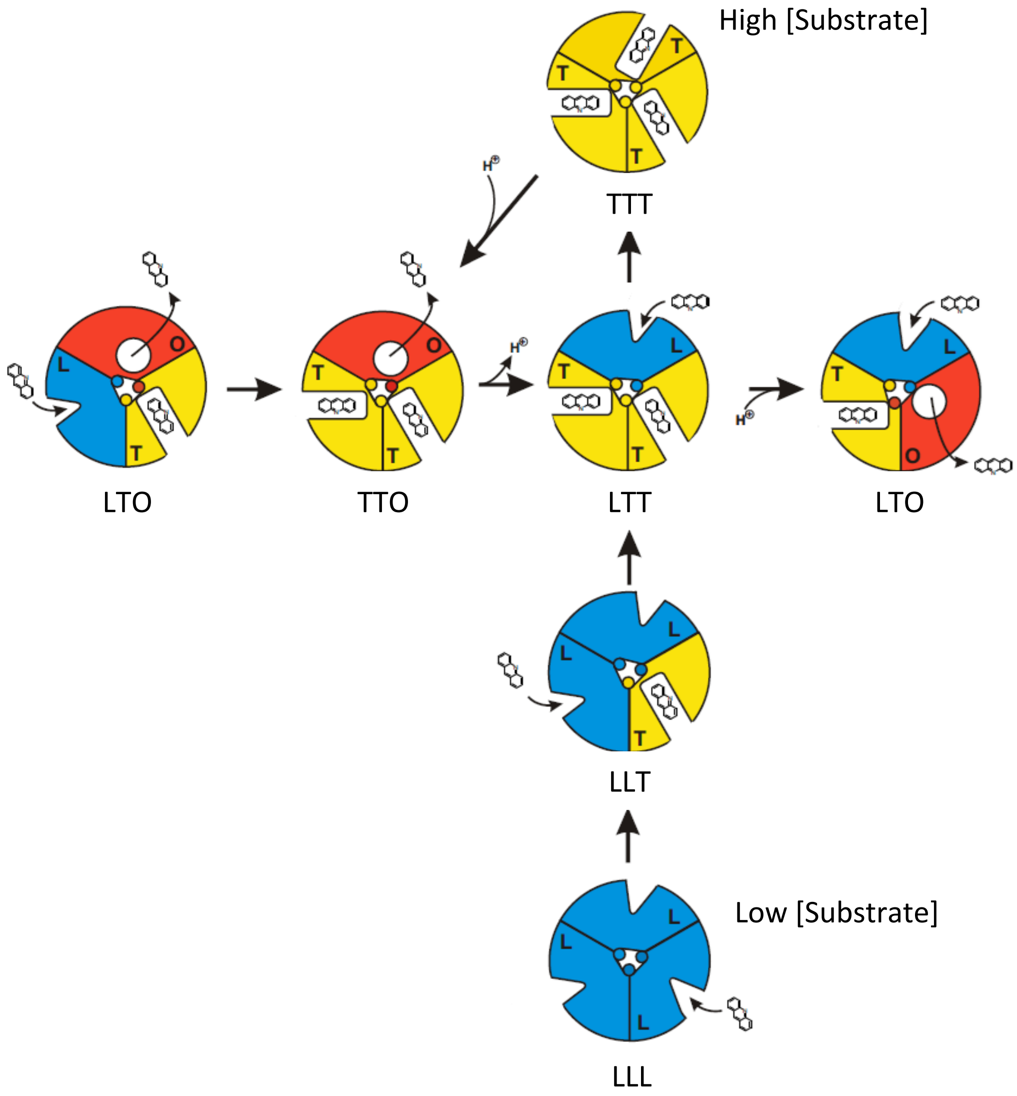

Figure 9- Conformational cycling mechanism of RND transporter

The schematic representation of the sliced RND transporter protein presents the functional rotation transport mechanism. The protomers of the conformer are represented by L state (blue), T state (yellow) and the O state (red). The different conformational arrangements were suggested in presence of substrate at low (LLL), increasing (LLT, LTT) and high (TTT) concentration. The cycling mechanism describes the substrate pathway through the access, binding and extrusion steps by the LTO, TTO and LTT conformers. Adapted from Pos, 2009.

3.1.2.4. Conformational states and their substrate specificity of the drug binding pocket

The substrates of high molecular mass are recognized and bound in the loose state by the access pocket in the porter domain. This pocket is open toward the periplasmic space (Nakashima *et al.*, 2011; Eicher *et al.*, 2012). The substrate binding to the hydrophobic pocket of the RND transporter induces proton translocation through the TM domain. The proton gradient allows inducing conformational switch from loose to tight state and the substrate translocation deeper into the binding pocket.

The substrate of low molecular-mass binds apparently directly to the deep binding pocket which corresponds to the tight state of protomer. The substrate bypasses the loose state and thus the substrate recognition and binding (Nakashima *et al.*, 2011).

Thus, the size and/or the arrangement of the substrate binding site can change in their amino acid side chains through the chemical structure of the substrate. The induced-fit mechanism (Vogt *et al.*, 2014) was suggested to be like enzymatic recognition mechanism which enables multiple substrates binding of different chemical composition. The protein structure of AcrB in tight state reveals preferential binding of doxorubicin and minocycline in the distal pocket, whereas rifampicin and erythromycin are preferentially binding the proximal pocket in the loose state.

On the other hand, the conformational changes of the drug translocation channel, during the functional-rotation cycle, could not be attributed to the induced- fit mechanism. Therefore the described mechanism is not considered as the primary mechanism of multidrug recognition.

Additional molecular dynamics simulations revealed that substrate binding in the binding pocket of AcrB could differ by the chemical structure of the substrate which leads to distinct site recognition (Takatsuka *et al.*, 2010; Vargiu and Nikaido, 2012). The proximal and distal pockets were characterized as multisite drug binding pockets. The different substrate specificity of each drug binding pocket contributes to expanding substrate specificity. Furthermore the multiple substrate entrances, the periplasmic cleft and the IM entrances are implicated into drug uptake are expanding the drug specificity.

The drug binding in the asymmetric AcrB structure seems to be difficult for most substrates and inhibitors. This could be explained by loose binding of the drug to specific sites. However, the substrate extrusion is highly efficient. The substrate extrusion becomes even more, when multidrug transporters are sufficiently expressed. Hence, the drugs are mostly extruded before crossing the IM and entering the cytoplasm.

The high drug extrusion efficiency in presence of low substrate affinity to specific binding sites could be supported by multi-site-drug-oscillation hypothesis based on molecular simulation study of AcrB (Takatsuka *et al.*, 2010). The latter showed a voluminous distal binding pocket that has several binding sites, which were subdivided in different domains: groove, cave, several mixed binding sites and single drug-binding site.

However, the supported simulation study is based on the assumption of drug oscillation in the binding pocket. This scenario gets plausible when each binding site of the binding pocket presents low drug affinity. Nevertheless, the global binding affinity of the binding pocket is high because the sum of the single binding affinities could be considered. This second drug binding model was validated by the crystal structure of the doxorubicin binding to the AcrB proximal pocket (Eicher *et al.*, 2012). The doxorubicin appeared first as dimer but was finally discriminated being an oscillating doxorubicin molecule by average density in the crystal structure. In conclusion, strongly bound substrates are fairly well resolved besides oscillating substrates which are difficult to detect in protein crystals.

3.1.2.5. The proton pathway

The substrate pathway of RND transporter is driven by proton motive force (Thanassi *et al.*, 1997; Li *et al.*, 1998; Zgurskaya and Nikaido, 1999). Each protomer of the RND transporter has a proton translocation site localized in the membrane part (Figure 10). The transmembrane proton relay network is composed by four essential charged amino acid residues: Asp407, Asp408, Lys940 and Arg971. The amino acid residues Arg971 and Thr978 were discriminated by site-directed mutagenesis to be implicated into the proton translocation site (Guan and Nakae, 2001; Su *et al.*, 2006; Takatsuka and Nikaido, 2006). In the transmembrane core ion pairs are formed between the TM4 with the amino acids Asp407, Asp408 and TM10 with the amino acid Lys940 (Murakami *et al.*, 2002; Murakami *et al.*, 2006). The Arg971 is in close proximity to the outer leaflet of the IM. The proton-relay network is energetically coupled to the conformational coupled hydrophobic binding pocket which is apart by approximately 50 Å. In an asymmetric trimer, the L and T state is characterized by ion pair formation due to interdigitating of the ε-amino group of Lys940 between the carboxyl groups of Asp407 and Asp408.

In O state, no ion pairs remain and the side chain of Lys940 is twisted by approximately 45° clock wise from the periplasm view (Murakami *et al.*, 2006). This reflects the protonation of the carboxyl group(s) of Asp407 and Asp408. This side chain twisting of

TM4 and TM10 induces twisting of the TM bundle TM1-TM6 and TM7-TM12. These induce successive conformational changes: the entrance closing, the exit opening and the extrusion stage by peristaltic motion of the deep binding pocket.

The transition from the O state to the L state is associated to deprotonation of carboxyl group(s) which restore the tripartite ion pairs. The proton relay network is based on the proton translocation observed at the crystal structure. The Lys940 residue seems to be permanently protonated. In O state all the named residues are protonated. The Asp407 and Asp408 are neutral. The ion pairs are disrupted. The side chain of Arg971 is facing the cytoplasm and thus protons can be released into the cytoplasm. The transition from the O state to the L state is mediated by deprotonation of the guanidine side chain of Arg971. Thus the side chain swings away from the cytoplasm to the transmembrane core.

In L state a proton is binding the Asp408 and will be further transferred to Arg971. The proton is binding to the aspartate which is physically closer to Arg971 and is probably forwarded by water molecules. This deprotonation leads to Lysine-Aspartate ion pairing. A second proton is binding to Asp407 and is subsequently transferred to Asp408 during the binding state.

The transition from the T state to the O state is mediated by protonation of the Asp407 from periplasm leads to unpairing of the tripartite ion pairs and swings the side chain of Lys940 away from the aspartate pair.

Several amino acid residues (Asp566, Asp924, His338, and Glu346) were identified on the periplasmic side of the transmembrane domain which seems to be implicated in proton transition (Eicher *et al.*, 2014) through the water accessible channel which are continues to the core ion pair region (Fischer and Kandt, 2011). The conformer returns to the open state by swinging away the protonated Arg971 side chain.

The protonation of the ion region from the periplasm to the cytoplasm undergoes one cycle. The changes of the ion pair conformation was discriminated from the structure of the asymmetric AcrB (Murakami *et al.*, 2006; Seeger *et al.*, 2006; Sennhauser *et al.*, 2007).

The proton translocation pathway and cycling mechanism were determined by molecular dynamics studies (Fischer and Kandt, 2011; Eicher *et al.*, 2014). The water channels connect periplasm to transmembrane core region, the ion pairs involved in T and L state which disappear in O state were observed. The orientation changes of the Arg971 were reported to act as valve in the peristaltic mechanism (Eicher *et al.*, 2014). Both aspartates could be deprotonated in one cycle during the T state and protonated during the O state (Eicher *et al.*, 2014). It remains still unclear how Arg971 mediates the two protons relayed from the ion pairs to the cytoplasm in one cycle.

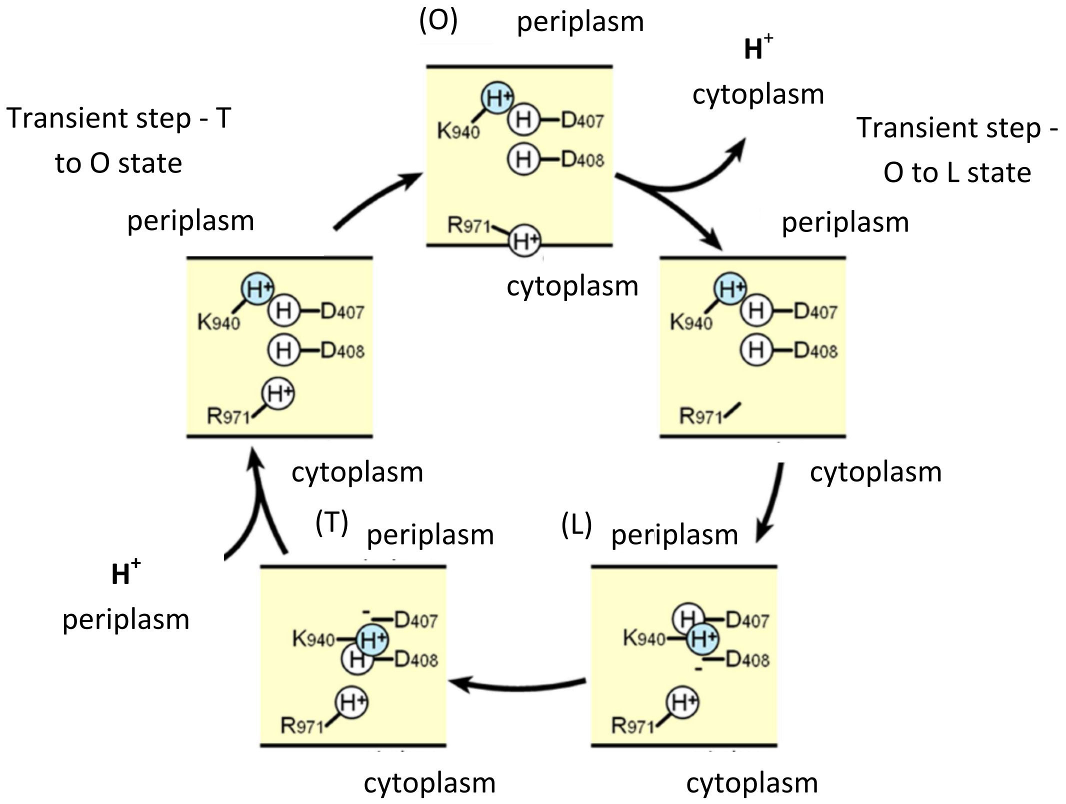

Figure 10- Proton pathway during cycling mechanism of RND transporter

The schematic representation of proton pathway in the transmembrane domain shows O state (O), transient step from O to L state, T state (T), transient step from T to O state. The permanent bound protons are labelled in blue and flexible protons are represented in white. Adapted from (Yamaguchi *et al.*, 2015).

3.2. The channel protein OprM and its homologue TolC

The OMF of the RND efflux system which were mostly studied are TolC from *E. coli* and its homologue, OprM from *P. aeruginosa*. The TolC protein (Wandersman and Delepelaire, 1990; Fralick, 1996) is a homotrimeric channel which was characterized by X-ray crystallography at 2.4 Å (Koronakis *et al.*, 2000).

3.2.1. Structural highlights of OprM and its homologue TolC

The crystal reveals 12 helices which build-up a channel having an outer membrane domain of 40 Å and the periplasmic domain of 100 Å (Figure 11). The periplasmic domain is further subdivided into 3 domains which are coiled-coil domain at its periplasmic extremity, followed by the equatorial domain and α-barrel domain toward the outer membrane. The transmembrane domain is composed of a β-barrel domain (Figure 11). One monomer of the homotrimer is composed by two β-strands repeats and a coil-coil pair. Very little differences between monomers of OprM or TolC where highlighted. The OprM structure from (Akama *et al.*, 2004a) compared to the structure obtained by Phan *et al.* (2010) reveals 13 additional residues in the C-terminus and 44 residues in the N-terminus.

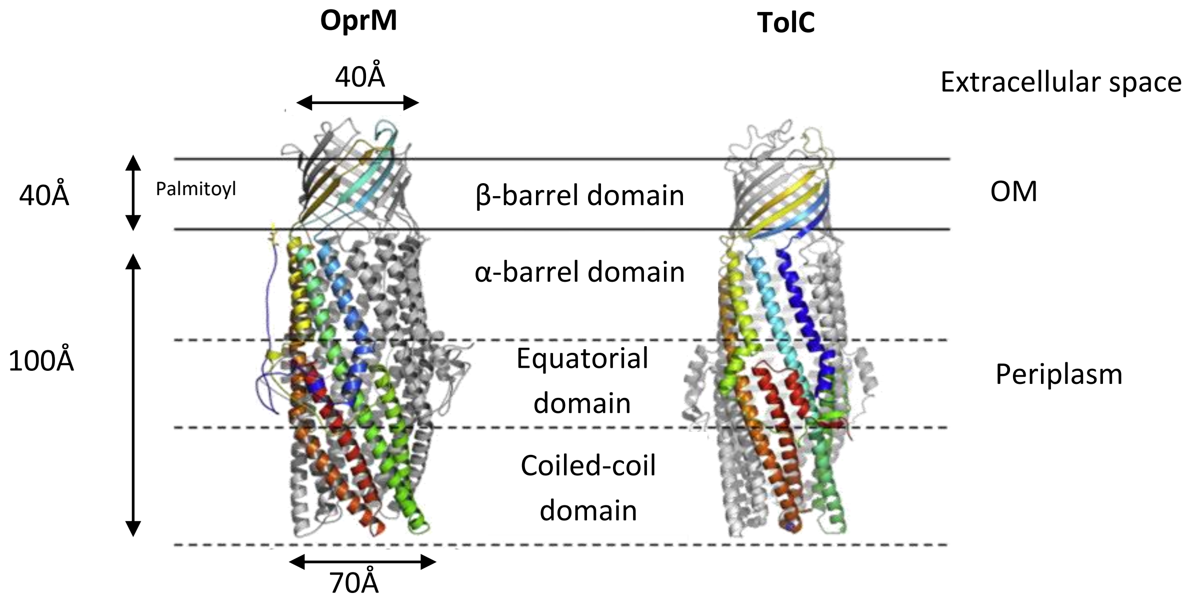

Figure 11- Crystal structures of OprM and TolC

The ribbon representations of channel proteins OprM and TolC present α-helical and β-barrel domains. The α-helical domain is subdivided in: α-barrel, equatorial, and coiled-coil domains. One monomer is highlighted in rainbow colours. Adapted from Phan *et al.*, 2010.

3.2.2. Opening mechanism of OprM and its homologue TolC

The OprM crystal structure (Akama *et al.*, 2004a; Phan *et al.*, 2010) present a porin domain closed at both ends. The aperture of the porin domain facing the extracellular medium is probably closed in ground state, thus substrates could not enter the bacterial envelope. As consequence the opening of the porin has to occur after tripartite assembling in perspective of drug extrusion. The porin opening implicates different movements described as an iris-like mechanism (Phan *et al.*, 2010).

The periplasmic entrance commonly shows a constriction formed by the ‘’inner coiled-coil’’, the H7/H8 α-helical coiled-coils, and the ‘’outer coiled-coil’’, the H3/H4 α-helical coiled-coils, from each monomer (Figure 12). The closed conformation of the periplasmic entrance was attributed to hydrogen bonding between the outer and inner coiled-coil of TolC (Andersen *et al.*, 2002; Bavro *et al.*, 2008). The interaction occurs by establishing one hydrogen bond between a highly conserved tyrosine from the inner coiled-coil and an acidic residue from the outer coiled-coil as shown for OprM (Phan *et al.*, 2010). This key interaction has to be disrupted for opening. The required energy for channel opening comes probably from the interaction with the MFP-RND partners.

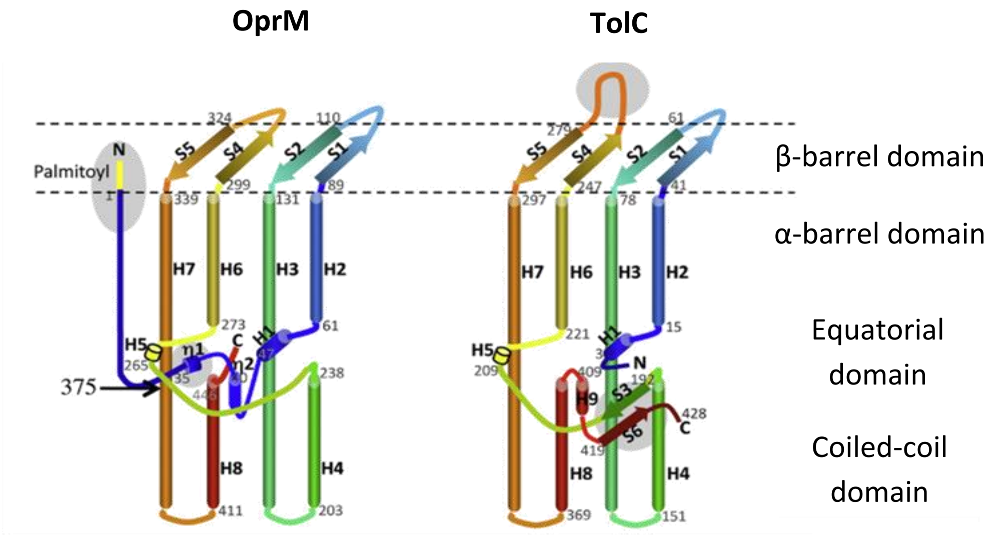

Figure 12- Topologic diagrams of OprM and TolC

The cartoon representations of the channel proteins OprM and TolC present the α-helical and β-barrel domains with the respective nomenclature. The α-helical domain is subdivided into α-barrel domain, equatorial domain and coiled-coil domain. Adapted from Phan *et al.*, 2010.

Some local differences between monomers of OprM are concerning exclusively polar side chains. One of these differences concerns several residues which are at the periplasmic entrance (Phan *et al.*, 2010). The residue R405 of OprM corresponds to the key residue S363 of TolC which is involved in the interaction of OMF and MFP (Lobedanz *et al.*, 2007). The interaction of OMF and MPF leads to conformational changes from closed to open state of the OMF. An iris-like motion of the α-helical domain leads to the enlargement of the outer coiled-coil region by 2 Å and the inner coiled-coil region by 1 Å. The aperture of the OMF is maintained by strong hydrogen bonds and salt bridge formation between two monomers. The key residues involved in hydrogen bonding are R419 and D416 of two neighbouring monomers. The β-barrel domain is opening synchronised with the periplasmic domain. The OMF gives rise of a 3-10 Å aperture at the β-barrel domain. The equatorial domain plays the role of a hinge during the OMF opening. The topology of the equatorial domains of the OMFs is quite different. The common features of TolC and OprM are two α-helices, the H1 and H5, and the large loop between H4/H5 (Yamanaka *et al.*, 2007) suggests that this loop is implicated in the recruitment of the MFP partner.

The crystal structure of OprM reveals a N-terminal end which is 44 residues longer compared to the N-terminal of TolC (Figure 13). The N-terminal of OprM goes from the equatorial domain toward the β-barrel domain, along the α-helices of the periplasmic domain and sizes 60Å (Figure 8). The last residue of the N-terminal is a cysteine. Until 2010, the crystal structure of OprM gave no evidence of lipidation in the thiol or amine function of the last cysteine (Phan *et al.*, 2010). This could be due to high flexibility of the lipidic anchor. Recently, the N-terminal lipidation was determined by fluorescent probing of the thiol and amine function of the last cysteine (Phan *et al.*, 2010; Monlezun *et al.*, 2015). This study showed that OprM is palmitylated at its N-terminal cysteine by thio-palmitoylation. The post-translational lipidation is particularly essential for the secretion and localization of some membrane proteins. OprM is addressed by the thio-palmitoylated N-terminal to the outer membrane and maintained by the peptidoglycan in the periplasmic space. In contrast, TolC has no N-terminal anchor and seems to be stabilized by the anchoring of the β-barrel in the outer membrane and the periplasmic domain by the peptidoglycan in the periplasmic space.

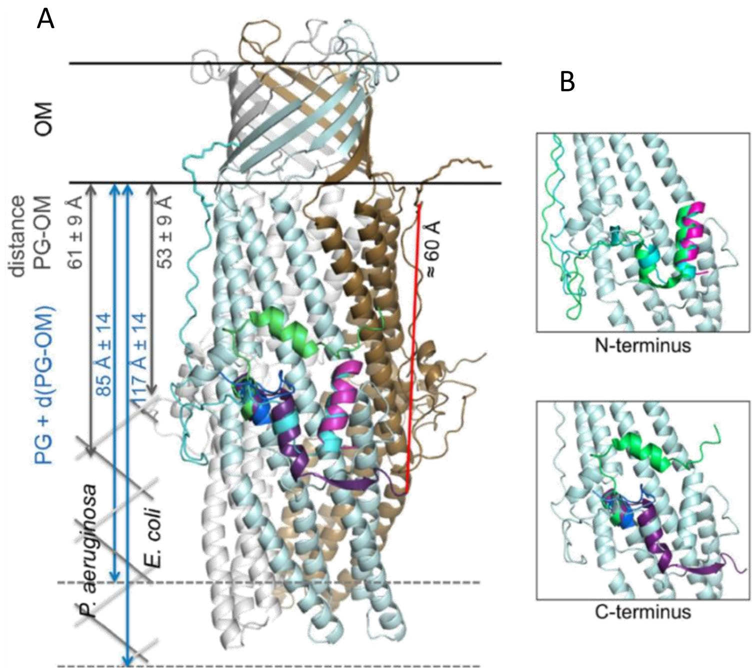

Figure 13- Comparative between crystal structures of OprM and TolC

The crystal structure of OprM (in light blue, gray, and brown) from *P. aeruginosa* is enshrined by the β-barrel domain and N-terminal end into the outer membrane. The length of the N-terminal is indicated on one monomer of the OprM trimer (red). The OMF is positioned in respect to the outer membrane and the peptidoglycan (PG) with the relative distances (Matias *et al.*, 2003) (A). Structural differences are highlighted at the N- and C-terminal ends of OprM (cyan and dark blue respectively) from *P. aeruginosa* and TolC (magenta and violet respectively) from *E. coli* (Phan *et al.*, 2010; Monlezun *et al.*, 2015) (B). Adapted from Monlezun *et al.*, 2015.

The crystal structure of the native OM channel TolC showed to be closed at the end of the periplasmic domain. However the OM channel is opening for drug export and has to remain open (Koronakis *et al.*, 2000; Murakami *et al.*, 2002). The open form of the TolC structure was experimentally determined with a mutant (Bavro *et al.*, 2008; Pei *et al.*, 2011). Those results suggest that the mutated amino acids play key role in channel opening.

3.3. The membrane fusion protein MexA and its homologue AcrA

The MFPs belong to a family of proteins which presents sequence similarities with viral fusion proteins. The name of the MFPs comes from the supposition that AcrA and MexA protein could span the inner and outer membrane (Zgurskaya and Nikaido, 2000). Finally it was experimentally proven that MFP only interacts with the inner membrane (Touzé *et al.*, 2004; Elkins and Nikaido, 2003). The MFPs of RND pumps are characterized by X-ray crystallography and the first crystallized structure was MexA from *P. aeruginosa* (Akama *et al.*, 2004b; Higgins *et al.*, 2004) followed by the AcrA from *E. coli* (Mikolosko *et al.*, 2006). Bavro *et al.* (2008) suggested that MFP seems not necessary in substrate extrusion, RND transporter AcrB and OMF TolC should be able to interact without any additional partner. Both present a comparable diameter with complementary electrostatic properties. According to these suggestions the substrate could be transported from the inner membrane, or from the cytoplasm through the OMF. The MFP does not seem to be essential in the drug pathway. The crystal structures of the connected RND and OMF have a global length of 170 Å spanning the periplasmic space. All these observations are supporting the hypothesis that the MFP is not necessary in drug extrusion.

3.3.1. Structural insights of fusion protein MexA and AcrA

The first resolved MFP is MexA from *P. aeruginosa* in 2004 by X-ray crystallography at a 3.0 Å resolution (Akama *et al.*, 2004b). MexA is composed of 360 residues and presents a linear architecture which is 90 Å long and 35 Å wide. The first MexA structures were missing a region called membrane proximal (MP) domain, which suggests that this region is highly flexible. The full length MexA was described by Symmons *et al.*, (2009) from the solved MexA structure of Akama *et al.*, (2004b), revealing 4 domains which are the MP domain, the α-hairpin domain, followed by the β-barrel domain and the lipoyl domain (Figure 14).

The α-hairpin domain is 47 Å long and supposed to interact with OprM. The connecting loop which is linking the two α-helices of the α-hairpin domain is 13 amino acids longer for AcrA than for MexA. This structural difference could have its importance in MFP and OMF interaction and thus in tripartite complex formation. The MFP's are differing in length and architecture depending on the bacterial origin which implies multi-potentiality of the MFP to interact with different IM and OM components.

The lipoyl domain is characterized by a β-sandwich composed by two interlocking motif of four β-strands. The β-barrel domain is composed of six antiparallel β-strands overhung by a single α-helix. The MP domain is a β-roll linked on one side to the proximal β-barrel domain and on the other contains the N-terminal which is anchored via fatty acid(s) into the IM (Akama *et al.*, 2004b; Symmons *et al.*, 2009). The N- and C-terminal ends are close to each other located at MP domain.

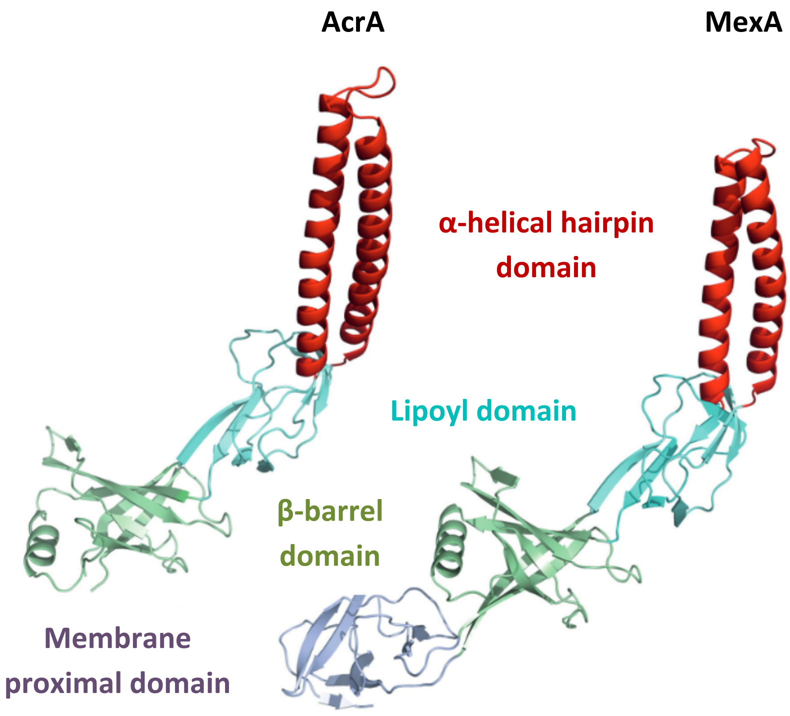

Figure 14- Crystal structures of AcrA and MexA

The ribbon representation reveals three common sub-domains: α-helical hairpin domain, lipoyl domain, β-barrel domain. The AcrA molecule is missing the membrane proximal domain compared to MexA. Each sub-domain of both structures is distinguished by a different colour. Adapted from Du and Luisi, 2015.

MexA could oligomerize and organize into an asymmetric 13-mer which interact by their helices (Akama *et al.*, 2004b; Higgins *et al.*, 2004b). The 13-mer presents an asymmetric cylindrical shape of 40 Å in diameter. The helices are organized in a coiled-coil manner and in its end the 13-mer is widening (Figure 15).

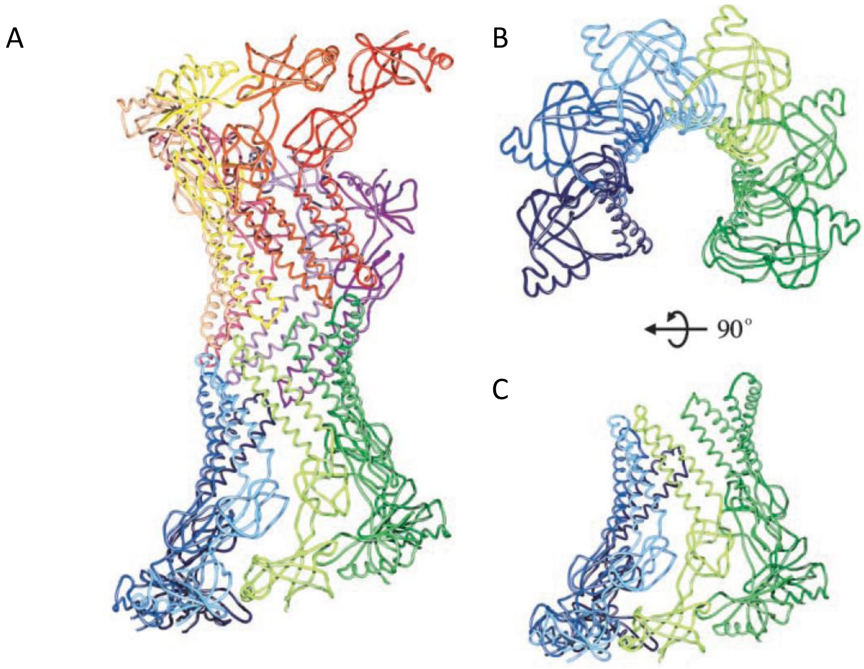

Figure 15- Oligomeric form of MexA in the crystal

The backbone representation MexA 13-mer is composed of two 6-mer which are interacting in “tip to tip” manner (A). The 6-mer is an asymmetric open structure, which is represented by a top view (B) and a side view (C). Each MexA monomer is distinguished by a different colour. Adapted from Higgins *et al.*, 2004b.

AcrA from *E. coli* (Mikolosko *et al.*, 2006) present a packed crystal of a dimer of dimers. Both homologue structures are differing in packing the AcrA is dimer and the MexA a monomer.

By considering that MexA is an inescapable component in tripartite complex building and is anchoring into the IM, a mutation deleting the fatty acyl moiety was performed. Thus MexA mutant is freely soluble and shows fully functional antibiotic efflux (Yoneyama *et al.*, 2000). These results suggest that the entire protein moiety of MexA is extended into the periplasmic space. Thus the fatty acyl moiety of the MexA N-terminal is assumed to be anchored into the IM.

3.3.2. Interaction of fusion protein MexA in RND efflux pump

The α-hairpin domain of MexA is binding by the RLS motif (R119, L123, S130) to the OM channel protein OprM (V201, V408, S138) (Symmons *et al.*, 2015). The β-barrel domain and a lipoyl domain are both interacting with the RND (Yum *et al.*, 2009). The C-terminal end, part of the membrane proximal domain, is implicated in interaction of MFP with the RND transporter. The orientation of MexA MP domain seems to be in close proximity to the RND transporter MexB and with α-helical hairpin domain toward the OM channel OprM (Akama *et al.*, 2004b).

The four domains of MexA are joined by linkers who could confer flexibility and induce molecular dynamic. That proposal was confirmed by molecular dynamic simulation which showed domain bending and relative rotation of the domain to each other (Vaccaro *et al.*, 2006). The MPF flexibility allows adapting to protein partners in order to build up the tripartite complex.

Narita *et al.*, (2003) quantified from intact cells the individual components of the MexA-MexB-OprM complex which allowed suggesting a 6:3:3 stoichiometry of the efflux system. The protein ratio suggests that five to six MexA could interact with MexB and OprM. A gel filtration experiment allowed discriminating the monomeric from the dimeric MexA and determining the major fraction which correspond to the dimeric form of MexA. These results are suggesting a 3-fold MexA dimer model. In order to map the entire MexA-MexB-OprM efflux system, the MexA dimers were fitted by the α-helical hairpin domain to the lower part of OprM (Higgins *et al.*, 2004). The β-barrel domain of MexA fits with the MexB-OprM contact region. It was suggested that MexB is interacting with the β-barrel domain of MexA (Higgins *et al.*, 2004).

3.4. *Other protein partners of RND tripartite complex*

The RND tripartite pumps are described as complexes which span the IM and the OM. However, it was reported that other RND components could be involved in the tripartite complex formation and stabilization. Thus the RND pumps could be a multi-compound complex.

In this following paragraph two stabilization proteins YajC and AcrZ from AcrA-AcrB-TolC of *E. coli* were chosen for description. Both were characterized as a single TM helix.

3.4.1. *RND stabilization protein: YajC*

The stabilization protein YajC was characterized by co-crystallization, of the single TM helix YajC associated to AcrB (Törnroth-Horsefield *et al.*, 2007). YajC is composed of 37 residues with a length of 54 Å and crosses through the membrane. The interaction of YajC and AcrB occurs with TM2, TM7, TM11 and TM12 of AcrB. The AcrB presents conformational changes in presence or absence of the stabilization protein. The co-crystalized structure present TM helix rotation from AcrB pore domain. The presence of YajC induces as well rotational movements of the transporter and does not avoid substrate uptake. In order to understand the physiological role of YajC, *in vivo* studies were performed on Δyajc strains. The substrate uptake is little reduced which proves that AcrAB-TolC remains functional. The role of the YajC remains unclear.

3.4.2. RND stabilization protein: AcrZ

The AcrZ protein which is also named YbhT was characterized through genetic screening. The protein is composed of 49 residues. The protein is binding AcrB (Hobbs *et al.*, 2012) and are localized in the OM and predominantly in the IM of *E. coli*. The purification of AcrA and AcrB are co-eluted with AcrZ. The AcrAB-TolC multidrug efflux system gets sensitive to antibiotics in ΔacrZ strains. Thus, AcrZ presents substrate affinity. The co-crystallization of AcrB-AcrZ (Figure 16), present AcrZ as folded α-helix which binds the deep binding pocket (Du *et al.*, 2014). The AcrZ is inshrined with a 45° angle in the IM along and interacting with the TM domain of AcrB. The protein could probably induce allosteric modulation which could modify the substrate recognition and binding. That protein is not conserved in all RND efflux pumps. In fact, sequence analysis of the integral *P. aeruginosa* genome showed that the MexA-MexB-OprM has no additional protein partner.

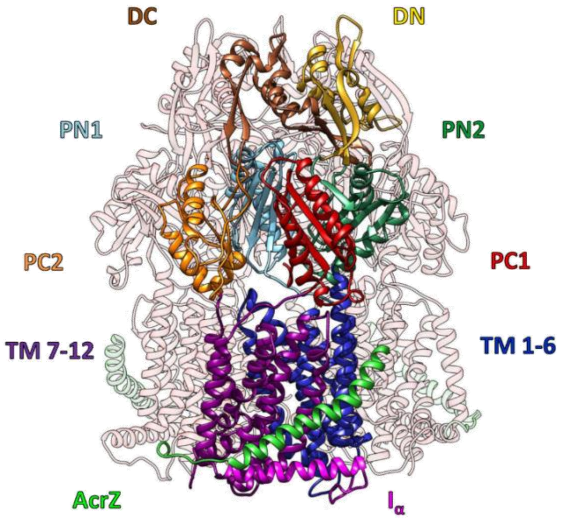

Figure 16- Co-crystal structure of AcrB-AcrZ

The ribbon representation of AcrB-AcrZ co-crystal presents a distinct colour code for the structural features and shows the AcrZ positioning in the transmembrane domain of the AcrB. One monomer of AcrB and the associated linker protein are highlighted in colour. The AcrZ (light green) is represented at the TM domain of AcrB. Adapted from Du *et al.*, 2014.

4. The RND tripartite efflux pump

4.1. The tripartite structure of RND assembly

The crystal structure and organization of RND efflux pumps were limited over the last decades to structural data of individual components of the efflux system or limited to bipartite complexes (Su *et al.*, 2011).

The scientific community is confronting two models of the RND efflux system assembly.

4.1.1 The "deep interpenetrating" or direct interacting models

The first supported model was described by Akama *et al.*, (2004b). They described a model which presents deep interpenetration between the helical hairpin of the MFP and the coiled-coil domain of OM channel. Thus, the RND transporter AcrB is presumably docking directly the OM channel TolC, because diameter and shape of AcrB fit with the open form of the OM channel TolC (Symmons *et al.*, 2009).

The "deep-interpenetration" model could present different assemblies of RND-MFP-OMF in terms of stoichiometry with 3:9:3, 3:6:3, and 3:3:3 ratios. Fernandez-Recio *et al.* (2004) supported the 3:3:3 model with a direct interaction between the RND transporter and TolC (Figure 17). These "deep-interpenetration" models are supported by direct evidence of cross-linking studies and gain of function analyses of AcrAB-TolC efflux systems (Bavro *et al.*, 2015).

In vivo cross-linking experiments between AcrB and TolC (Tamura *et al.*, 2005; Weeks *et al.*, 2010) and *in vitro* detection of direct interaction of AcrB-TolC in the absence of

AcrA through surface plasmon resonance (Tikhonova *et al.*, 2011) were supporting the “deep-interpenetration” model. Further surface plasmon resonance studies allowed detecting separately AcrA, bi-partite AcrA-AcrB and AcrA-TolC complexes formation (Tikhonova and Zgurskaya, 2004; Touzé *et al.*, 2004). Hence, it was suggested that AcrA is recruiting TolC to form a tripartite complex (Tikhonova *et al.*, 2009). The cross-linking of AcrA-AcrB (Symmons *et al.*, 2009), AcrA-TolC (Lobedanz *et al.*, 2007) and MexA-OprM (Ferrandez *et al.*, 2012) showed a 1:1 stoichiometry respectively. These results are supporting the “deep interpenetrating” tripartite model has a 3:3:3 stoichiometry with three AcrA which are interacting with the 3:3 direct docking complex AcrB-TolC (Symmons *et al.*, 2009) (Figure 17). The model sizes approximately 270 Å. The interaction between the tripartite components were highlighted, the α-hairpins of AcrA are interacting with TolC, and AcrA is interacting by their three other domains with the DN and PN2 domains of AcrB. In conclusion the “deep interpenetrating” model could be supported by individual crystal structures of the tripartite components and cross-linking experiments.

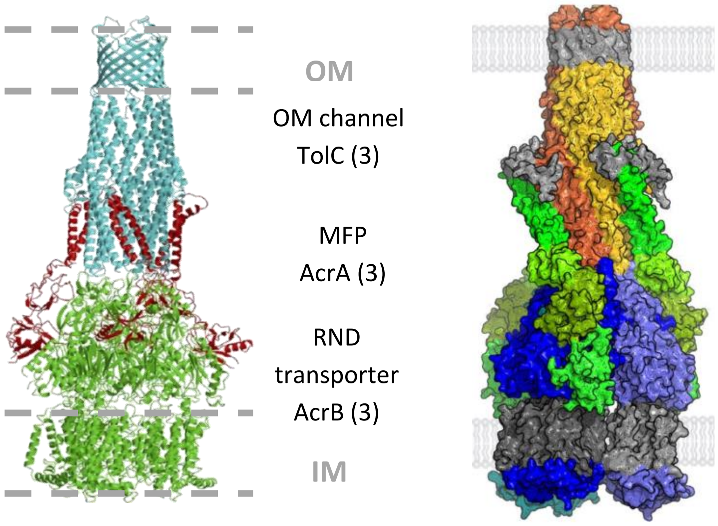

Figure 17- "Deep interpenetrating" RND model

The *in vivo* cross-linked AcrB-AcrA-TolC efflux system is described by the “deep interpenetrating” model with a stoichiometry of 3:3:3, represented respectively in green:red:blue (left) and blue:green:orange (right). Adapted from Fernandez-Recio *et al.,* 2004 (left) and Symmons *et al.*, 2009 (right).

4.1.2. The "tip-to-tip" or indirect interacting models

The second supported model is the "tip-to-tip" model (Figure 18) which was recently described from the complete structure of AcrB-AcrA-TolC RND efflux system obtained by single particle cryo-electron microscopy analysis (Du *et al.*, 2014; Kim *et al.*, 2015).

The tripartite complex from Du *et al.* (2014) was obtained from fusion proteins AcrA-AcrB and AcrA-AcrZ-His co-purified with TolC (Du *et al.*, 2014). The cryoEM structure was calculated at 16 Å resolution which allowed fitting the crystal structures of all components and provided the stoichiometry of 3:6:3 AcrB-AcrA-TolC (Figure 18). The model is described having drumstick shape with an approximate length of 320 Å. It shows no interaction between AcrB and TolC in the assembly. Both are connected by the fusion protein AcrA in the periplasm. The six AcrA's are forming in between the AcrB and TolC a tube comprising the α-helical and lipoyl domains and a portion of the β-barrel domains.

The cross-section of the AcrA-AcrB-TolC complex is revealing a cavity which corresponds to the duct of the efflux system. This latter present different widths comprised between 16 Å and 34 Å, from the periplasmic side of AcrB to the extracellular side of TolC. The OM channel TolC adopts an open conformation after assembling into a tripartite efflux system. This conformational change is probably due to binding of OM channel with the MFP-RND bipartite complex. It was suggested that the assembly formed *in vivo* requires no substrates or proton-motive force (Tikhonova and Zgurskaya, 2004) to induce the conformational changes to the open state of the OM channel TolC. The conformational change from the closed to the open state of TolC is probably driven by the hexameric organisation of AcrA.

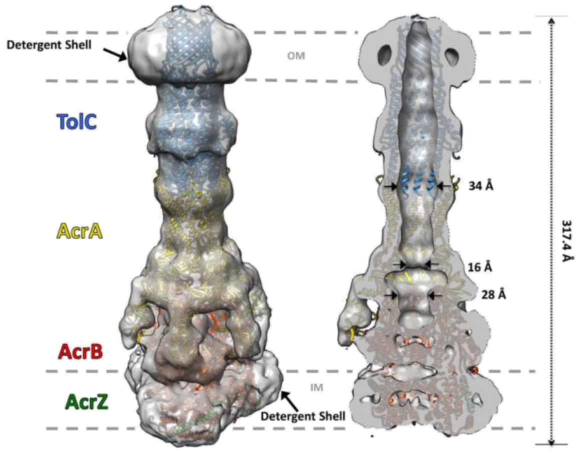

Figure 18- "Tip-to-tip" RND model

The AcrBZ-AcrA-TolC efflux system is represented a “tip-to-tip” model. The crystal structures of the three protein partners are in the cryo-EM density map. The map shows a stoichiometry of 3:6:3. The TM domains of the channel protein and the RND transporter are enshrined into detergent shells. Adapted from Du *et al.*, 2014.

The “deep interpenetrating” model may represent an intermediate step of active tripartite complex formation. This supposition could be made considering the stoichiometry of AcrA in the complex, with the recent observation of AcrB-AcrA one-to-one fusion protein (Du *et al.*, 2014). For that, later observations of *in vivo* complementarity were made by activity recovery of AcrA-AcrB deficiency. The results suggested that 1:1 stoichiometry allows to perform drug extrusion (Hayashi *et al.*, 2016). Considering that the hypothesis of an intermediate assembly, these results may be not in contradiction with the chimeric assembly of Du *et al*., (2014) presenting a 3:6:3 stoichiometry.

4.2. Assembly and disassembly of RND tripartite complex

Genetic and *in vivo* studies allowed demonstrating that the MPF seems to be absolutely necessary to assemble functional tripartite pump (Ge *et al.*, 2009). Tikhonova *et al.* (2011) showed with sequential assembly studied in SPR that on the surface oriented AcrB was not interacting with preformed AcrA-TolC complex. The AcrA-AcrB formation was inhibited when adding to early TolC which could enter in competition with AcrB for AcrA. The tripartite assembly were obtained by co-injection of AcrA-AcrB and TolC-AcrB with a complex AcrA:AcrB:TolC suggesting a 6:3:3 stoichiometry. The reconstitution in liposome of the tripartite system reveals that a functional system can be formed from native MexA, MexB, OprM proteins (Verchère *et al.*, 2014; Ntsogo Enguéné *et al.*, 2015). Thus, the tripartite assembly process appears to be a proton-independent process. It was confirmed by the native protein reconstitution of tripartite complex into Nanodisc (Daury *et al.*, 2016).

The disassembly of the system has been observed after effective drug efflux in the presence of proton (Ntsogo Enguéné *et al.*, 2015). The disassembly process seems correlated with the proton or/and drug transport that was previously indirectly suggested by Bavro *et al.*, (2008). The precise mechanism still remains to be elucidated.

4.3. Dynamic considerations regarding the assembly of RND tripartite complex

Drug uptake of RND tripartite complex occurs from the outer layer of the inner membrane and/or from the periplasm (Sennhauser *et al.*, 2007; Husain *et al.*, 2011; Nakashima *et al.*, 2011). The high efficiency of drug extrusion and the relatively low intrinsic expression level of RND transporters suggest rapid sweeping of the RND transporter in the inner membrane through lateral diffusion (Bolla *et al.*, 2011; Yamaguchi *et al.*, 2015). However, the peptidoglycan mesh which stabilizes the trans-periplasmic tripartite complex prevents from lateral diffusion.

Two succeeding modes, the horizontally-diffusion drug-sweep and the fix drug-extrusion are probably necessary for substrate sweeping and the efficient substrate extrusion. This suggestion was made because TolC is a multifunctional OM channel which interacts with various RND transporters. The tripartite complex formation would be needed for optimized efflux (Zgurskaya, 2009).

The sweeping mode is described to work with the RND transporter alone or with the MFP. This latter may move laterally via Brownian motion in the lipid bilayer of the IM. Each protomer of the RND transporter adopts a symmetric O state conformation and gets accessible for substrates even in absence of substrate.

The MFP is binding to the RND transporter and their motion is bending downwards the α-helical moiety. The conformational arrangement of AcrA linked to RND transporter was previously described (Du *et al.*, 2014). However the AcrA is bent downward and could be easily adapted due its high flexibility between the subdomains of the RND transporter (Vaccaro *et al.*, 2006). In presence of substrate each protomer of RND transporter could bind a substrate and thus undergoes cycling mechanism.

The presence of MFP induces the OM channel recruitment in the perspective to build up a tripartite efflux pump. After drug extrusion, it was suggested that, the tripartite complexe is immediately dissociating. Nevertheless, the tripartite complex may not dissociate and is continuously pumping in presence of high substrate concentration.

The substrate sweeping and extrusion mode could explain the high efficiency of drug efflux and thus role of the RND efflux pumps in antibiotic resistance.

Results

Chapter 2 - Stabilization of the components of the MexA-MexB-OprM tripartite complex in detergent-free buffer: Input of Nanodisc technology

The following chapter will briefly present the Nanodisc, its formation and role in the transmembrane protein stabilization in the absence and in the presence of exogenous lipids. Finally, a biochemical approach will be shown, how to reconstruct *in vitro* the tripartite complex sandwiched in between two Nanodiscs from separately purified protein partners stabilized into Nanodiscs.

1. Presentation of the Nanodiscs

The Nanodiscs are circular patches of phospholipid bilayer maintained by two membrane scaffold protein (MSP) copies. The MSP protein is derived from Apolipoprotein A-1 (ApoA-1) (Bayburt and Sligar, 2002, Denisov *et al.*, 2004) and presents a modified sequence at the N-terminal end. The latter contains a hexa-histidine tag and a linker in between the tag and the MSP sequence. The linker contains a protease site which enables cleavage of the tag from the main MSP sequences. The Nanodisc system is a versatile tool for stabilizing various transmembrane proteins in detergent-free buffer. The transmembrane proteins enshrined into Nanodiscs could be separated from empty Nanodiscs by purification using

His-tag or by size exclusion chromatography when molecular weight of both is significantly different.

The first engineered MSP, MSP1 was based on the ApoA-1 sequence without comprising the globular N-terminal domain (deletion of the first 43 amino acids). The MSP1 presents a 6 His-tag followed by a linker in N-terminal end (Figure 19) and seven helical segments of ApoA-1 until the C-terminal end. The original construct of the MSP1 is constituted of 200 amino acids. The MSP1 was engineered to establish a MSP1 library by generating constructs which are differing in size due to amino acid inserts of different lengths. As an example the MSP1E1, MSP1E2, and MSP1E3 of the engineered MSP1 are present respectively 22, 44, and 66 amino acid sequence insertions.

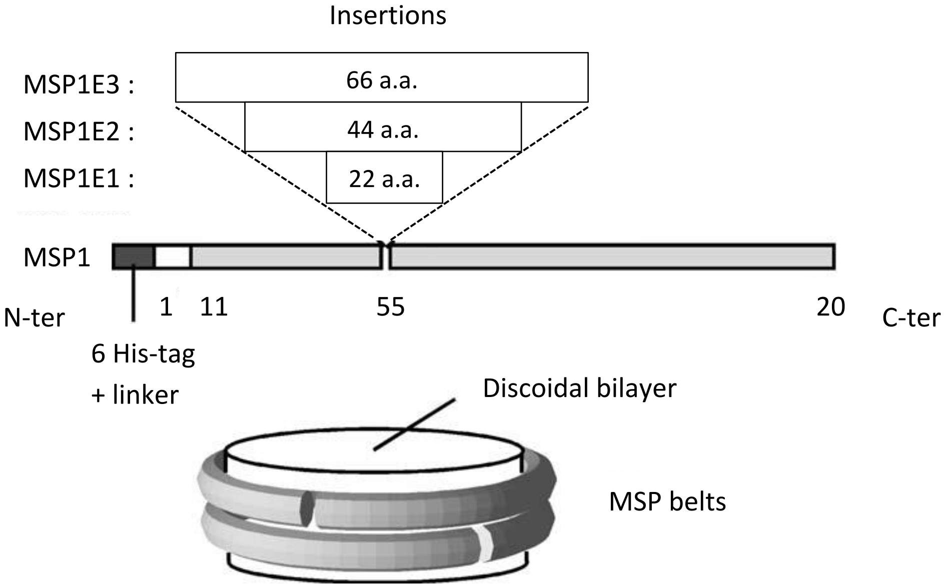

Figure 19- Schematic representation of MSP constructs used for Nanodisc formation

The schematic representation shows the MSP1 and its engineered versions according to the chosen insert of different lengths. The arrangement of two MSP is modelled as MSP belt around discoidal bilayer. Adapted from Bayburt *et al.*, 2006.

The MSP1 could wrap approximately 160 to 340 phospholipids. The Nanodisc structure is characterized by two MSPs forming a double-belt shielding the acyl chains of the lipid molecules (Figure 19).

The next paragraphs will present the MSP1D1 and MSP1E3D1, which were chosen for the stabilization of individual proteins needed for the tripartite complex reconstruction.

The MSP1D1 is a MSP1 molecule which was deleted in the first 11 residues (Denisov *et al.*, 2004). The MSP1D1 available from Addgene presents a 7 His-tag followed by a spacer sequence and TEV protease site at the N-terminal end (Figure 20). The MSP1D1 Nanodiscs are approximately 9.7 nm in diameter and comprise 120 to 160 phospholipids. The Nanodisc thickness could vary from 4.6 to 5.6 nm. The MSP1D1 is wrapping the discoidal phospholipid bilayer, thus the missing residues are not participating in the helical belt formation. The MSP1E3D1 is an extended version of MSP1D1, the amino acid sequence was modified by insertion of helical domains 4 to 6, after the helical domain 6 (Figure 20).

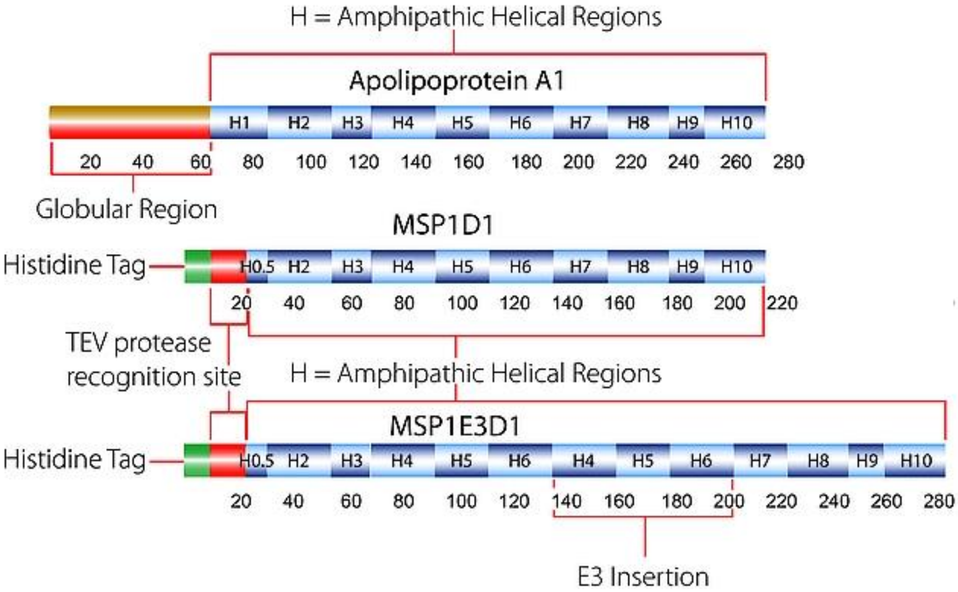

Figure 20- Schematic representation of the Apolipoprotein A-1 and the engineered constructs of the MSP1D1 and MSP1E3D1

The figure represents the protein maps of ApoA-1, MSP1D1 and MSP1E3D1 with their sequence similarities and differences. Illustration comes from Sigma-Aldrich Company product information sheet.

The Nanodiscs could vary in size due to MSP sequence which could present different number of amphipathic helices punctuated by prolines and glycines. By considering these differences, the Nanodisc could present a size ranging from 9.8 to 17 nm in diameter (Ritchie *et al.*, 2009) which enables accommodation of various transmembrane proteins as shown for cytochrome P450 (Bayburt and Sligar, 2002), bacteriorhodopsin () or more recently TRPM4 (Autzen *et al*., 2018). The ratio of phospholipid: MSP could also affect the Nanodisc size and stoichiometry optimization allows obtaining self-assembled uniform Nanodiscs. The lipid nature influences the Nanodisc size. A mean diameter of 5.2, 5.7, 6.9 nm has been measured for respectively 1,2-dipalmitoyl-sn-glycero-3-phosphocholine (DPPC), 1,2-dimyristoyl-sn-glycero-3-phosphocholine (DMPC) and 1-palmitoyl-2-oleoyl-sn-glycero-3-phosphocholine (POPC) empty Nanodiscs (Bayburt and Sligar, 2002; Denisov *et al.*, 2004; Bayburt *et al.*, 2006).

POPC (Figure 21) is the phospholipid which was chosen for the transmembrane protein stabilization during Nanodisc formation. The latter is considered to be a model lipid for biophysical experiment, able to form lipid bilayers mimicking biological membranes (Ritchie *et al.*, 2009). The POPC Nanodiscs are stable in liquid crystalline state above 4.8°C.

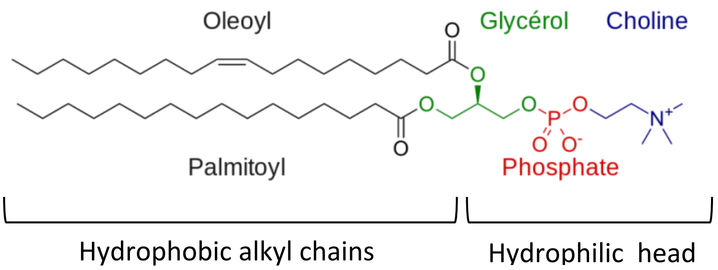

Figure 21- Schematic representation of POPC

The POPC lipid contains two hydrophobic alkyl chains and a hydrophilic head.

2. Nanodisc preparation for transmembrane protein stabilization

The following paragraphs will present in detail the steps leading to the insertion of the transmembrane protein OprM and MexB in lipid Nanodiscs using the standard method proposed by Sligar and co-workers. During my thesis, I have developed an alternative method which consists in a reconstitution in a minimal Nanodisc without adding exogenous lipids. This new method is also presented in this chapter.

2.1. Expression and purification of MSP1D1 and MSP1E3D1

The two membrane scaffold proteins, MSP1D1 and MSP1E3D1 were expressed and purified from *E. coli* according to the standard protocol described by Sligar's group (Ritchie *et al.*, 2009) with some modifications described in Daury *et al.*, 2017. BL21 Gold (DE3) strains were transformed with pET28a His-MSP1D1 or pET28a His-MSP1E3D1 plasmids purchased from AddGene and plated on a petri dish (Luria broth (LB) agar medium) supplemented with kanamycin at 30 µg/ml. After one night at 37 °C, a clone resistant to kanamycin was taken up in 5 ml of LB medium supplemented with kanamycin (30 µg/ml). This pre-culture was incubated at 37 °C with overnight shaking (200 rpm). This pre-culture was used to inoculate 100 ml of LB medium, which were then incubated at 200 rpm and 37°C until an OD at 600 nm of 0.6-0.8 is reached (approximatively 3h). Once the desired OD was reached, 1 mL of 0.1 M IPTG (Isopropyl β-D-1 thiogalactopyranoside) was added to the culture, which continued to incubate under the same conditions for 3h. The culture was centrifuged for 10 min at 8000 g at 4 °C.

The pellet was taken up in 3mL of 20mM phosphate buffer pH 7.4, to which 1mM PMSF, 1% Triton X100, 0.125 g of DNase and 50mM imidazole were then added. The sample was sonicated 6 times during 30 seconds and centrifuged for 40 min at 21200g at 4 °C. The supernatant was then applied, in an 8ml closed column, to 2ml pre-equilibrated Ni-NTA resin (Invitrogen) and incubated 2h at 4 °C. After 1 min of centrifugation at 800g, the supernatant is removed and the column is incubated with buffer 1 (40 mM Tris/HCl pH 8, 300 mM NaCl with 1% Triton X100), buffer 2 (40 mM Tris/HCl pH 8, 300 mM NaCl with 50 mM Na-cholate) and buffer 3 (40 mM Tris/HCl pH 8, 300 mM NaCl with 70 mM imidazole). A centrifugation of 1 min at 800 g is carried out between each wash. The elution is then perform by depositing 3 ml of 40 mM Tris/HCl pH 8 buffer with 300 mM NaCl and 400 mM imidazole at the top of the column. At the end, the column is opened and 6 fractions of 0.5 ml are collected.

After SDS-PAGE analysis of the samples, the imidazole of the selected fractions is removed by dialysis. The concentration of proteins is measured with a Nanodrop 1000 (Thermoscientific) at 280 nm and the concentration is adjusted to at least 2 g/l using an Amicon filtration with a cutoff of 10 kDa (Merck Millipore).

2.2. Lipid preparation for classic Nanodisc formation

1-palmitoyl-2-oleoyl-sn-glycero-3-phosphocholine (POPC) lipids, purchased from Avanti Polar, were dissolved in chloroform, dried onto a glass tube under steady flow of nitrogen and followed by exposure to vacuum for 1 h. The lipid film was suspended in the reconstitution buffer (100 mM NaCl, 10 mM Tris/HCl, pH 7.4) and subjected to five rounds of sonication for 30 seconds each. Lipid concentration was quantified by phosphate analysis.

2.3. Expression and purification of MexA, MexB and OprM

The protein partners of the tripartite complex MexA-MexB-OprM were separately expressed and purified, MexA and MexB following the protocol described in Verchère *et al.*, 2014 and OprM following the protocol described in Phan *et al.*, 2010.

2.4. Reconstitution of transmembrane proteins into Nanodiscs

MexA, MexB and OprM were inserted into Nanodiscs following the standard protocol described by Sligar's group (Denisov *et al.*, 2004; Ritchie *et al.*, 2009) with some modifications described in Daury *et al.*, (2017). In this previous work the MexB and OprM were stabilized into Nanodisc and characterized by an average image in negative staining TEM.

Here, the OprM-ND was obtained by mixing the solutions of POPC liposome and MSP with OprM at a final 36:1:0.4 lipids/MSP/protein molar ratio in a 10 mM Tris/HCl, pH 7.4, 100 mM NaCl, 30 mM octyl-β-glucoside (OG) and 15 mM Na-cholate solution. Detergent was removed with nonpolar polystyrene beads (SM2 Bio-beads from Bio Rad) overnight at 4 °C.

The OprM-ND was characterized by negative staining with 2% uranyl acetate in TEM (Figure 22). The carbon coated grid was glow discharged at 2.6 10^{-1} mbar, 2.6 mA. The 5 µl of OprM-ND sample at 0.004 g/l was incubated at carbon side over 30 seconds before blotting. The negative staining was performed with 5 µl of 2% uranyl acetate for 2 minutes before blotting and grid drying.

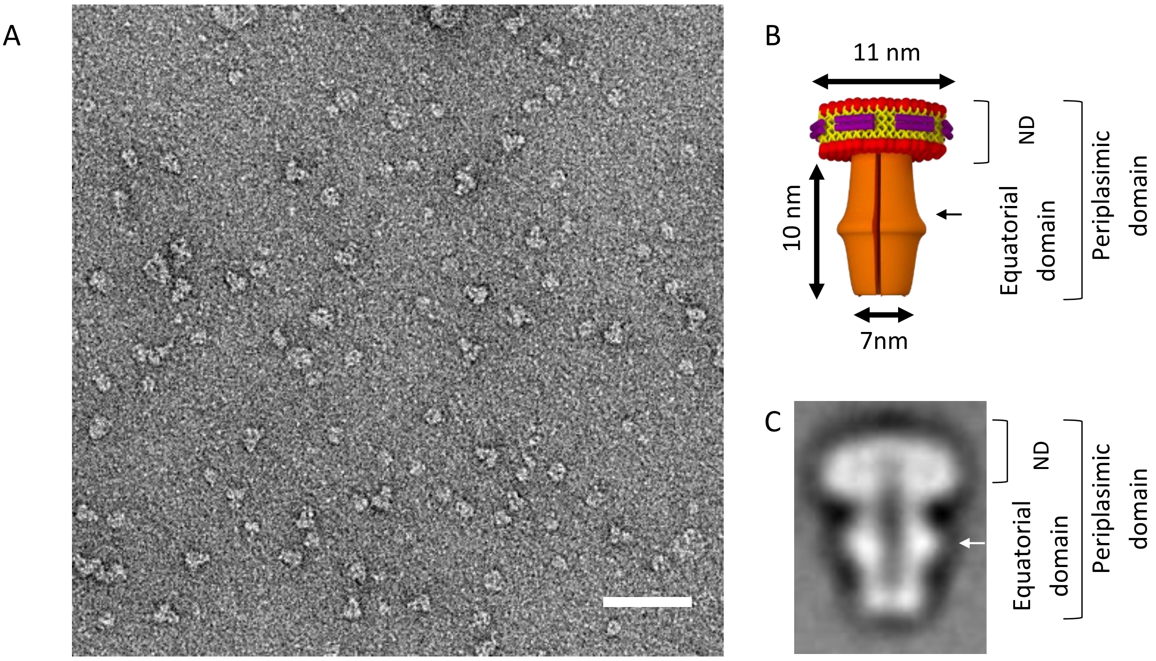

Figure 22- OprM-ND characterized in negative staining TEM

Field of view of OprM-ND negatively stained (scale bar 50nm). The micrograph shows white densities which correspond to the Nanodisc and the periplasmic domain of OrpM protruding from the Nanodisc (A). The average image of OprM (C), obtained from approximately 200 images, presents the Nanodisc at the top followed by the periplasmic part of OprM with a bulge corresponding to the equatorial domain and schematically represented in B.

The POPC liposome and MSP were mixed to MexA, MexB at a final 33:1:0.5:4.5 lipids/MSP/MexB/MexA molar ratio in a 10 mM Tris/HCl, pH 7.4, 100 mM NaCl and 15 mM Na-cholate solution (Figure 23, step 1). After detergent removal by the addition of SM2 Bio-beads shaken overnight at 4 °C (Figure 23, step 2), MexA and MexB were inserted into Nanodics.

The MexA-MexB-ND was characterized by negative staining with 2% uranyl formate in TEM (Figure 23). The carbon coated grid was glow discharged at 2.1 10^{-1} mbar, 2.1 mA. The 5 µl of MexA-MexB-ND sample at 0.06 g/l was incubated at carbon side over 30 seconds before blotting. The negative staining was performed with 5 µl of 2% uranyl formate for 2 minutes before blotting and grid drying.

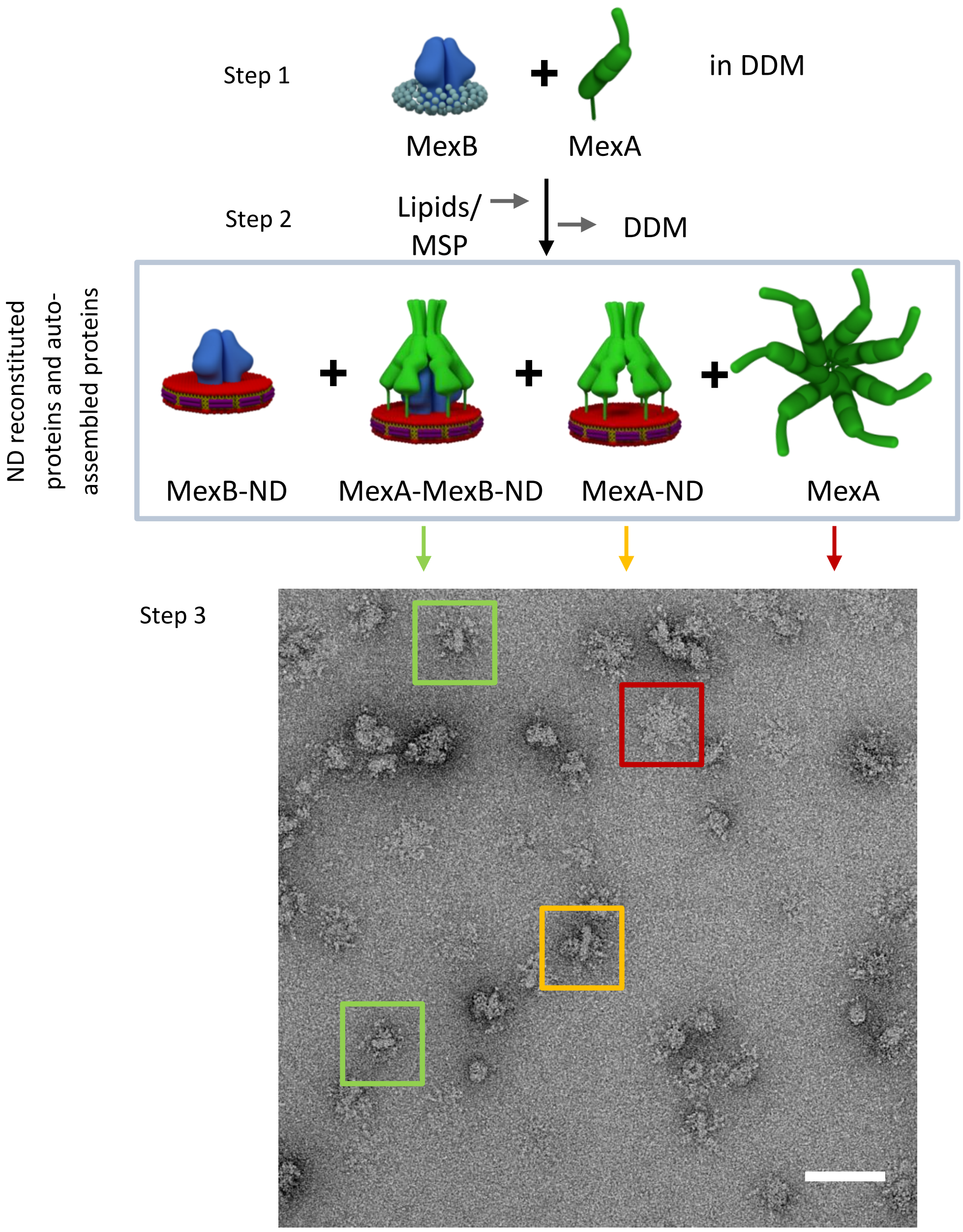

Figure 23- MexA-MexB-ND characterized in negative staining TEM

Field of view of MexA-MexB-ND negatively stained (scale bar 50nm). The reconstituted sample presents numerous types of objects which were highlighted on the EM image and represented schematically (grey box): MexB-ND (not seen at this image), MexA-MexB-ND bipartite (green), MexA-ND (orange) and oligomerized MexA in hexameric rosette (red).

3. Self-assembling of MexA-MexB-OprM tripartite efflux complex

The OprM-ND and MexA-MexB-ND were mixed together which leads to the tripartite complexes formation.

The tripartite complexes from the initial mixed samples were submitted to size exclusion chromatography (SEC) with a Superose 6 column (Figure 24). The SEC column was pre-equilibrated with reconstitution buffer which was also used as running buffer. Peak fractions were collected on a micro-Akta (GE Healthcare).

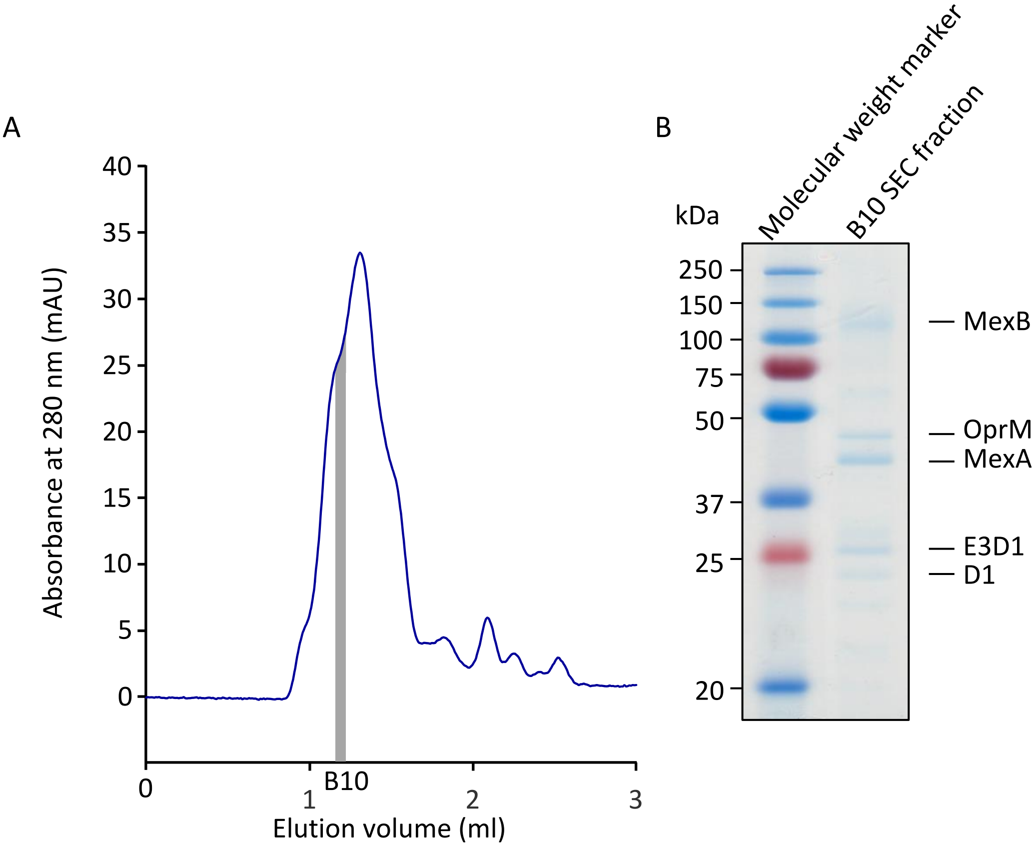

Figure 24- Characterization of MexA-MexB-OprM efflux complex by size-exclusion chromatography and Coomassie-stained SDS-PAGE analysis

The elution profile of the SEC (A) presents a main peak comprising tripartite complex enriched in B10 at 1.2ml elution volume followed by individual ND. The collected elution fractions are about 50 µl. The Coomassie-stained SDS-PAGE gel was realised for control of the B10 elution fraction (B).

The SDS-PAGE analysis (Figure 24 B) and negative staining in TEM (Figure 25) of the B10 fraction (Figure 24 A) show that this fraction contained mainly MexA-MexB-OprM complex. The sample will be used for cryo-EM preparation. Detailed experiments are presented in the next chapter.

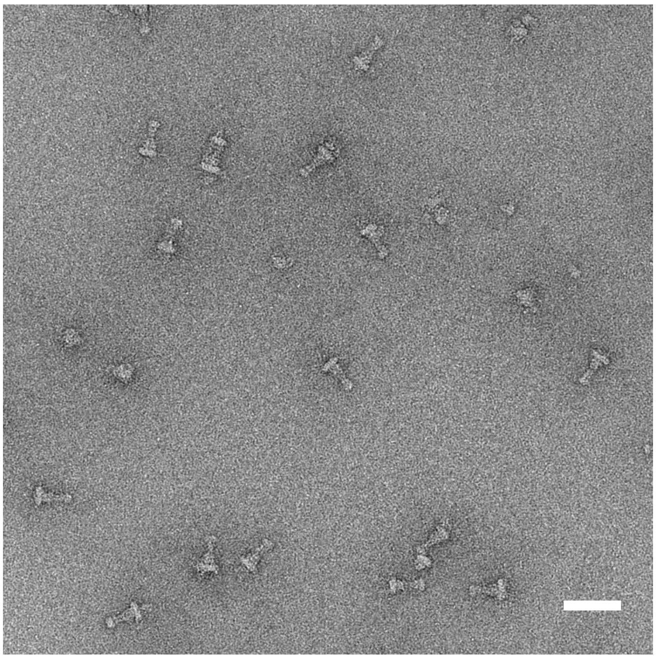

Figure 25- MexA-MexB-OprM sandwiched in between two ND characterized in negative staining TEM

The negative staining of the B10 fraction (1/60 dilution) allows confirming the sample enrichment in tripartite efflux complexes and estimation of sample concentration for cryo-EM sample preparation (scale bar 50nm).

4. Minimal Nanodisc without adding exogenous lipids for stabilizing membrane proteins in detergent-free buffer

Mechanistic comprehension of membrane proteins is essential to understand underlying complex cellular mechanisms. Membrane proteins are not soluble and need to be stabilized for being studied. Thus, it is mandatory to imagine convenient and minimal tools for protein stabilization. The idea comes up to simplify the lipid Nanodisc to minimal Nanodisc. As a consequence the membrane proteins are stabilized by only membrane scaffold proteins MSP in detergent-free buffer.

Minimal nanodisc without exogenous lipids for stabilizing membrane proteins in detergent-free buffer

Dimitri Salvador[1,2$], Marie Glavier[1,2 $], Guy Schoehn[3], Gilles Phan[4], Jean-Christophe Taveau[1,2], Marion Decossas[1,2], Sophie Lecomte[1,2], Cyril Garnier[4], Isabelle Broutin[4], Laetitia Daury[1,2§], Olivier Lambert[1,2§]

[$]Equally contributing first authors,
[§]Equally contributing last authors

[1]Univ. Bordeaux, CBMN UMR 5248, Bordeaux INP, F-33600 Pessac, France.
[2]CNRS, CBMN UMR5248, F-33600 Pessac, France,
[3] Université Grenoble Alpes, CNRS, CEA, Institute for Structural Biology (IBS), 38000, Grenoble, France.

[4] Laboratoire de Cristallographie et RMN Biologiques, UMR 8015, CNRS, Université Paris Descartes, Faculté de Pharmacie, 4 Avenue de l'Observatoire, 75006, Paris, France.

To whom correspondence should be addressed: Olivier Lambert, CBMN, UMR CNRS 5248, Université Bordeaux, Institut National Polytechnique Bordeaux, Allée Geoffroy Saint-Hilaire 33600 Pessac, France.
Tel: +33-540006829 and +33-540002200; Email: o.lambert@cbmn.u-bordeaux.fr

Keywords: Membrane protein, nanodisc, lipids, CryoEM

Abstract

Membrane protein stabilization after detergent solubilization presents drawbacks for structural and biophysical studies, in particular that of a reduced stability in detergent micelles. Therefore, alternative methods are required for efficient stabilization. Lipid nanodisc made with the membrane scaffold protein MSP is a valuable system but requires a fine optimization of the lipid to protein ratio. We present here the use of the scaffold protein MSP without added lipids as a minimal system to stabilize membrane proteins. We show that this method is applicable to α-helical and β-strands transmembrane proteins. This method allowed cryo-electron microscopy structural study of the bacterial transporter MexB. A protein quantification indicates that MexB is stabilized by two MSP proteins. This simplified and efficient method proposes a new advance in harnessing the MSP potential to stabilize membrane proteins.

1. Introduction

Membrane proteins play key roles in cellular activities and are major targets for medicinal drugs. One hurdle that limits their studies is related to their structural organization. They expose a hydrophobic surface that demands its incorporation into biological membranes. A major challenge for biochemical, biophysical and structural studies, is maintaining membrane proteins in a lipid-like environment for keeping them stable and monodisperse in solution. In order to maintain membrane protein integrity, various solutions for mimicking native lipid-bilayer environments have been described.

Scaffolding systems form a belt around the hydrophobic part of the membrane protein and unlike liposomes, these systems can stabilize membrane proteins as nanometer-size single particles. Scaffolding systems are based on polymers, peptides and proteins. Amphiphilic polymers (Amphipol and SMA) have been developed to stabilize the proteins after detergent exchange and to extract the proteins directly from their native lipid membrane [1,2]. Engineered amphipathic helices and β-sheet peptides are relatively efficient to form lipid nanodisc or to stabilize membrane proteins but present solubility and stability issues [3–5]. Lipoprotein such as apolipoprotein or saposin are potential scaffold proteins to form lipid nanoparticles after detergent removal [6,7]. Proteins in lipid nanoparticles, based on apolipoproteins ApoA1, also termed nanodiscs [8], have been used frequently for biochemical and biophysical studies of membrane proteins and have also been applied for structure determination by single-particle cryo-EM [9–12].

The rationale for the reconstitution of the integral membrane proteins into lipid nanodiscs (ND) is based on the use of a membrane scaffold protein and extra lipids forming the lipid bilayer. Upon detergent removal, the membrane proteins are inserted into a lipid bilayer containing NDs whose size is limited by the membrane scaffold protein (MSP) [13] wrapped around the hydrophobic core of the lipids. A major difficulty of forming protein-ND is the control of the number of protein molecules per nanodisc. From our previous results, we have observed that this parameter can be tuned by adjusting the lipid to protein ratio but remains tedious to determine because of the system complexity consisting in two proteins that interplay with lipids [14]. Therefore, we explore the formation of a minimal nanodisc without added exogenous lipids.

Here, we present the reconstitution of membrane proteins with the scaffold protein MSP without added extra lipids. We report a methodology to stabilize representatives of β-strand and α-helical transmembrane proteins with MSP as isolated particles amenable to structural EM studies. This minimal method of the nanodisc formation provides a suitable and straightforward approach for structural studies of individual membrane proteins.

2. Methods

2.1 Materials and reagents

1-palmitoyl-2-oleoyl-*sn*-glycero-3-phosphocholine (POPC) was purchased from Avanti Polar Lipids (USA), sodium cholate hydrate, octyl-β-D-glucopyranoside (OG) and *n*-Dodecyl β-D-maltoside (DDM) were purchased from Sigma-Aldrich. SM2 Bio-beads was obtained from Bio-Rad. Superose 6 3.2/300 column was purchased from GE Healthcare. Cu 300 mesh grids and C-flat grids were obtained from Agar Scientific and Protochips respectively.

2.2 Lipid preparation

POPC lipids were dissolved in chloroform, dried onto a glass tube under steady flow of nitrogen and followed by exposure to vacuum for 1 hour. The lipid film was suspended in the reconstitution buffer (100mM NaCl, 10mM Tris/HCl, pH 7.4 (Buffer 1)) and subjected to five rounds of sonication for 30 seconds each. Lipid concentration was quantified by phosphate analysis.

2.3 Protein preparation

Two membrane scaffold proteins, MSP1D1 and MSP1E3D1 (genetic constructs available from AddGene) were expressed and purified from bacteria [13]. MexB and OprM membrane proteins were expressed and purified from bacteria as previously described for MexB [15], and OprM [16,17]. After purification, protein buffers contained 0.03% *n*-Dodecyl β-D-maltoside for MexB and 0.9 % n-octyl-β-D-glucopyranoside for OprM.

2.4 MSP histidine tag cleavage

The linker connecting the histidine tag to the MSP protein contains a recognition site for the AcTEV protease enzyme. Digestion of 1 mg of MSP1E3D1 was performed by incubation with 500U of AcTEV (Invitrogen) at room temperature for 5 h, following the manufacturer's protocol. The tag-less protein was obtained in the flow through fraction after passage on a Ni-NTA agarose resin (Invitrogen).

2.5 Preparation and purification of MexB-ND, MexB-MSP, OprM-ND and OprM-MSP.

MexB was inserted into NDs according to the standard protocol [13,14]. Briefly, to obtain MexB-ND, MexB was mixed with POPC and MSP1E3D1 with or without its His-tag, at a final 32:1:0.5 lipid:MSP:protein molar ratio in a 10 mM Tris/HCl pH 7.4, 100 mM NaCl buffer with 0.03% DDM and 15 mM Na-cholate (Buffer 2). Unless stated otherwise, molar ratios are calculated based on the monomeric forms of the proteins considered. Detergent was removed by the addition of SM2 Bio-beads into the mixture shaken overnight at 4°C. MexB-MSP was obtained following the same protocol without addition of POPC. Samples were then purified by size exclusion chromatography (SEC) on a Superose 6 column at 40µL/min in buffer 1 or by affinity chromatography using a Ni-NTA agarose resin. In the latter case, elution in 10 mM Tris/HCl pH 7.4, 500 mM Imidazole was performed after extensive washing (10CV) to remove excess MSP. Imidazole was then removed by buffer exchange with 10mM Tris/HCl pH 7.4, 100mM NaCl on an amicon ultra 100 000 MWCO by 5 centrifugations at 3000g for 10 min.

For OprM-ND, OprM was mixed with POPC and MSP1D1 at a final 24:1:0.6 lipid:MSP:protein molar ratio in a 10 mM Tris/HCl pH 7.4, 100 mM NaCl buffer with 0.9% β-octylglucoside and 15 mM Na-cholate (Buffer 3). Detergent was removed by SM2 Bio-beads overnight at 4°C. OprM-MSP was reconstituted following the same protocol, without addition of lipids. Samples were then purified by SEC on a Superose 6 column at 40µL/min in buffer 1.

An alternative reconstitution of OprM-MSP and MexB-MSP was performed on spin columns. For OprM-MSP, OprM was mixed with MSP1D1 at a final 1:0.6 MSP:protein molar ratio in buffer 3 and incubated with slight agitation for 1h at 4°C. For MexB-MSP, MexB was mixed with MSP1D1 at a final 1:0.5 MSP:protein molar ratio in buffer 2 and incubated with slight agitation for 1h at 4°C. Equilibration of zeba spin desalting columns (MWCO 7K, Thermo Fisher) was achieved by three centrifugations with 300µL of buffer 1 at 2000g for 1min. Then, the reconstitution mixture was applied onto the column and the complex was collected in the flow through after centrifugation for 2min at 2000g.

2.6 Protein quantification from SDS polyacrylamide gel electrophoresis (SDS-PAGE)

Protein samples were boiled for 10min at 100°C in 1X SDS-PAGE reducing buffer and ran for 1h at a constant voltage of 180V on a 12% polyacrylamide gel following the protocol of Laemmli [18]. Protein bands were stained by overnight incubation in SYPRO ruby gel stain solution (Bio-Rad) with slow agitation. Excess background staining was removed by two successive 30min incubations in a solution containing 10% methanol and 7% acetic acid. The gels were washed one last time in ultrapure water and imaged on a Typhoon 8600 (Molecular dynamics) in fluorescence mode using a green excitation laser (λ=532nm) and the Rox 610 BP 30 emission filter at a normal sensitivity.

The quantification of protein bands was achieved using the gel analyzer plugin of the imageJ software for integration of the area under the peaks. Construction of a standard curve using BSA allowed the determination of the samples protein content in micrograms. The corresponding number of moles for each protein was calculated as follows:

$n_{(MexB)} = \mu g_{(MexB)} \times 10^{-6} \times F_{(MexB)} / MW_{(MexB)}$ and $n_{(MSP1E3D1)} = \mu g_{(MSP1E3D1)} \times 10^{-6} \times F_{(MSP1E3D1)} / MW_{(MSP1E3D1)}$

where $F_{(MexB)}$ and $F_{(MSP1E3D1)}$ are correction factors equal to 0.8 and 1.3 respectively calculated from the ratio of the slopes (s) for the standard curves of MexB, BSA and MSP1E3D1 ($F_{(MexB)} = s_{(BSA)} / s_{(MexB)} = 0.8$; $F_{(MSP1E3D1)} = s_{(BSA)} / s_{(MSPE31D1)} = 1.3$). Finally, in order to account for the trimeric nature of MexB, we multiplied by 3 the molar ratio of MSP to MexB.

2.7 Lipid content characterized by attenuated total reflection fourier transform infrared spectroscopy (ATR-FTIR)

Polarized ATR-FTIR spectra were recorded on a Nicolet 6700 FT-IR spectrometer (Nicolet Instrument) with a spectral resolution of 4 cm^{-1}. MexB samples at 0.5 mg/mL were deposited on the crystal in a 10µL droplet. The surface was washed twice with Tris/HCl 10mM pH 7.4, 100mM NaCl and the spectra of the adsorbed molecules were recorded with a parallel (p) and perpendicular (s) polarization of the incident light. The observation of characteristic absorption bands for protein and lipid molecules and comparison of their relative intensities across the different samples allowed for the assessment of lipid content for each specimen.

2.8 Negative stain electron microscopy

For EM grid preparation, a diluted mixture of MexB-MSP (at 0.005 mg/ml) or OprM-MSP (at 0.01 mg/ml) samples was applied to a glow-discharged carbon-coated copper 300 mesh grid and stained with 2% uranyl acetate (w/v) solution. Images were recorded under low dose conditions on F20 electron microscope operated at 200kV using a Eagle 4k x 4k camera (FEI). 1902 and 2413 particles were manually picked from 300 and 50 micrographs for MexB and OprM respectively, and image alignment and two-dimensional averages were performed using Eman2.

2.9 Single particle cryo-electron microscopy

MexB-MSP was characterized in a second time by single particle analysis in cryo-electron microscopy. Holey carbon grids (300mesh R2/1 C-Flat) were treated with a glow discharge before a deposition of a 3µl aliquot at 4 mg/ml for 1 minute. The grid was blotted for 1s (Whatmann paper ashless 42), rapidly plunged and frozen in liquid ethane using EMGP (Leica) with 5°C controlled temperature and 60% regulated hygrometry. The grids were stored in liquid nitrogen before grid checking and imaging. The data collection of MexB-MSP was carried out automatically on a Polara (FEI) operated at 300kV using K2 Summit direct electron detector (GATAN). A data set of 445 dose fractionated micrographs was recorded in counting mode with a pixel size of 1.21 Å. Each micrograph was collected as 40 movie frames of 0.15 s with a dose rate of 1 $e^- Å^{-2} s^{-1}$ each. The total dose was about 40 $e^- Å^{-2}$. Images were recorded using the automated acquisition program Latitude S from Gatan with defocus values ranging from -1.5 to -3 µm.

All movie frames were corrected for gain reference and aligned using Motioncorr2 [19]. Contrast transfer function (CTF) parameters were estimated using Gctf [20]. Further image processing was done in RELION2.1. Initial particle picking consists in a manual-picking of

1181 particles to calculate 2D references. These 2D templates were low-pass filtered to 20 Å to limit reference bias and used for automated picking of all micrographs. A total of 50,722 particles from 233 micrographs was picked. After a 2D classification, 50,522 particles were selected for further analyses. A particle subset was used to calculate a 60 Å low-pass filtered initial model. The 50,522 particles were subjected to 3D classification into 10 classes with no symmetry imposed. Four classes, exhibiting similar structural features and comprising a total of 24,576 particles were subjected to 3D refinements with C1 symmetry. Since MexB has been described as an asymmetric homotrimer, no symmetry was imposed. The resolution estimation calculated onto two separately 3D refined half-reconstructions with the Fourier shell correlation criterion at 0.143 was 8.4 Å for C1 symmetry reconstruction.

3 Results

3.1 Stabilization of a α-helical transmembrane protein with MSP scaffold protein

We evaluated the ability of MSP1E3D1 to stabilize, in a detergent-free buffer, the MexB drug transporter, as a representative of α-helical transmembrane protein. In Gram-negative bacteria, MexB forms an asymmetric trimer in which each protomer is made of a 12 transmembrane α-helices domain and a large periplasmic part comprising a porter and a funnel domain extending 7 nm away from the inner membrane inside the periplasm. We incubated the detergent-purified MexB protein with MSP1E3D1 at a MSP:MexB molar ratio of 2:1 and then proceeded to the detergent removal with Bio-beads. The sample was thereafter submitted to SEC using a buffer without detergent (buffer 1). The SEC profile showed two peaks; the first peak corresponds to the MexB stabilized with MSP (MexB-MSP) whereas the second peak originates from monomeric MSP (Figure 1A). For comparison, a solution of MexB stabilized in a lipid nanodisc (MexB-ND) submitted to SEC exhibited a comparable elution profile suggesting that MexB-MSP and MexB-ND have similar sizes.

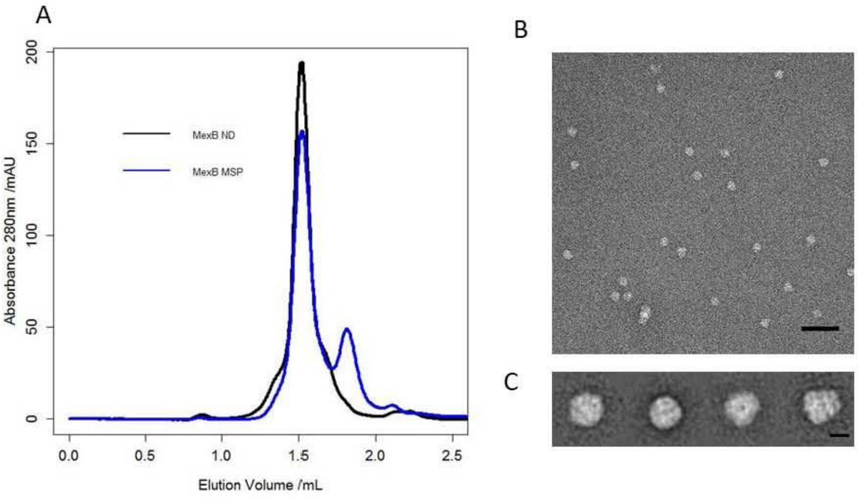

Figure 1: A) Size Exclusion Chromatography elution profiles for MexB-MSP (blue curve) and MexB reconstituted in lipid nanodisc using the same MSP1E3D1 (MexB-ND). For MexB-MSP, an extra peak is observed at 1.8 mL eluted volume, indicating an excess of free MSP. B) Negative stain EM field of the peak at 1.5 mL eluted volume showing homogeneous MexB-MSP particles. Scale bar 50 nm. C) Representative 2D classes of MexB viewed with different orientations. The two average images on the right correspond to top and side views respectively. Scale bars 10 nm.

EM revealed a homogenous population of MexB-MSP molecules (Figure 1B). Averaging 1902 single particles showed side and top views of MexB-MSP in accordance with the trimeric organization of MexB (PDB ID: 2V50) with a continuous layer of electron density for the MSP, including the 36-transmembrane helix domain of trimeric MexB. Furthermore, the periplasmic part of MexB exhibited two clearly distinguishable layers of density, assigned to the porter domain and to the more distal funnel domain (Figure 1C).

3.2 Single particle cryo-electron microscopy of MexB-MSP

We used single-particle cryo-EM to determine the structure of MexB-MSP. We prepared cryo-EM grids of the MexB-MSP by the standard plunge-freezing method. Cryo-EM images showed that the frozen hydrated complexes of MexB-MSP were homogeneous and monodisperse (Figure 2A). We collected a relatively modest cryo-EM data set (455 micrographs) as the purpose of this structural study was conceived as a proof of feasibility but not as the elucidation of MexB structure, which is already known [21]. The 2D class averages displayed thin features of the periplasmic and transmembrane domains of MexB-MSP viewed in various orientations (Figure 2B). After 3D classification, four classes comprising a total of 24,576 particles were used to calculate a 3D reconstruction following a gold-standard refinement procedure at a resolution of 8.4 Å (estimated with the criterion of Fourier shell correlation FSC = 0.143) (Figures 2C, D, E). The Euler angle distribution showed a good spatial coverage of all particles used in the final map (Figure S1 Supplementary materials). No symmetry was imposed as MexB forms an asymmetric homotrimer [21].

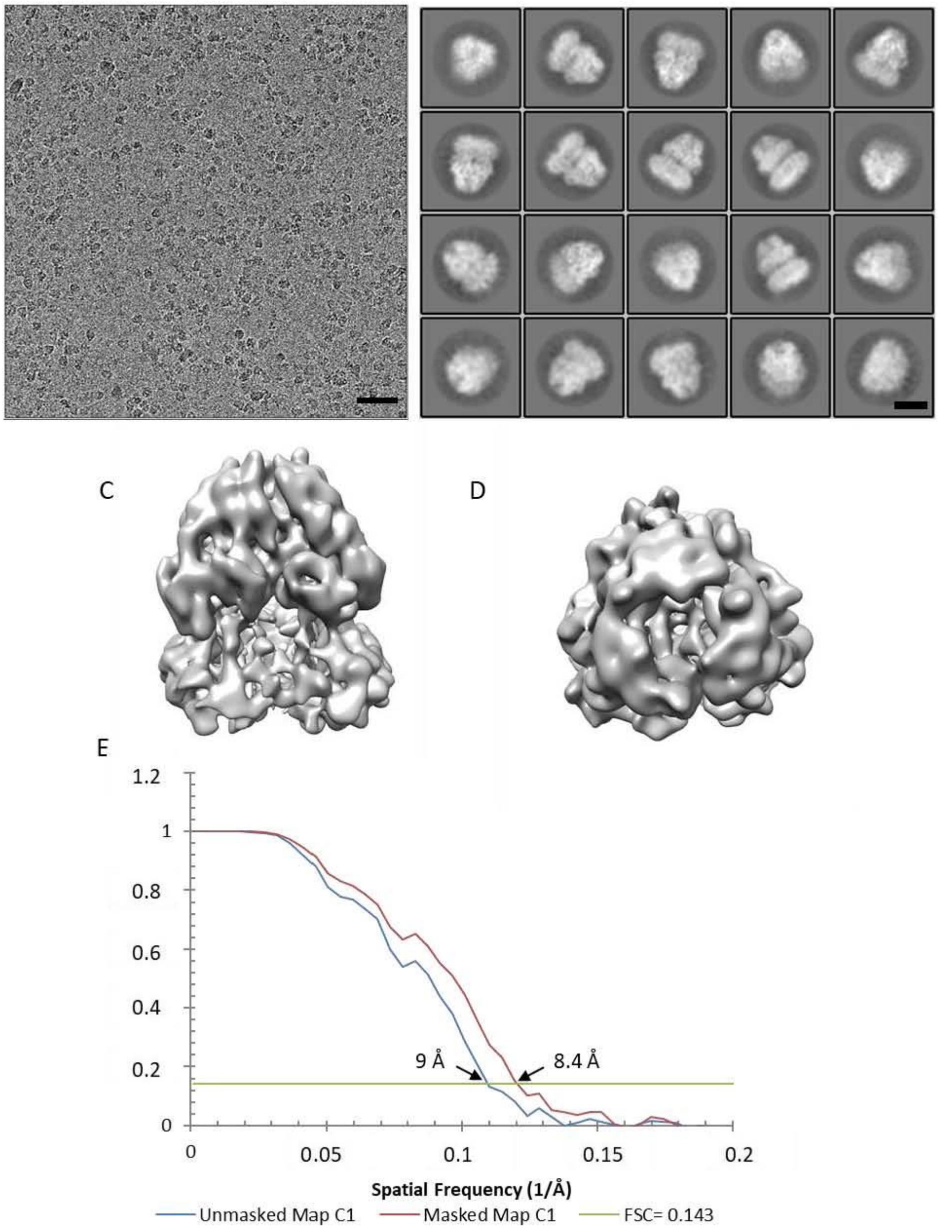

Figure 2: Cryo-EM data and image processing of MexB-MSPE3D1. A) Representative cryo-EM micrograph. Scale bar 50 nm. B) Average images after 2D classification. Scale bar 7 nm. C-D) Side and top views of MexB-MSP cryo-EM reconstruction. E) Resolution curve.

Surface representations of MexB-MSP cryo-EM densities show that the periplasmic core of MexB was better resolved than some domains at the edge of the molecule that seem highly flexible as well as the region that could be attributed to the MSP proteins (Figures 2D-C). The asymmetric MexB crystal structure could be directly fitted within our cryo-EM map without modification. Overall no significant difference was observed between the two structures (Figure 3). The three asymmetric subunits (in access, binding and extrusion conformations as described in the crystal structure [21,22] have been positioned in the C1 cryo-EM map. The secondary structure elements could be assigned within the periplasmic domain which confirms the 8.4 Å resolution. The funnel domains DN and DC were well-accommodated and the α-helices and loops were clearly defined (Figure 3B) as well as the porter domains PC1 and PC2 (Figure 3C). Transmembrane densities exhibited a good fit with transmembrane helices of the Binding and Extrusion subunits from the crystal structure unlike densities corresponding to those of the Access subunit (Figures 3E, G-I). For the latter, the bundle of helices in the EM map was resolved but a small shift was observed with respect to the helices from the crystal. This structural variation may likely be explained by the use of MSP instead of detergent. Such mobility of the helices was already observed when AcrB, *E coli* transporter homologous to MexB was solubilized with SMA [23], suggesting the position of the transmembrane helices are slightly modified by the presence of the stabilizing molecules. In addition, extra densities around MexB could correspond to the MSP molecules but poor resolution did not permit to solve the MSP structure (Figures 3E-I). Overall, the C1 cryo-EM map was in good agreement with the crystal structure and the stabilization with MSP did not induce major changes to the global secondary structure in MexB.

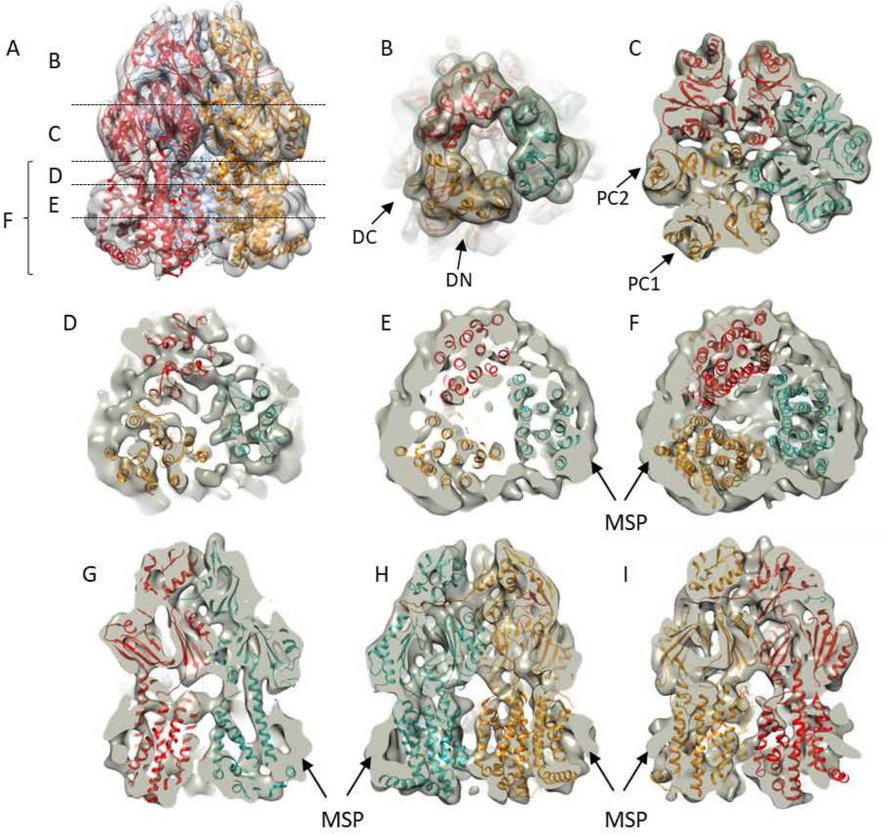

Figure 3: Fitting of MexB crystal structure within the cryo-EM map.

A) Side view of MexB in the cryo-EM map B-F) Transversal sections through the volume showing the fit of each asymmetric subunit colored in red, yellow and blue corresponding to the Access, Binding and Extrusion conformation respectively. Selected position at the level of the funnel domain (B), porter domain (C), transmembrane domain (D-F) marked on A). G-I) Longitudinal sections revealing good fit of transmembrane helices of blue and yellow subunits corresponding to Binding and Extrusion conformations.

3.3. Analysis of MexB-MSP stoichiometry

To determine the stoichiometry of MSP bound per MexB trimer within the MexB-MSP complex, we reconstituted MexB-MSP1E3D1 with a MSP devoid of its His-tag and removed the excess of MSP by affinity purification using the His-tag of MexB. SDS-PAGE of purified MexB-MSP with BSA-standards as a reference (Figure 4) suggested a 2:1 ratio of MSP / MexB trimer (Table 1).

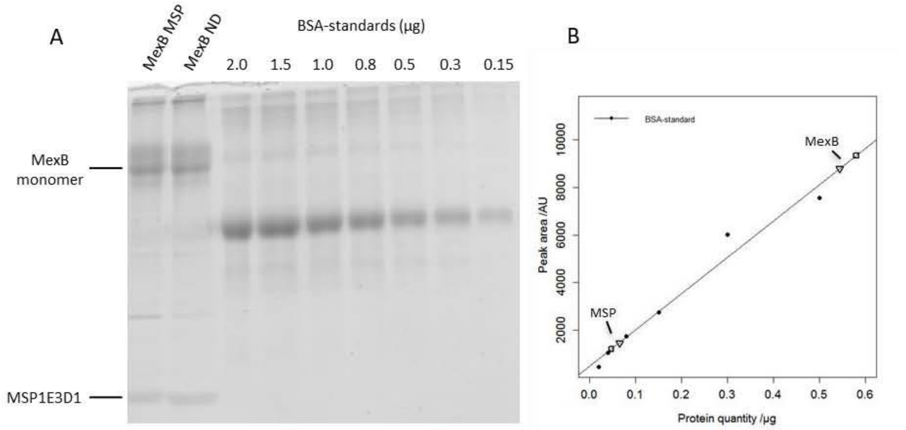

Figure 4: Determination of the molar MSP to MexB ratio by SYPRO ruby quantification.

A) SDS PAGE of MexB-MSP, MexB-ND and BSA-standards. The samples were run on the same gel as the BSA-standards to ensure proper calibration. B) Protein quantities for MexB and MSP1E3D1 were determined for both MexB-ND (triangles) and MexB-MSP (squares) complexes by use of the BSA calibration curve.

Table 1: MSP to MexB trimer molar ratio. Values presented are the average of two independent experiments.

	MSP to MexB molar ratio	
	Mean	*SD*
MexB ND	1.7	0.3

MexB MSP	1.5	0.2

In this range of concentration, the fluorescence intensities of MexB and MSP1E3D1 were proportional to the amount of protein but differed slightly from the BSA-standards at similar concentrations (Figure S2A Supplementary materials). To get an accurate quantification from the BSA standard curve, an adjustment factor using the ratio of their slopes has been applied as described in Materials and Methods (Figure S2B Supplementary materials). For comparison, a MexB-ND sample prepared in a way similar to that of MexB-MSP showed a comparable stoichiometry suggesting that there are two MSP molecules in both MexB-MSP and MexB-ND complexes (Table 1).

3.4. Characterization of lipid content of MexB-ND and MexB-MSP by ATR-FITR

Given that membrane proteins after purification with detergent may conserve some lipid molecules tightly bound to their transmembrane regions, we sought to evaluate if a large amount of residual lipids could be responsible for MexB stabilization by MSP. To this end, reconstitution of MexB-ND2 was performed with a lipid concentration two fold larger than that of MexB-ND, for a characterization of the lipid content using polarized ATR-FTIR. ATR spectra were collected for MexB-MSP, MexB-ND and MexB-ND2 between 4000 cm^{-1} and 600 cm^{-1}. Lipid content was determined by following the absorption bands around 2923 cm^{-1} and 2850 cm^{-1} which correspond to the antisymmetric and symmetric CH_2 stretching modes of the lipid acyl chains respectively (Figure 5). The intensities of the absorption bands are proportional to the molecule concentration and these increased with increasing lipid to protein ratio used for MexB-ND reconstitution. Indeed, a doubling of the lipid to protein ratio resulted in twice as much signal in the CH_2 region, going from $2.3.10^{-4}$ to $4.5.10^{-4}$ at $2920cm^{-1}$ and from $1.0.10^{-4}$ to 2.10^{-4} at $2850cm^{-1}$ for the MexB-ND and MexB-ND2 samples respectively. The presence of amide bands between 1600-1700 (amide I) and

1500-1580 (amide II) clearly demonstrates the presence of the proteins. For all studied samples, comparable intensities were observed, indicating that similar quantities of MexB-ND2 or MexB-ND were adsorbed on the crystal providing further evidence that the difference in signal for the bands at 2923 cm^{-1} and 2850 cm^{-1} was due to different lipid concentrations. Specifically, in the vicinity of the wavenumbers where a lipid contribution should appear, MexB-MSP exhibited only background level absorbance intensity revealing the absence of endogenous lipids surrounding its transmembrane region. Interestingly, when more lipids were used for nanodisc reconstitution, i.e. for MexB-ND2, a characteristic band of the ester carbonyl stretching mode appeared at 1740 cm^{-1} which unequivocally identified the presence of lipids. In conclusion, the MexB-MSP complex was stabilized mainly by direct protein-protein contacts and no significant amounts of leftover lipids were required to accommodate interactions between MexB and its MSP.

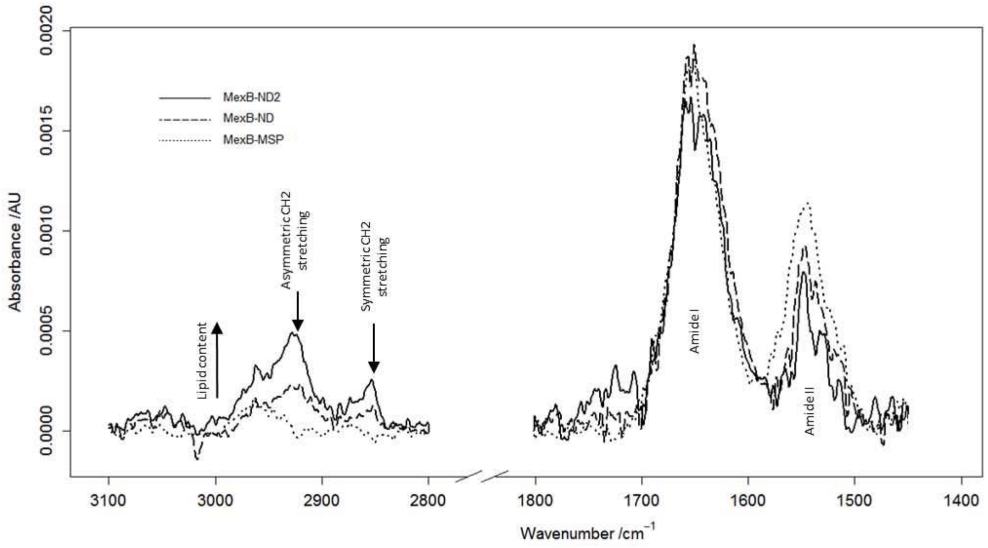

Figure 5: ATR-FITR characterization of lipid content for MexB reconstituted in ND or with MSP alone.

ATR-FTIR *p*-polarized spectra show the presence of lipids for MexB-ND according to the absorption bands at 2923 cm^{-1} and 2850 cm^{-1} (Arrows). Doubling the lipid to protein ratio for MexB-ND reconstitution (MexB-ND2) results in a two-fold increase in the concentration of lipids per nanodisc, as shown by the MexB-ND2/MexB-ND ratio in the CH_2 bands intensity, while the amount of protein adsorbed remains constant as indicated by the intensity of the amide bands (between 1600-1700 cm^{-1} (amide I) and 1500-1580 cm^{-1} (amide II). Unlike MexB-ND, the MexB-MSP spectrum shows undetectable amount of endogenous lipids.

3.5. Stabilization of a β-strand transmembrane protein with MSP scaffold protein

To further determine whether a membrane protein with a smaller transmembrane domain could be stabilized by a MSP alone, we focused on the potential of MSP1D1 to stabilize OprM which possesses a trimeric organization consisting in a β-barrel transmembrane domain of 4-5 nm in diameter. We incubated the detergent-purified OprM protein with MSP1D1 at a MSP:OprM molar ratio of 1:0.6 and then proceeded to remove the detergent with Bio-beads. The SEC profile showed a main peak corresponding to the OprM stabilized with MSP (OprM-MSP) (Figure 6A). OprM reconstituted in lipid nanodisc (OprM-ND) showed a comparable elution profile that appeared thicker than that of OprM-MSP suggesting a higher homogeneity for OprM-MSP. EM analysis of these OprM-MSPs revealed a homogenous population of OprM-MSP molecules with their long axis preferentially oriented parallel to the carbon support which was consistent with the trimeric assembly of OprM (Figure 6B) [24,25]. An average image (from 2413 particles) of OprM-MSP revealed densities related to the MSP at the edge of the duct formed by the OprM β-barrel domain and the 10-nm-long OprM periplasmic domain (Figure 6B, inset). A previous EM characterization of OprM-ND showed also one trimer per ND [14]. Of note, the ND size appeared slightly larger because of the presence of lipids. It appears MSP1D1 without extra lipids also allowed the stabilization of one trimer of OprM.

Our protocol for measuring the OprM/MSP ratio required the removal of the MSP excess using His-tag affinity chromatography and elution of OprM-MSP complexes. Unfortunately, we observed that during this step, a molecular reorganization occurred within these complexes leading to the formation of complexes containing two or three OprM molecules. Therefore, the OprM/MSP ratio has not been determined because the presence of these complexes would have biased the calculation of the number of MSP per OprM trimer. For OprM-ND, the ratio

MSP/OprM indicated that one OprM particle is stabilized by two MSP molecules, like MexB-ND and MexB-MSP (data not shown).

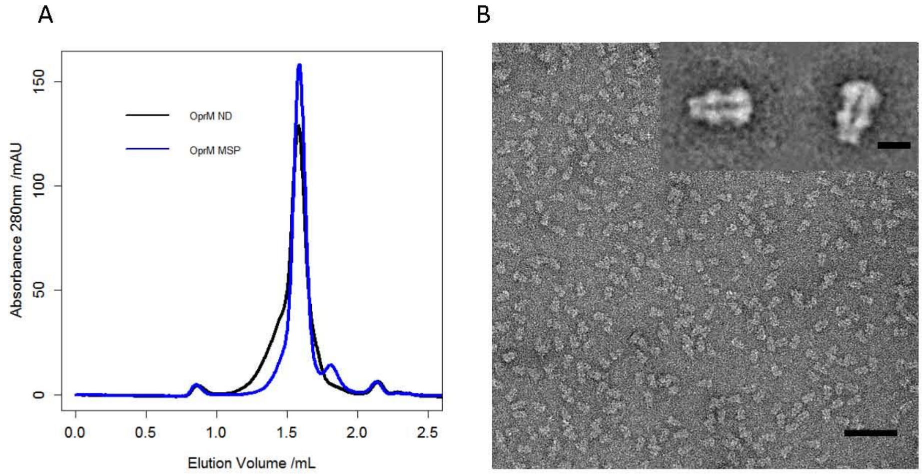

Figure 6: A) Size Exclusion Chromatography elution profiles for OprM-ND and OprM-MSP. In the latter case, an extra peak is observed, indicating an excess of free MSP. Higher molecular weight species are present in the OprM ND reconstitution. B) EM observation of the OprM-MSP fraction shows isolated OprM molecules. Scale bar 50 nm. Inset: Representative class average of OprM negatively stained images. Scale bar 7 nm.

4. Discussion

Nanodiscs currently developed for stabilizing membrane protein in detergent-free buffer use scaffold proteins and extra lipids leading to the formation of a tripartite scaffold-lipid-protein complex [9,26,27]. We have explored the ability of the ApoA1-derived MSP protein to stabilize membrane protein in detergent-free buffer without adding extra lipids for structural and biophysical studies. The formation of MSP-membrane protein complex was carried out by detergent removal.

We successfully stabilized representatives of both β-barrel and α-helical membrane proteins with MSP1D1 and MSP1E3D1. We carried out a cryo-EM structure determination of MexB stabilized by MSP indicating that the overall structure of MexB stabilized by MSP resembles the asymmetric crystal structure of MexB in detergent (Figure 3). Our results also provided evidence that trimeric MexB particles were stabilized by two MSP molecules (Figure 4). In pure lipid nanodiscs, it has been proposed that two MSP molecules form a double-belt shielding the acyl chains of the lipid molecules [27–29]. Likewise, cryo-EM density map showed extra densities around the transmembrane domain of MexB. The MSP densities were poorly resolved probably because of an irregular arrangement of MSP molecules. However, their disposition strongly suggests that the MSP proteins are wrapped around MexB. Moreover, the similar sizes obtained for pure lipid nanodiscs and MexB-MSP suggest a similar arrangement of the scaffolding protein, in a double belt-like pattern, as previously proposed [29].

The stabilization of OprM has been achieved with MSP1D1. The choice of this MSP was driven by our previous data on the formation of OprM-ND [14]. We had been able to reconstitute OprM in nanodisc using this MSP. Therefore, we used the same MSP to stabilize OprM without extra lipids. The EM results after size exclusion chromatography show a homogeneous distribution of OprM molecules (Figure 6). These results indicate that the MSP on its own with no extra lipids, is able to maintain the stability and monodispersity of membrane proteins in a detergent-free buffer even for proteins harboring a rather small transmembrane domain (5 nm in diameter for OprM). It can be assumed that MSP molecules adopt an organization that encircles OprM, as for MexB. Given the MSP flexibility revealed by the cryo-EM structure of MexB-MSP, we expect similar variabilities in MSP structural arrangements around OprM which would hamper the determination of its organization by single particle cryo-EM explaining why we did not pursue further cryo-EM structural investigation.

Stabilizing membrane proteins with MSP in the absence of lipids presents several advantages. First, defining the MexB/MSP ratio to get one trimeric MexB particle per complex seems rather straightforward. As long as MSP is present in a little excess, MexB will be well stabilized. In our experiments, we have used a MSP/MexB ratio of 2. There is no need to add a larger excess of MSP. In the case of lipid nanodisc formation, the addition of lipids may affect the number of MexB protein per ND inducing a certain heterogeneity [30]. This explains why the lipid to protein ratio needs to be finely adjusted to maintain one molecule of MexB per ND. Secondly, the method for removing detergent classically uses polystyrene beads. Another method has also been explored with the use of spin column. The advantage of this method is a much quicker detergent removal than with the Bio-beads. The stabilization of OprM and MexB has been performed with the MSP1D1 and the samples were observed by electron microscopy (Figure S3 Supplementary materials). Both OprM and MexB samples looked homogeneous and similar to those prepared with Bio-beads. For the formation of lipid nanodisc, the rate of detergent removal is important for the bilayer reconstitution. Altogether, the stabilization of membrane proteins with MSP in the absence of additional lipids appears less restrictive.

The ability of scaffolding systems to stabilize membrane proteins without adding extra lipids has been proposed for engineered peptides forming β-strands and α-helices. Such stabilization was successful for the MsbA transporter, rhodopsin and bacteriorhodopsin that are α-helical integral membrane proteins but failed for the β-barrel PhoE porin [3,4]. Very recently a bi-helical peptide has been developed with the ability to stabilize both α-helical and β-barrel membrane proteins [31]. Our results extend this approach to the use of proteins such as MSP containing several helical segments without the need for peptide engineering.

Even though our cryo-EM structure of MexB-MSP revealed the asymmetric structure of MexB encircled by densities attributable to the MSP, it did not permit to describe the interactions of MSP with MexB. Nevertheless, these densities were located in the close vicinity of MexB suggesting a direct interaction of MSP with MexB. This hypothesis is supported by ATR results showing no detectable lipid content associated with MexB (Figure 5), although it cannot be excluded that a few lipids remained strongly bound the membrane protein after its purification and may help its stabilization with the scaffolding protein.

5. Conclusions

Our protocol opens the use of MSP for stabilizing membrane protein without adding extra lipids. This method is less restrictive than that for preparing lipid nanodisc in terms of MSP to protein ratio optimization, detergent removal or even the choice of MSP length. Membrane proteins are well maintained as isolated particles amenable to single particle cryo-EM structural studies. As a scaffold protein, the same MSP can be used with or without extra lipids for stabilizing membrane proteins. This versatile property may emerge as a valuable advantage to use a unique scaffold system instead of several for biochemical, structural and pharmacological characterizations.

Acknowledgments

This work was supported by French national agency ANR (Assembly ANR-17CE11-0028), Bordeaux INP and Conseil Régional d’Aquitaine. This work has benefited from the facilities of UMS3033/US001 (http://www.iecb.u-bordeaux.fr/index.php/fr/plateformestechnologiques) and used the platforms of the Grenoble Instruct-ERIC Center (ISBG: UMS 3518 CNRS-CEA-UGA-EMBL) with support from FRISBI (ANR-10 INSB-05-02) and GRAL (ANR-10-LABX-49-01) within the Grenoble Partnership for Structural Biology (PSB). The electron microscope facility is supported by the Rhône-Alpes Region, the Fondation Recherche Medicale (FRM), the Fonds Européen de Développement Régional (FEDER) and the GIS-Infrastrutures en Biologie Sante et Agronomie (IBISA). DS is recipient of a MENRT fellowship. MG is recipient of a fellowship from Bordeaux-INP and Conseil Régional d'Aquitaine. We thank C. Gounou for technical assistance.

Author contributions

OL, LD, DS, MG designed the project, analysed data and wrote the manuscript. DS, MG, GS carried out experiments. IB, GP, CG developed expression and protein purification protocols. SL advised on ATER experiment. MD, JCT assisted with electron microscopy and image analysis.

Competing financial interests:

The authors declare no competing financial interests.

References

[1] C. Tribet, R. Audebert, J.L. Popot, Amphipols: polymers that keep membrane proteins soluble in aqueous solutions, Proc. Natl. Acad. Sci. U. S. A. 93 (1996) 15047–15050.

[2] T.J. Knowles, R. Finka, C. Smith, Y.-P. Lin, T. Dafforn, M. Overduin, Membrane proteins solubilized intact in lipid containing nanoparticles bounded by styrene maleic acid copolymer, J. Am. Chem. Soc. 131 (2009) 7484–7485. doi:10.1021/ja810046q.

[3] C.E. Schafmeister, L.J. Miercke, R.M. Stroud, Structure at 2.5 A of a designed peptide that maintains solubility of membrane proteins, Science. 262 (1993) 734–738.

[4] H. Tao, S.C. Lee, A. Moeller, R.S. Roy, F.Y. Siu, J. Zimmermann, R.C. Stevens, C.S. Potter, B. Carragher, Q. Zhang, Engineered nanostructured β-sheet peptides protect membrane proteins, Nat. Methods. 10 (2013) 759–761. doi:10.1038/nmeth.2533.

[5] A.N. Larsen, K.K. Sørensen, N.T. Johansen, A. Martel, J.J.K. Kirkensgaard, K.J. Jensen, L. Arleth, S.R. Midtgaard, Dimeric peptides with three different linkers self-assemble with phospholipids to form peptide nanodiscs that stabilize membrane proteins, Soft Matter. 12 (2016) 5937–5949. doi:10.1039/c6sm00495d.

[6] T.H. Bayburt, J.W. Carlson, S.G. Sligar, Reconstitution and imaging of a membrane protein in a nanometer-size phospholipid bilayer, J. Struct. Biol. 123 (1998) 37–44. doi:10.1006/jsbi.1998.4007.

[7] J. Frauenfeld, R. Löving, J.-P. Armache, A.F.-P. Sonnen, F. Guettou, P. Moberg, L. Zhu, C. Jegerschöld, A. Flayhan, J.A.G. Briggs, H. Garoff, C. Löw, Y. Cheng, P. Nordlund, A saposin-lipoprotein nanoparticle system for membrane proteins, Nat. Methods. 13 (2016) 345–351. doi:10.1038/nmeth.3801.

[8] T.H. Bayburt, Y.V. Grinkova, S.G. Sligar, Assembly of single bacteriorhodopsin trimers in bilayer nanodiscs, Arch. Biochem. Biophys. 450 (2006) 215–222. doi:10.1016/j.abb.2006.03.013.

[9] J. Frauenfeld, J. Gumbart, E.O. van der Sluis, S. Funes, M. Gartmann, B. Beatrix, T. Mielke, O. Berninghausen, T. Becker, K. Schulten, R. Beckmann, Cryo-EM structure of the ribosome-SecYE complex in the membrane environment, Nat. Struct. Mol. Biol. 18 (2011) 614–621. doi:10.1038/nsmb.2026.

[10] R.G. Efremov, A. Leitner, R. Aebersold, S. Raunser, Architecture and conformational switch mechanism of the ryanodine receptor, Nature. 517 (2015) 39–43. doi:10.1038/nature13916.

[11] Y. Gao, E. Cao, D. Julius, Y. Cheng, TRPV1 structures in nanodiscs reveal mechanisms of ligand and lipid action, Nature. 534 (2016) 347–351. doi:10.1038/nature17964.

[12] P. Jin, D. Bulkley, Y. Guo, W. Zhang, Z. Guo, W. Huynh, S. Wu, S. Meltzer, T. Cheng, L.Y. Jan, Y.-N. Jan, Y. Cheng, Electron cryo-microscopy structure of the mechanotransduction channel NOMPC, Nature. 547 (2017) 118–122. doi:10.1038/nature22981.

[13] T.K. Ritchie, Y.V. Grinkova, T.H. Bayburt, I.G. Denisov, J.K. Zolnerciks, W.M. Atkins, S.G. Sligar, Chapter 11 - Reconstitution of membrane proteins in phospholipid bilayer nanodiscs, Methods Enzymol. 464 (2009) 211–231. doi:10.1016/S0076-6879(09)64011-8.

[14] L. Daury, F. Orange, J.-C. Taveau, A. Verchère, L. Monlezun, C. Gounou, R.K.R. Marreddy, M. Picard, I. Broutin, K.M. Pos, O. Lambert, Tripartite assembly of RND multidrug efflux pumps, Nat. Commun. 7 (2016) 10731. doi:10.1038/ncomms10731.

[15] V. Mokhonov, E. Mokhonova, E. Yoshihara, R. Masui, M. Sakai, H. Akama, T. Nakae, Multidrug transporter MexB of Pseudomonas aeruginosa: overexpression, purification, and initial structural characterization, Protein Expr. Purif. 40 (2005) 91–100. doi:10.1016/j.pep.2004.10.002.
[16] Y. Ferrandez, M. Dezi, M. Bosco, A. Urvoas, M. Valerio-Lepiniec, C. Le Bon, F. Giusti, I. Broutin, G. Durand, A. Polidori, J.-L. Popot, M. Picard, P. Minard, Amphipol-mediated screening of molecular orthoses specific for membrane protein targets, J. Membr. Biol. 247 (2014) 925–940. doi:10.1007/s00232-014-9707-3.
[17] G. Phan, H. Benabdelhak, M.-B. Lascombe, P. Benas, S. Rety, M. Picard, A. Ducruix, C. Etchebest, I. Broutin, Structural and dynamical insights into the opening mechanism of P. aeruginosa OprM channel, Struct. Lond. Engl. 1993. 18 (2010) 507–517. doi:10.1016/j.str.2010.01.018.
[18] U.K. Laemmli, Cleavage of structural proteins during the assembly of the head of bacteriophage T4, Nature. 227 (1970) 680–685.
[19] X. Li, P. Mooney, S. Zheng, C. Booth, M.B. Braunfeld, S. Gubbens, D.A. Agard, Y. Cheng, Electron counting and beam-induced motion correction enable near atomic resolution single particle cryoEM, Nat. Methods. 10 (2013) 584–590. doi:10.1038/nmeth.2472.
[20] K. Zhang, Gctf: Real-time CTF determination and correction, J. Struct. Biol. 193 (2016) 1–12. doi:10.1016/j.jsb.2015.11.003.
[21] G. Sennhauser, M.A. Bukowska, C. Briand, M.G. Grütter, Crystal structure of the multidrug exporter MexB from Pseudomonas aeruginosa, J. Mol. Biol. 389 (2009) 134–145. doi:10.1016/j.jmb.2009.04.001.
[22] R. Nakashima, K. Sakurai, S. Yamasaki, K. Hayashi, C. Nagata, K. Hoshino, Y. Onodera, K. Nishino, A. Yamaguchi, Structural basis for the inhibition of bacterial multidrug exporters, Nature. 500 (2013) 102–106. doi:10.1038/nature12300.
[23] M. Parmar, S. Rawson, C.A. Scarff, A. Goldman, T.R. Dafforn, S.P. Muench, V.L.G. Postis, Using a SMALP platform to determine a sub-nm single particle cryo-EM membrane protein structure, Biochim. Biophys. Acta. 1860 (2018) 378–383. doi:10.1016/j.bbamem.2017.10.005.
[24] H. Akama, M. Kanemaki, M. Yoshimura, T. Tsukihara, T. Kashiwagi, H. Yoneyama, S. Narita, A. Nakagawa, T. Nakae, Crystal structure of the drug discharge outer membrane protein, OprM, of Pseudomonas aeruginosa: dual modes of membrane anchoring and occluded cavity end, J. Biol. Chem. 279 (2004) 52816–52819. doi:10.1074/jbc.C400445200.
[25] O. Lambert, H. Benabdelhak, M. Chami, L. Jouan, E. Nouaille, A. Ducruix, A. Brisson, Trimeric structure of OprN and OprM efflux proteins from Pseudomonas aeruginosa, by 2D electron crystallography, J. Struct. Biol. 150 (2005) 50–57. doi:10.1016/j.jsb.2005.01.001.
[26] F. Hagn, M. Etzkorn, T. Raschle, G. Wagner, Optimized phospholipid bilayer nanodiscs facilitate high-resolution structure determination of membrane proteins, J. Am. Chem. Soc. 135 (2013) 1919–1925. doi:10.1021/ja310901f.
[27] I.G. Denisov, S.G. Sligar, Nanodiscs in Membrane Biochemistry and Biophysics, Chem. Rev. 117 (2017) 4669–4713. doi:10.1021/acs.chemrev.6b00690.
[28] Y. Li, A.Z. Kijac, S.G. Sligar, C.M. Rienstra, Structural analysis of nanoscale self-assembled discoidal lipid bilayers by solid-state NMR spectroscopy, Biophys. J. 91 (2006) 3819–3828. doi:10.1529/biophysj.106.087072.
[29] S. Bibow, Y. Polyhach, C. Eichmann, C.N. Chi, J. Kowal, S. Albiez, R.A. McLeod, H. Stahlberg, G. Jeschke, P. Güntert, R. Riek, Solution structure of discoidal high-density lipoprotein particles with a shortened apolipoprotein A-I, Nat. Struct. Mol. Biol. 24 (2017) 187–193. doi:10.1038/nsmb.3345.

[30] L. Daury, J.-C. Taveau, D. Salvador, M. Glavier, O. Lambert, Reconstitution of Membrane Proteins into Nanodiscs for Single-Particle Electron Microscopy, Methods Mol. Biol. Clifton NJ. 1635 (2017) 317–327. doi:10.1007/978-1-4939-7151-0_17.
[31] M.L. Carlson, J.W. Young, Z. Zhao, L. Fabre, D. Jun, J. Li, J. Li, H.S. Dhupar, I. Wason, A.T. Mills, J.T. Beatty, J.S. Klassen, I. Rouiller, F. Duong, The Peptidisc, a simple method for stabilizing membrane proteins in detergent-free solution, ELife. 7 (2018). doi:10.7554/eLife.34085.

Minimal nanodisc without exogenous lipids for stabilizing membrane proteins in detergent-free buffer

Dimitri Salvador[1,2$], Marie Glavier[1,2 $], Guy Schoehn[3], Gilles Phan[4], Jean-Christophe Taveau[1,2], Marion Decossas[1,2], Sophie Lecomte[1,2], Cyril Garnier[4], Isabelle Broutin[4], Laetitia Daury[1,2§], Olivier Lambert[1,2§]

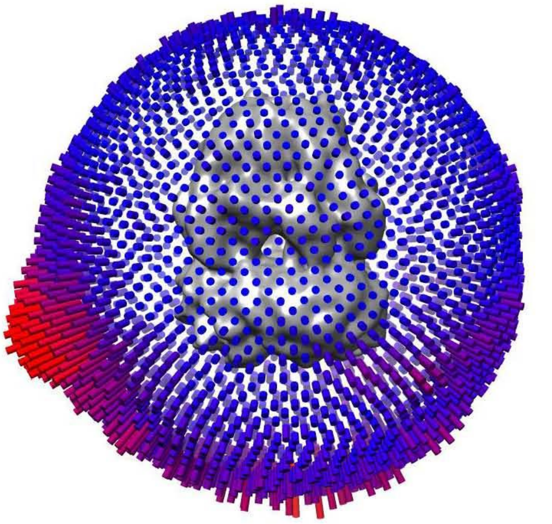

Figure S1: Representation of Euler angle distribution from images used to calculate the 3D reconstruction of MexB-MSP

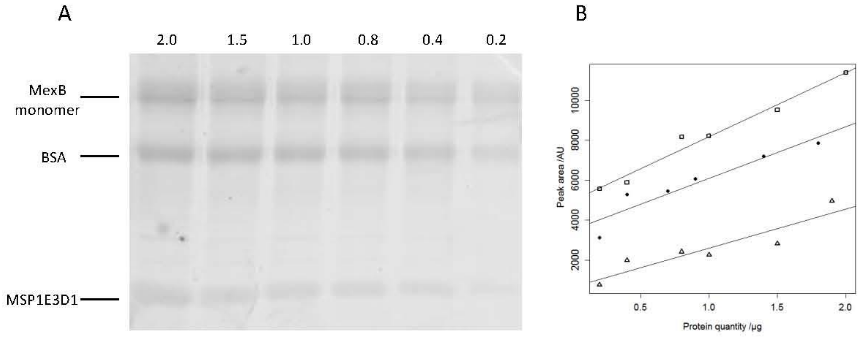

Figure S2-A) SDS PAGE of pure MexB, BSA and MSP1E3D1 for SYPRO ruby quantification. B) Calibration curves. Equal quantities of MexB, BSA and MSPE31D1 result in different calibration curves which would hamper accurate measurements when BSA is used as the reference. To correct for this effect, the ratios of the slope for each protein to that of BSA is determined and used as a correction factor in the equation for the calculation of its number of moles, see materials and methods for more details (MSP: triangles, BSA: full circles, MexB: squares).

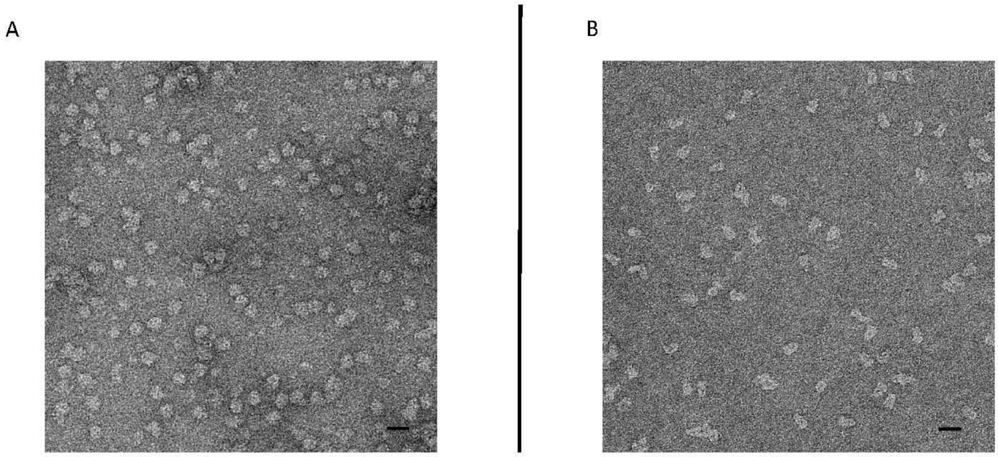

Figure S3: Reconstitution of OprM and MexB-MSP on spin columns. Reconstitution mixtures were first incubated with agitation for 1h and then underwent a 2min centrifugation on spin column with a 7K MWCO. Representative negative stain EM fields are shown for MexB-MSP (A) and OprM-MSP (B). The samples present a homogeneous distribution of particles identical to those observed for the reconstitution method using Bio-Beads . Scale bars 20nm.

The conducted studies showed that the minimal Nanodisc, by the use of MSP and in absence of lipids, allows stabilizing membrane proteins. However, this tool is valuable for investigation of single protein by biophysical and structural studies. The minimal Nanodisc could be limited when studying large and multi-protein complexes.

Chapter 3 – Cryo-EM sample preparation

The following chapter is dedicated to the grid preparation for cryo-electron microscopy (cryo-EM), a crucial step in cryo-EM single particle analysis. If this step is scamped, the biological sample can be irreversibly denatured, protein assemblies can collapse and lead to an inadequate repartition of the particles on the grid, thus the grid can end up useless for data acquisition. As a matter of fact, efforts to improve grid preparation have proven very useful in many cases such as affinity support films with biochemical functionality and continuous carbon support films grid preparation, to retain the particles fare away from air-water interface avoiding protein denaturation. In my case, the MexA-MexB-OprM sample is obtained in rather small quantity, so an additional challenge was to adapt the method of preparation of the grids with the objective to enrich the sample on the grid.

1. Introduction to cryo-electron microscopy

In structural biology, the recent developments in cryo-electron microscopy start to challenge the X-ray crystallography. Both techniques aim at elucidating the structure of single proteins to more complex macromolecular assemblies involved in biological mechanisms. Cryo-EM developed in the 1970s and 1980s revealed the ability to directly visualize large biomolecular assemblies. In the early states, the cryo-EM suffered from "technical" drawbacks (specimen damages, low signal to noise ratio, and additional instabilities related to the microscope) limiting the reachable resolution at few nanometers and leading to poorly resolved structures compared to X-ray crystallography reaching atomic resolution.

Protein X-ray crystallography provides the atomic structure of a protein from recorded X-Ray diffraction patterns of 3D crystals that are converted into a 3D model of electron densities. The macromolecular assemblies are generally difficult to crystallize due to their large sizes and low stability. In contrast, in cryo-EM the sample is a suspension of proteins or macromolecular complexes quickly frozen in amorphous ice. Thus the biological specimens remain hydrated in a state close to its state in solution (Dubochet and McDowall, 1981; Dubochet *et al.*, 1988). The principle of Single Particle Analysis consists in acquisiting of thousands of particle images which are randomly oriented. The different spatial orientations of particles allow to calculate a 3D volume of non-periodic biological specimens (Frank, 1975).

The first EM 3D reconstruction was achieved by De Rosier and Klug (1968) with the T4 bacteriophage tail, establishing for the first time, the basis for determining 3D reconstruction from 2D EM images. In the early studies, the 3D reconstruction from EM projections was performed on crystalline ordered molecules (Crowther *et al.*, 1970; Unwin and Henderson, 1975). At that time, the highly symmetric assemblies (2D crystals, helical and icosahedral structures) provided a repetitive signal enhancing the signal to noise ratio therefore leading to 3D reconstruction at sub-nanometer resolution and even better as exemplified with the structure of bacteriorhodopsin at 3.5 Å (Henderson *et al.*, 1990). In contrast, low symmetry particles presented a low signal to noise ratio giving rise to a more limited resolution. Since 2014, the cryo-EM experiences a major breakthrough by obtaining the high-resolution structures due to technical improvements in microscopy technology, camera technology for data collection and computational image analysis. The technological improvements will further be discussed in the following chapter in the context of cryo-EM workflow and data collection.

Nowadays, the cryo-EM analysis allows studying a broad range in size of proteins and multi-protein complexes at near atomic resolution. For example, reachable resolutions are in a range of 1.8 to 4.5 Å, for dengue virus (3.6 Å, Kostyuchenko *et al.*, 2014), glutamate dehydrogenase (1.8 Å, Merk *et al.*, 2016), human p97 (2.3 Å, Banerjee *et al.*, 2016) and Darpin (3.1 Å, Liu *et al.*, 2018). The near atomic cryo-EM density maps present densities which correspond to α-helices and β-strands, and side chains that permit to build atomic models either using the crystal model as starting structure or to directly build a *de novo* atomic model (Yu *et al.*, 2008; Cong and Ludtke, 2010).

2. Cryo-EM grid preparation methods

The grid preparation represents a step that is crucial for the successful cryo-EM analysis. Despite some marginal evolutions, the method of sample preparation in cryo-EM remains largely unchanged from the genuine Dubochet's vitrification method (Dubochet *et al.*, 1988).

In cryo-EM the sample support is a metal grid usually coated by a carbon film having a defined hole pattern. The sample preparation consists in depositing few microliters of sample onto a hydrophilic EM grid before blotting the excess of solution with filter paper. The remained solution forms a thin layer in the hole pattern over the entire grid. Then, the grid is quickly plunge frozen into liquid ethane and stored in liquid nitrogen before cryoEM image acquisition.

The sample preparation could be performed by manual-blotting or automated double-side or one-side blotting of the EM grid in humidity and thermostated environment. However, during grid preparation the particles could denature, protein assemblies could break up and particles could even present a limited set of views by adopting preferential orientations relative to the thin vitreous ice layer and the air-water interface (Taylor and Glaeser, 2008). Indeed, the particles could be exposed to the air-water interface after grid blotting and before plunge freezing. Approximately 90% of particles are ending up at the air-water interface (Noble *et al.*, 2017).

Efforts are made to develop new sample preparation methods. One of them uses microfluidic devices (Dandey *et al.*, 2017), which allow depositing tens of picoliters of biological sample and may reduce the exposure time of the particles to the air-water interface for improving particle distribution. Other methods propose to use additional supports, such as functionalized lipid monolayer (Kelly et al., 2008) or amorphous carbon (Grassucci *et al.*, 2007). The presence of this latter induces significant background noise in the particle images limiting its use (Gao *et al.*, 2007). A recent alternative proposes the use of graphene oxide (GO) sheets which are almost transparent and enrich adsorbed particles within the holes of the grid (Bokori-Brown *et al.*, 2016; Palovcak *et al.*, 2018).

2.1. Dubochet's cryo-EM grid preparation method for single particle analysis of MexA-MexB-OprM complex

Several cryo-EM sample preparation methods were performed to determine the most adapted one to analyze the MexA-MexB-OprM complex by single particle cryo-EM. The sample preparation using Dubochet's method was first performed. Several cryo-EM grids (Lacey, Quantifoil or C-Flat) were tested to figure out which grid type was suitable for performing reproducible cryo-EM grids of the MexA-MexB-OprM system amenable to single particle analysis. The different grid types present either irregularly spaced holes for Lacey grids or regularly-spaced circular holes for the Quantifoil and C-Flat grids. The C-Flat grids differ from the two other grid types by their carbon film thickness. Indeed, lacey and Quantifoil grids have a plastic film support for the carbon deposit while the plastic part of C-Flat grids is removed to ensure proper grids with ultra-thin carbon film. The carbon film thickness of the grid directly impacts the ice thickness formed into the holes. The thicker the carbon, the ticker is the ice layer. However, the C-Flat grid also seems more fragile as the plastic film support is removed and consequently demands the preparation of several grids because in most cases only a portion of the grid is exploitable. Despite these drawbacks, the retained grid type was the C-Flat grid because it provided a reproducible thin continuous ice layer covering the grid squares (Figure 26 A). The Dubochet's method revealed that the sample showed high affinity with the carbon film. The thin vitreous ice layer contained no particle and the particles were found aggregated at the carbon edges of the holes (Figure 26 B).

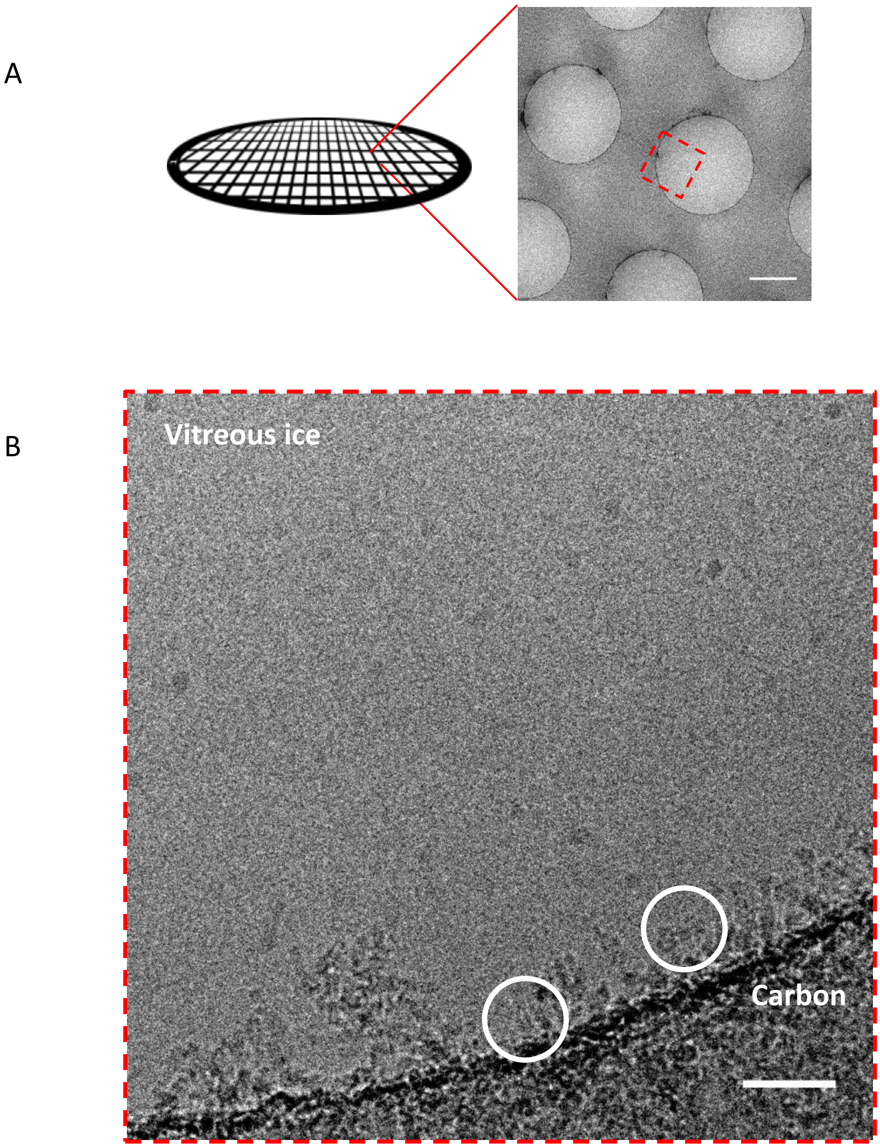

Figure 26- Cryo-EM sample of MexA-MexB-OprM complexes onto C-Flat carbon grid

The representation of schematic grid shows a focus onto one grid square presenting general ice aspect which is homogenous and continuous (A, scale bar 1µm). The sample distribution observed onto representative image shows particles onto carbon hole edges (B). In brief the grids were prepared as follows: the grids were glow discharged from both grid sides at 2 10^{-1} mbar and 2.2 mA. The grids were then mounted onto a EMGP plunge freezer (Leica), a 3 µl sample was deposited onto the grid for 30 seconds before blotting (Whatmann n°5 filter paper) and plunge freezing in liquid ethane.

Thus, the distribution of the particles within the ice layer needs to be improved for further image processing. A way to obtain a homogenous distribution of the particles is to provide a support on which the particles can adhere. The use of an extra thin layer of carbon deposited on the surface of the holey carbon film is rather well-known and is successfully used for macromolecules like ribosomes. I did not use this approach for two reasons. Since the complex is elongated, there is a high risk of producing preferential views (side and top views) that is not recommended for single particle analysis (if the particle distribution is not isotropic, the resolution of the 3D volume will be degraded). The second reason was to avoid the additional background originating from the carbon layer that could render more difficult the particle visualization and selection. When I started this work, there was no other method available. The graphene oxide method described below came up later. That is why I started to develop an original approach described in the next paragraph based on the well-know "lipid monolayer technique" (Lévy *et al.*, 1999; Dezi *et al.*, 2011; Simon *et al.*, 2013). The concept consists of the formation of lipid bilayer with Ni-NTA functionalized lipids to retain His-tagged protein sample on the grid surface.

2.1.1. Cryo-EM grid preparation method with lipid bilayer Ni-NTA functionalized support

The concept of lipid bilayer formation onto the cryo-EM grid consists in creating a thin lipid bilayer support containing functionalized lipids for a specific binding of proteins directly on the grid before plunge freezing. The functionalisation of the lipid bilayer offers a versatile tool for studying a broad range of proteins (Kelly et al., 2008). The technique is supposed to avoid particle adsorption onto carbon surface impairing possible complex disruption or protein structure alteration. The particles being retained by functionalized lipids remain far away from the air-water interface.

The demonstration of the lipid bilayer formation is achieved by a lipid film deposition on each side of the grid. The lipid films contain distinct fluorescent dyes with no spectral overlap (Figures 27 and 28). Thus, the chosen lipids comprise fluorescent lipids, dilution lipid and functionalized-lipids. The fluorescent lipids are egg-transphosphatidylated lipids from chicken. One of the lipid layer is composed of the green fluorescent lipids, PE-NBD (L-α-Phosphatidylethanolamine-N-(7-nitro-2-1,3-benzoxadiazol-4-yl) (ammonium salt)) (Figures 27, 29). For the second fluorescent layer, the red fluorescent lipid, PE-RB (L-α-Phosphatidylethanolamine-N-(lissamine rhodamine B sulfonyl) (ammonium salt)) is used (Figures 28, 30). Both lipids were supplied as powder at 1mg (Avanti Polar Lipids). They are aliquoted as stock solution at 1mg/ml in chloroform. The 1,2-dioleoyl-*sn*-glycero-3-phosphocholine (DOPC) lipids were supplied as powder at 1g (Avanti Polar Lipids) and aliquoted at 10mg/ml in chloroform. The functionalized-lipid 1,2-dioleoyl-*sn*-glycero-3-[(N-(5-amino-1-carboxypentyl)iminodiacetic acid)succinyl] nickel salt (18:1 DGS-NTA(Ni)) was supplied as powder at 25mg (Avanti Polar Lipids) (Figure 31).

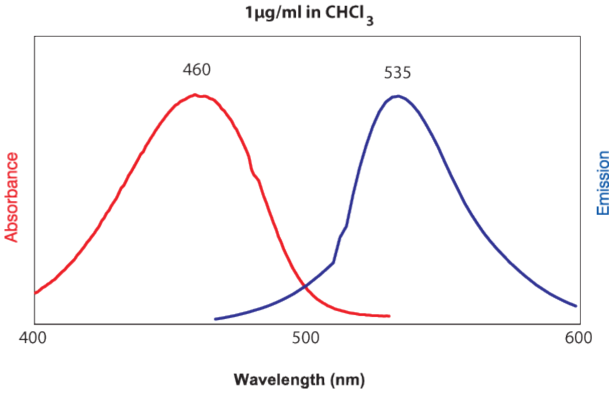

Figure 27- Fluorescent spectra of PE-NBD

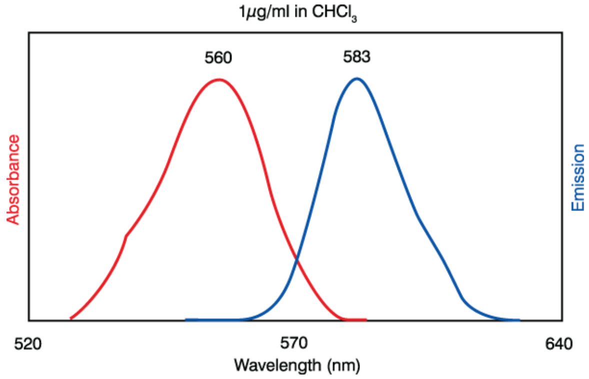

Figure 28- Fluorescent spectra of PE-RB

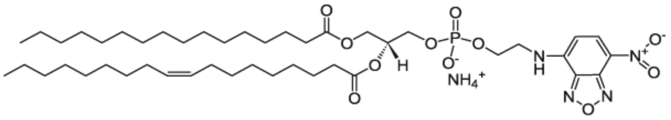

Figure 29- Chemical structure of PE-NBD

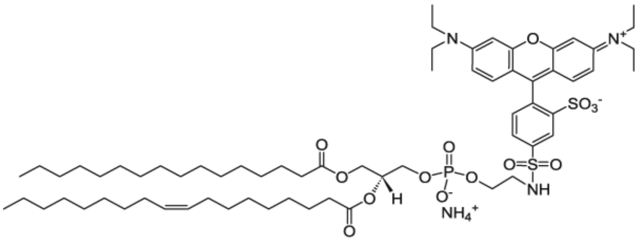

Figure 30- Chemical structure of PE-RB

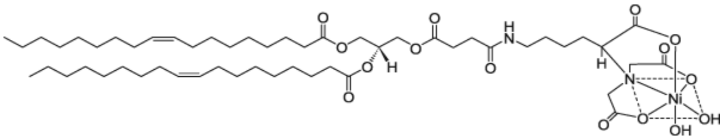

Figure 31- Chemical structure of DOGS-NTA(Ni)

For lipid bilayer formation with NTA(Ni)-lipid, two different lipid working solutions are prepared. The first lipid working solution is composed of DOPC 60%, PE-NBD 30% and DGS-NTA(Ni) 10% at 1mg/ml in chloroform/methanol (7/3, v/v). The second lipid working solution is composed of DOPC 80%, PE-RB 20% at 1mg/ml in chloroform/methanol (7/3, v/v).

The demonstration of lipid bilayer formation (Figure 32) consists in depositing 1µl of lipids-solvent solution with Hamilton syringe onto water (double-distillated water 18 MOhm.cm at 25°C, Milipore Système Direct-Q 3) filled Teflon wells. After overnight incubation the lipid film is transferred onto the cryo-EM grid using the grid side coated with the carbon film. The film transfer has to be as gentle as possible and the grid is brought parallel in contact with the lipid film before removing as slowly as possible. Then the grid is turned and the second lipid film is transferred onto the bare side of the cryo-EM grid.

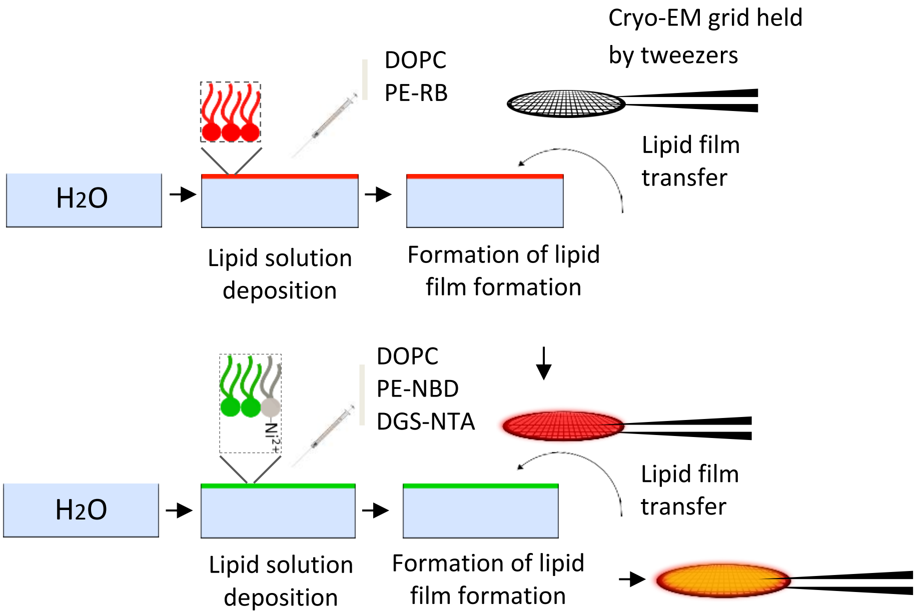

Figure 32- Workflow of lipid bilayer deposition onto cryo-EM grid

The schematic representation of the lipid bilayer functionalization cryo-EM grid preparation workflow illustrates stepwise by lipid film formation and succeeding film recuperation onto cryo-EM grid.

After lipid bilayer formation the grid is immediately mounted onto the cryo-plunge machine (EMGP from Leica) and the sample deposition is done on the opposite side of the carbon film before blotting and plunge freezing (Figure 33).

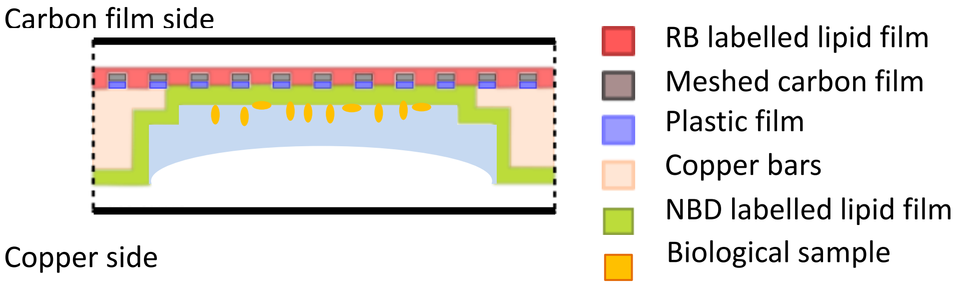

Figure 33- Illustration of a cross-section of a cryo-EM grid square with lipid bilayer formation and sample deposit

The schematic drawing of a cryo-EM grid square representing the red fluorescent lipid layer deposit onto carbon film and green fluorescence lipid layer deposit onto the opposite grid side. The sample is deposited onto the film side with the green fluorescent functionalized lipid monolayer. The particles bind to the functionalized lipid film far from the air-water interface. The grid is directly plunge frozen and stored in liquid nitrogen before cryo-EM observations.

The contribution of both lipid films in bilayer formation is checked in the Leica EM cryo-CLEM microscope (Leica DM6 FS). This fluorescent microscope allows mounting and observing a cryo-EM sample in a temperature regulated environment. This technique provides the proof of the contribution from both lipid films onto the cryo-EM grid. The deposits of the lipid films are distinguishable at 40x magnification (objective characteristics: ∞/0.17/D; HCX PL FLUOTAR; 40x/0.75; PH2) (Figure 34, A and B) and 100x magnification (objective characteristics: ∞/0.17/D; HCX PL FLUOTAR; 100x/1.30; PH3) (Figure 34, E and F). Not all the cryo-EM grid squares present the contribution of both lipid films, which is verified by merging the images of the two distinct colour channel red and green (Figure 34 C). However, the contribution of both lipid films is verified at 100x magnification, by observation of the distinct colour channel (Figure 34, E and F) and superposition of these channels (Figure 34 G). The images acquired in phase contrast mode seem to show continuous lipid film contribution with only little lipid film exceeds (Figure 34, D and H).

The image acquisition procedure consists in taking the images subsequently in red, green channel and phase contrast mode. The fluorescent filter cubes are the N3 (fluorescent spectra at excitation 595 nm/emission 613 nm) and the L5 (fluorescent spectra at excitation 488 nm/emission 508 nm). The acquisition is performed with: 300 ms and 200 ms exposition time for RB fluorescence at respectively 40x and 100x magnification and 2000 ms exposition time for NBD fluorescence at 40x and 100x magnification. The exposure time of in phase contrast mode is about 30ms.

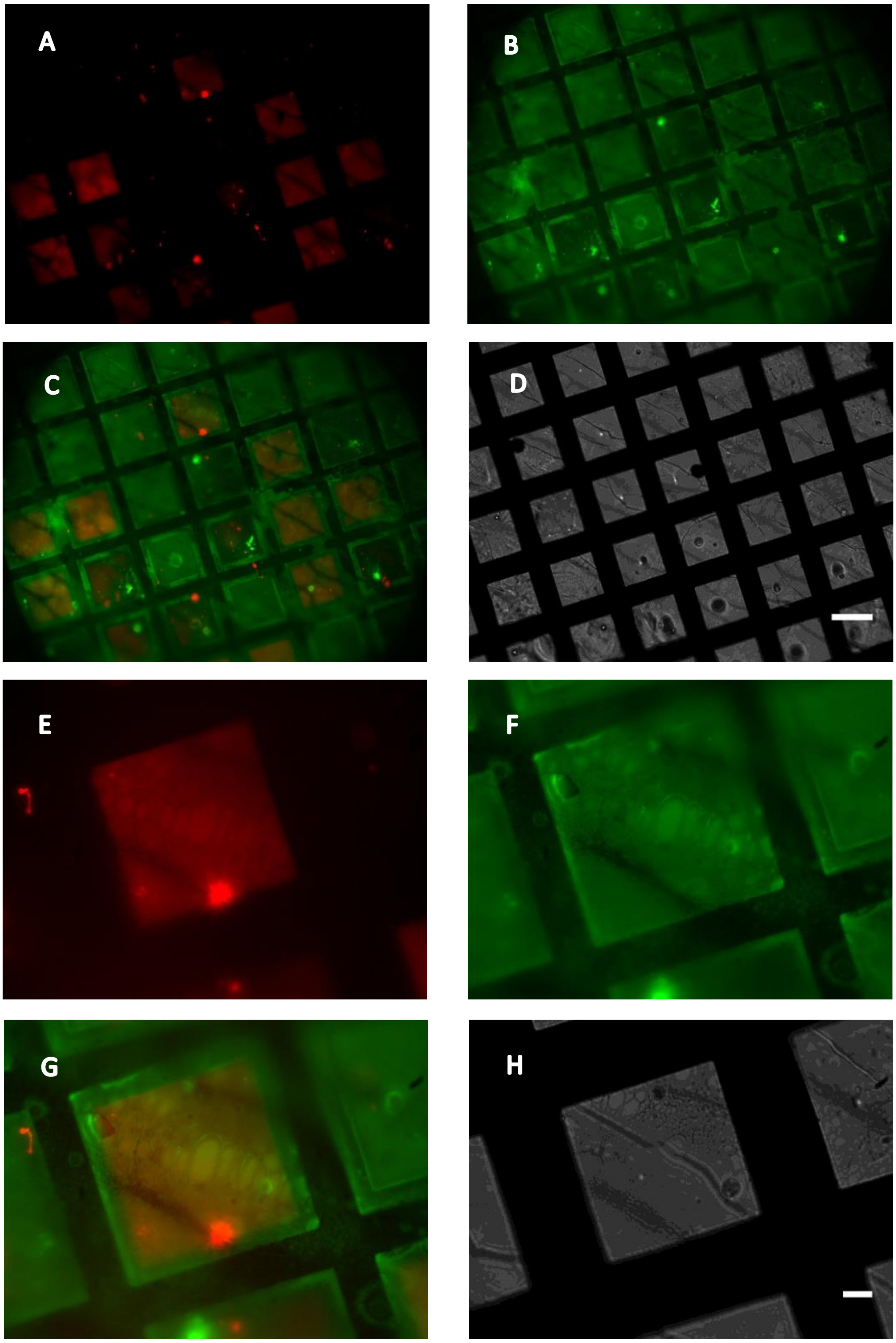

Figure 34- Illustration of lipid bilayer deposition with sample deposit onto Cryo-EM grid

Fluorescent and phase contrast images of functionalized lipid bilayer cryo-EM grid at 40x (A-D, Scale bar 50 µm) and 100x magnification (E-H, 10 µm). The lipid layer deposits seem continuous with a homogenous fluorescence from both fluorophores and has a transparent aspect in phase contrast.

The checked grids are further analysed in cryo-EM with F20 200keV (FEI) microscope, at 5,000x and 29,000x magnification and compared with the control, the same biological sample prepared onto glow discharged cryo-EM grids without support (Figure 35 A). The control condition shows thin vitreous ice (Figure 35 A and B) with few remaining particles (Figure 35 B).

The functionalized lipid bilayer cryo-EM grid shows lipid contribution as continuous layer and little lipid exceeds which form strands or liposomes over almost three quarters of the grid (Figure 35 C). The sample MexB in Nanodisc (MexB-ND) is used as test sample at 0.2 mg/ml. The particles are clearly visualized on lipid film support and appear monodisperse distributed in vitreous ice (Figure 35 D). Despite the ice thickness that is certainly too important for performing high resolution single particle cryo-EM analysis, a nice distribution of the particles within the ice is observed, indicating that this approach may be an interesting approach for a better control of the particle distribution. It remains that further optimizations are needed to reduce the amount of lipid deposition and to optimize sample blotting for obtaining the sample embedded in a thin ice suitable for high resolution analysis.

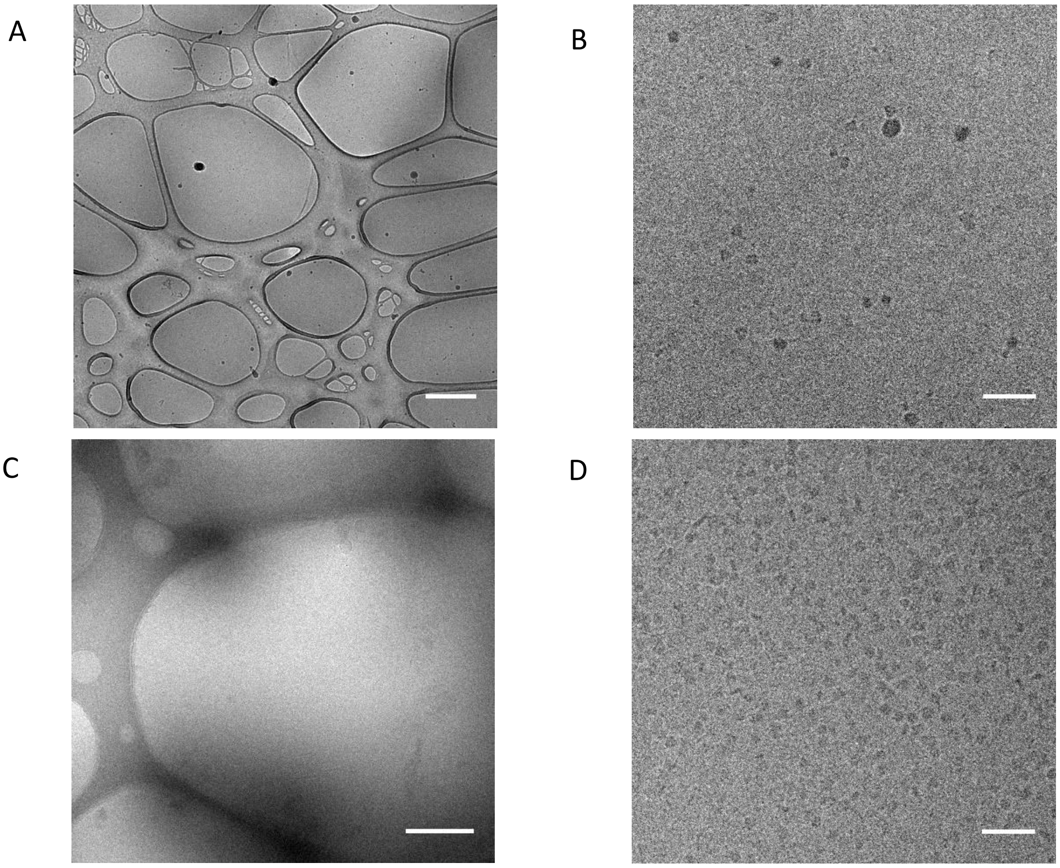

Figure 35- Cryo-EM analysis of functionalized lipid bilayer with MexB-ND as test sample

Compared to the Dubochet's sample preparation method, the cryo-EM sample preparation using lipid bilayer deposition improves MexB-ND particles concentration on cryo-EM grid. The images illustrates the control condition without sample support (A, Scale bar 500 nm and B, Scale bar 50 nm) in comparison to the functionalized lipid bilayer cryo-EM grid (C, Scale bar 500 nm and D, Scale bar 50 nm).

I did not pursue this approach because in the meantime, an easy and promising method using the deposition of thin layers of graphene oxide sheets has been published. I have adapted this method for the tripartite complex as described in the next paragraph.

2.1.2. Cryo-EM grid preparation methods using a coating with graphene oxide sheets

A coating of the EM grid with graphene oxide (GO) sheets described recently (Bokori-Brown *et al.*, 2016) is implemented and adapted, in order to perform high-resolution single particle cryo-EM studies of macromolecular complexes. This method is chosen due to the physical properties of the GO which is nearly electron transparent, hydrophilic and presents a good electron conductivity.

To take advantage of the method, the C-flat holey carbon-coated cryo-EM grids (C-Flat 2/1 -2C-50, Protoships) are chosen for their ultra-flatness providing ultra-flat and uniform ice surface and thickness as well as stability for GO sheet deposits. The regular grid pattern facilitates image acquisition in an automated manner to record a large dataset. The carbon side of the grids is treated by plasmon through electric glow discharge (0.29 mbar, 3mA for 40s, Cordouan) before being covered with GO sheets. The graphene oxide solution (2mg/ml, dispersion in H_2O, Sigma-Aldrich) is resuspended into water (18 MOhm.cm at 25°C, Milipore Système Direct-Q 3) in order to obtain a concentration allowing a homogeneous grid coverage by the GO sheets. The grid is taken into anti-capillary tongs (carbon side on top). The suspension, a 4µl drop, is deposited on the by plasmon treated carbon grid side for 1 minute. The grid is cleaned and hydrophilized in order to make the monolayers of GO stick onto the carbon. The drop is blotted onto cellulose filter paper (Grade 5, Whatman), with the drop oriented upside down. The grid is air dried over 5 min before storage overnight. The grid is UV treated during 1min at the copper side of the grid. Then, the grid is ready to use for sample deposit. The sample is incubated onto the UV-treated side during 1min under hygrometry and thermostated conditions before blotting and plunge freezing.

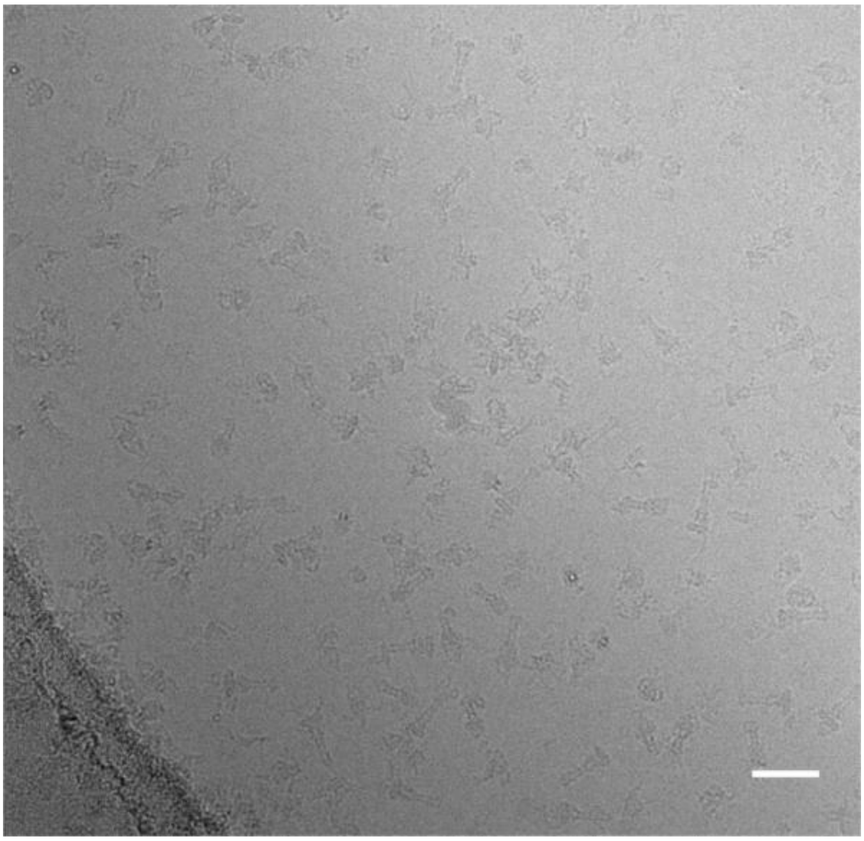

Figure 36- CryoEM grid of MexA-MexB-OprM efflux system

The sample of Nanodisc stabilized MexA-MexB-OprM efflux system deposited onto graphene oxide covered C-Flat grids present thin vitreous ice layer with homogeneous distributed particles of multiple orientations. The shown micrograph comes from the data collection performed on a Titan Krios (scale bar 50nm).

Chapter 4 – Data collection

In chapter 4, the data collections for single particle cryo-EM analysis are presented and critical criteria to access high resolution data will be discussed.

1. Introduction to single particle cryo-EM image analysis

Single-particle cryo-EM does not need an absolute sample homogeneity for 3D reconstruction. The implemented image analysis software is able to deal with a sample heterogeneity which could come from conformational configuration and compositional composition. The direct electron detection cameras allow acquiring movies composed of frames with high signal to noise ratio, and frame alignment correcting for stage drift improves the final image quality.

During my thesis, I use Eman2 and RELION2.1 for image processing. The image analysis starts with particle-picking which allows obtaining a large particle dataset. The 2D projection of the particles could present distinct orientation or compositional heterogeneity on which the particle images have to be sorted into 2D classes. The constituted classes contain homogeneous particles subsets. The maximum likelihood-based method is chosen for classification and refinement (Scheres *et al.*, 2007). The algorithms (Sigworth, 1998; Sigworth *et al.*, 2010) are implemented into user-friendly software packages for RELION2.1 (Scheres, 2010, 2012). The 2D projections are then sorted into different 3D classes. The 3D classification gives access to 3D reconstructions that may exhibit several structural conformations. Each 3D reconstruction or a combination of several 3D reconstructions can be further refined to determine a high-resolution structure.

2. Cryo-EM workflow

The simplified workflow (Figure 37) summarizes the different steps from the sample preparation until the calculation of the 3D volume and the building of near-atomic model of MexA-MexB-OprM efflux pumps.

After improving the biochemical sample preparation and optimizing the cryo-EM sample preparation, the next step consists in performing data acquisition and determining the most appropriated parameters in data collection to access high resolution cryo-EM data. For this purpose, I performed several data collections on different microscopes. The data collections were successively recorded using a Talos Arctica (ThermoFisher FEI), Tecnai F30 Polara (FEI), and Titan Krios (ThermoFisher FEI). The different data collections and associated results from image analysis will be discussed in the next paragraphs.

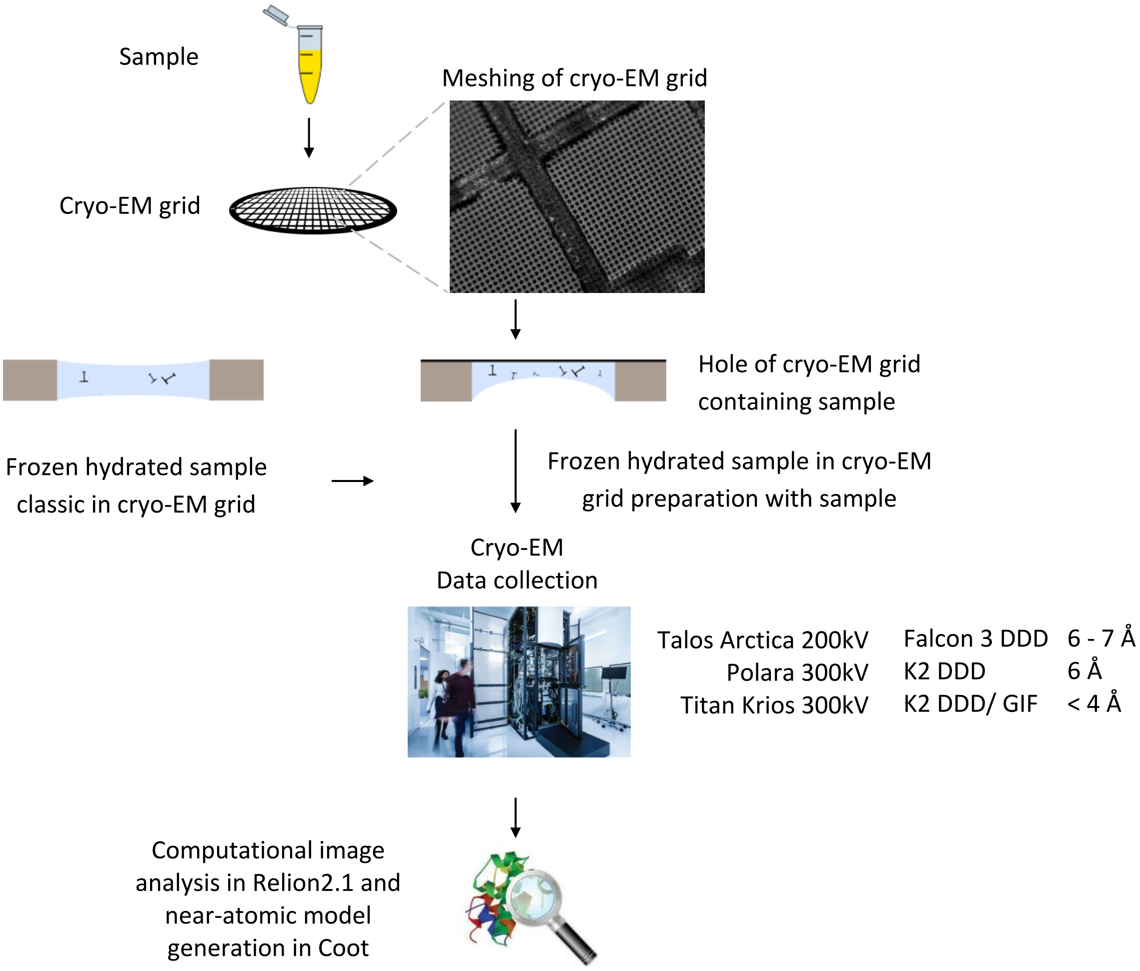

Figure 37- Cryo-EM workflow from the sample preparation to the structure determination

The single particle cryo-EM analysis is performed in four main steps which consist in preparing biological sample used for cryo-EM sample preparation followed by the data collection and computational image analysis.

3. Analysis of the cryo-EM data collection and image processing

3.1. Tecnai F30 Polara : a collection of a small set of images

A small set of images is collected first to assess whether the particles adopt a random orientation and distribution in thin vitreous ice with the use of the graphene oxide film. The data collection is performed on the 300kV Tecnai F30 Polara (FEI) at IBS Grenoble.

Micrographs (183) are manually recorded with dose fractionated images on a K2 Summit direct detector (GATAN) in a counting mode with a pixel size of 1.94 Å. Each micrograph is recorded as 40 movie frames with dose of 1 e^{-} Å^{-2}/frame with defocus values ranging from -1 to -3 µm, a spot size of 6, a condenser aperture of 50 µm, and an objective aperture of 100µm.

As shown in the micrograph, the particles adopt random distribution in thin vitreous ice (Figure 38 A). The particles retained onto the graphene oxide film (seen by folds) are numerous and allow performing single particle analysis. As the image set is small, the data are processed with Eman2. 1261 particles are used to calculate 2D projections (Figure 38 B) and a 3D reconstruction at approximate 25 Å resolution (Figure 38 C). The low resolution of the 3D reconstruction is attributed to the small data set. Interestingly, despite the low data set, features as the Nanodisc are visible. This promising result encourages me to collect a larger data set.

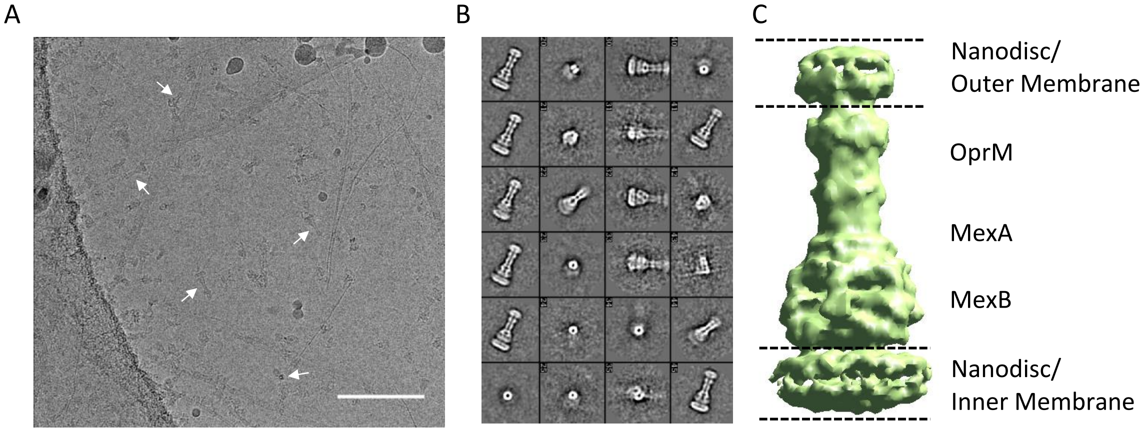

Tripartite complex on graphene oxide support in cryo-EM, suitable for low concentration samples

2D projections of the MexA-MexB-OprM with multiple orientations

3D reconstruction of the tripartite complex at 25 Å resolution

Figure 38 - Image analysis of the first cryo-EM data set from Polara

The illustration shows typical micrograph (Scale bar 100nm) from MexA-MexB-OprM sample deposited onto graphene oxide coated C-Flat grid (A) from which particles were selected to calculate several 2D projections (B) used in 3D reconstruction (C).

3.2. Talos Arctica: data collection and image processing

Taking advantage of the newly installed Arctica at the IECB facility in Bordeaux, I performed an automated data collection using EPU (FEI) on Talos Arctica (ThermoFisher FEI) 200keV, with dose fractionated images recorded on a Falcon 3 EC direct electron detector (ThermoFisher FEI) in a linear mode with a pixel size of 1.597 Å. A data set of 1404 micrographs was collected in a 48 hours session. Each micrograph was collected as 20 movie frames with a total dose of about 20 e^{-} $Å^{-2}$. Images were recorded over a defocus values ranging from -1 to -3 µm, a spot size of 6, a condenser aperture of 70 µm, and an objective aperture of 100µm.

The processed data provides 2D projections presenting multiple orientations with few intermediate views (Figure 39 A). The reconstructed 3D volume is calculated at 6 Å resolution with local resolution until 5 Å (Figure 39 B). In order to understand the limitation in resolution, the used micrographs for 3D reconstruction reveal that the majority is limited at 6 Å resolution (Figure 39 C). Low density surfaces reveal the different proteins such as the six MexA and the α-helices of OprM and MexA (Figure 39 D). The resolution limitation may have several sources. First the microscope Arctica was recently installed when I recorded the data and it is possible that a finer tuning is still required to get a better resolution with our samples. Second, the fact that the microscope operates at 200kV may represent a limitation for imaging our 30 nm samples because it requires a thick ice layer producing noisier images (reducing the signal to noise ratio) and therefore lead to a global low resolution structure. To overcome such drawbacks, I decided to record a larger set of images on a 300 kV microscope.

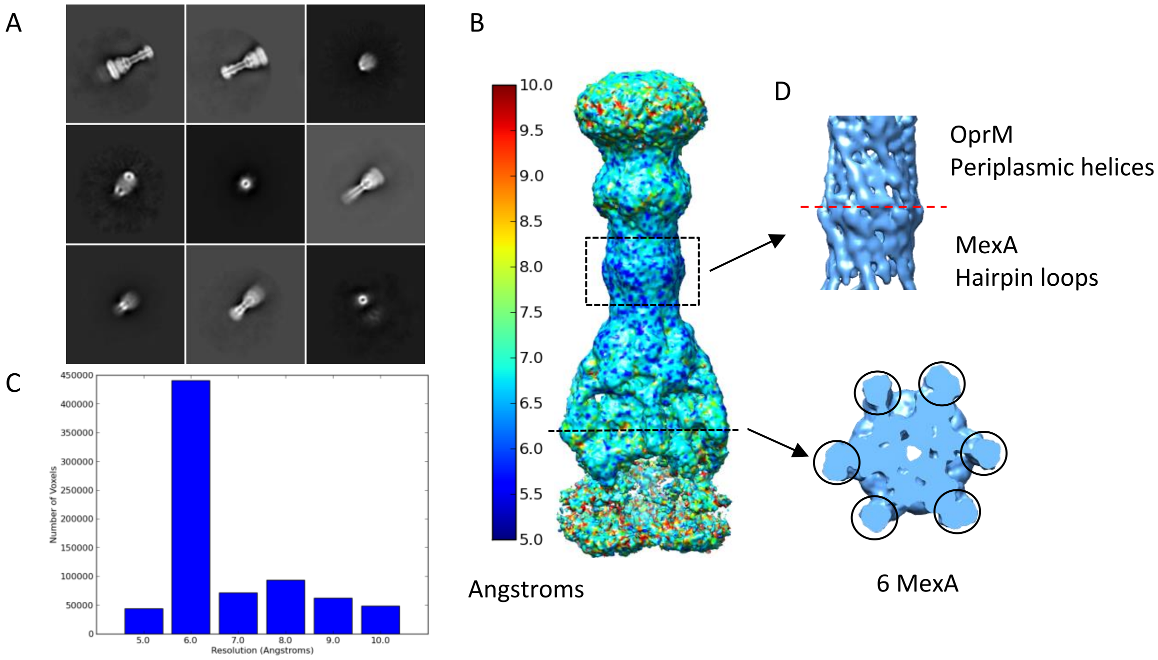

Figure 39- Image analysis of the cryo-EM data from Talos Arctica

The illustration presents 2D projections (A) which are used for 3D reconstruction of MexA-MexB-OprM with a global resolution of 6 Å (B). The global resolution could be attributed to the intrinsic resolution of the micrographs, reported by the histogram with 6 Å resolution of major voxels composing the 3D reconstruction (C). The structural features are distinguishable regarding OprM/MexA helices and the six MexA descending to the Nanodisc (D).

3.3. Tecnai F30 Polara : data collection and image processing

The second data collection on Tecnai F30 Polara (FEI) is then performed in automated fashion (EPU software, FEI) with dose fractionated images recorded on a K2 Summit direct detector (GATAN) in a counting mode with a pixel size of 1.21 Å. A data set of 2101 micrographs is collected in a 72 hours session. Each micrograph is collected as 40 movie frames for 7 s with a dose rate of 6 e^{-} $Å^{-2}$ s^{-1}. The total dose is about 42 e^{-} $Å^{-2}$. Images are recorded over a defocus values ranging from -1.3 to -3.1 µm, a spot size of 6, a condenser aperture of 100 µm, and an objective aperture of 100µm.

The data are processed in Relion2.1. The 3D reconstruction calculated with 18738 particles has a final 6.9 Å resolution. The MexA-MexB-OprM is profiling detailed features with Nanodiscs from each end of the efflux pump, the six MexA could be easily distinguished (Figure 40 B left) and α-helices of OprM and MexA are unveiled when increasing the surface threshold (Figure 40 right).

Clearly the resolution is not sufficient to correctly describe the whole structure. It is likely that the 3D reconstruction is limited in resolution because of the low number of particles. Collecting additional particles on the Polara could have been a way to improve the resolution. However, in the meantime I got the opportunity to get access to a Krios microscope that is considered as a reference to collect high resolution data.

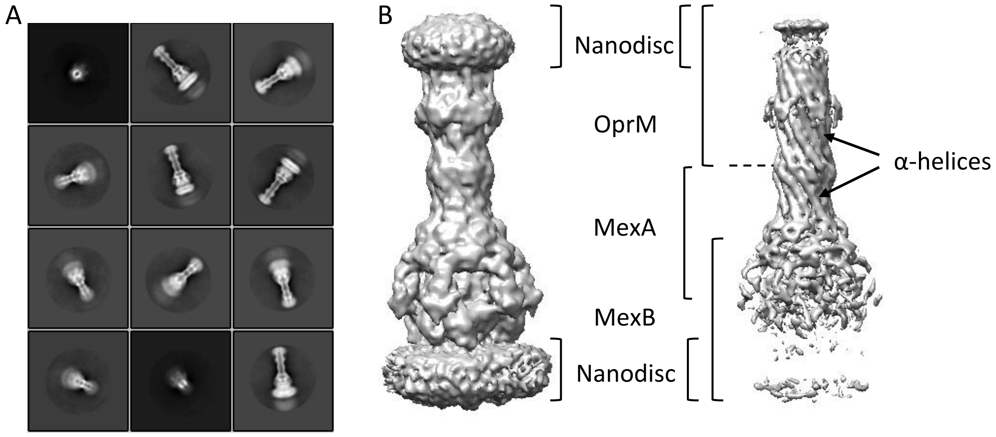

Figure 40- Image analysis of the second cryo-EM dataset from Polara

The illustration presents 2D projections (A) which were used for 3D reconstruction of MexA-MexB-OprM with different surface density representation (B).

3.4. Titan Krios: data collection and image processing

The data collection is performed on Titan Krios at the European Synchrotron Radiation Facility (ESRF) of Grenoble, France. Electron microscopy images are recorded on a

FEI Titan Krios electron microscope at 300keV equipped with a post-column GIF Quantum energy filter (20 eV) (GATAN). Dose fractionated images are recorded on a K2 Summit direct detector (GATAN) in a counting mode with a pixel size of 1.36 Å. A data set of 3358 micrographs is collected over a 72 h session. Each micrograph is collected as 40 movie frames for 7 s with a dose rate of 6 e^{-} $Å^{-2}$ s^{-1}. The total dose is about 42 e^{-} $Å^{-2}$. Images are recorded using the automated acquisition program EPU (FEI) with defocus values ranging from -1 to -2.4 µm, a spot size of 6, a condenser aperture of 50 µm, and an objective aperture of 100µm.

This last data collection allows determining a 3D reconstruction at less than 4 Å resolution. The image processing and results will be discussed in the chapter 5.

4. Discussion of cryo-EM data collection criteria for high resolution 3D reconstruction

After performing data collections and processing the different data sets, it appears that different criteria in data collection are mandatory to collect high quality micrographs.

The automated compared to manual data collection presents several advantages. The automated data collection is less time demanding because, once calibrated, it can run over days without assistance. The data set is calibrated considering focus, image drift and defocus range producing a homogenous set of images that is required for image processing.

The cameras and their evolving technology benefit to high quality images. Thus with the novel detector technology, the incoming electrons are not anymore amplified (as for charged-coupled device (CCD)) but directly detected and attributed to a specific pixel (direct electron detection device (DDD) which make the data collection faster. The DDD cameras are more sensitive and the collected images have a better signal to noise ratio. The high frame rate of DDD cameras allows performing dose fractionated acquisition enabling the movie frame correction for stage- or beam-induced motion, which significantly improves image quality. The data acquisition in counting mode needs to be optimized by dose rate on the camera. The typical dose rate is of 10 e^{-} $pixel^{-1}$ s^{-1}. A lower dose rate can improve detective quantum efficiency (DQE), implicating longer exposure time to accumulate the same total dose and larger movies, which leads to larger file sizes and data storage issues.

The use of energy filter seems to be favourable to the last data collection on the Krios. It enables subtracting inelastic scattering electrons during image acquisition which decreases background contribution and improves the signal to noise ratio. The particles could be easily seen at low defocus and thus were included in the image processing. In retrospective, the indispensable criteria of data collection which are limiting the 3D reconstruction are the acquisition of large particle data set and the use of low defocus images that contain high resolution structural information.

Chapter 5 – Single particle cryo-EM analysis

In this chapter, image analysis and structural insights of the 3D reconstruction of the tripartite MexA-MexB-OprM of *Pseudomonas aeruginosa* will be presented.

1. Cryo-EM image analysis of the tripartite MexA-MexB-OprM

All movie frames are corrected for gain reference, and aligned using Motioncorr2 (Li *et al.*, 2013). Contrast transfer function (CTF) parameters are estimated using Gctf (Zhang, 2016). Further image processing is performed with RELION2.1 on “good quality” micrographs as the one presented below (Figure 41).

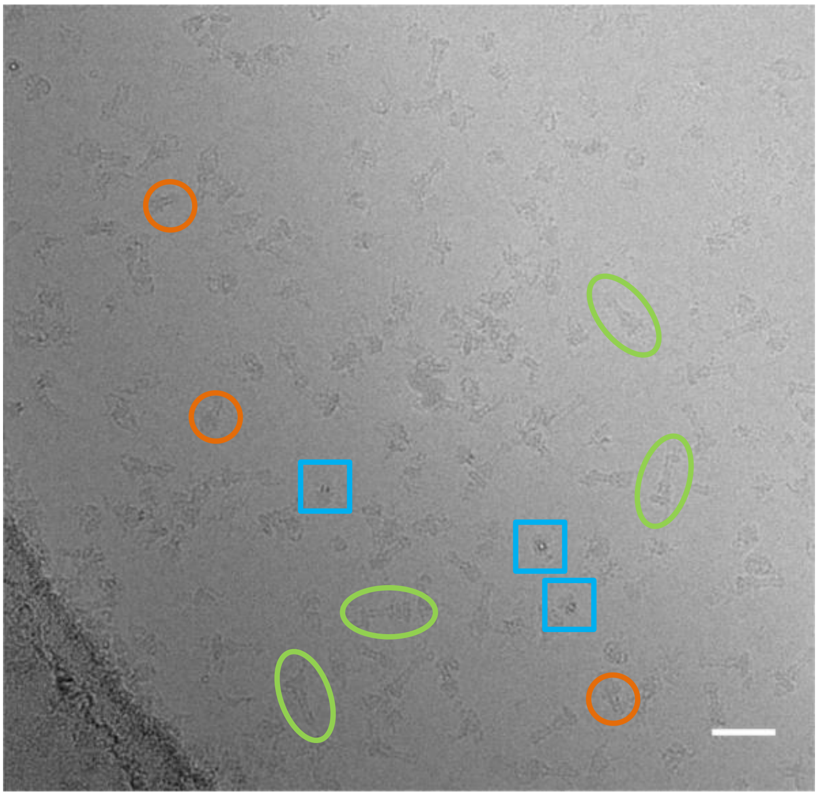

Figure 41- Representative cryo-EM micrograph of MexA-MexB-OprM efflux system

The cryo-EM micrograph of MexA-MexB-OprM efflux system recorded on a Titan Krios shows a thin vitreous ice layer with homogeneous distributed particles having multiple orientations with side views (green) corresponding to elongated structures and top views exhibiting circular shapes (blue) and intermediate views (orange) (scale bar 50nm).

Initial particle picking consists of a manual-picking of 1041 particles to calculate 2D references. These 2D templates are low-pass filtered to 20 Å and used for automated picking of all micrographs. A total of 364,914 particles from 3068 micrographs are picked, binned by 4 and extracted with a box of 128 pixels. Several steps of 2D classifications are performed to remove defective particles and lead to a subset of 96,755 particles (Figure 42).

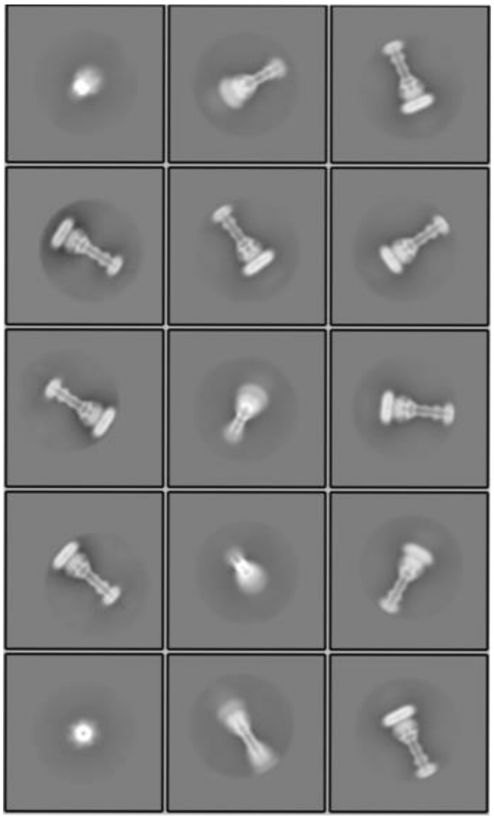

Figure 42- Selected 2D classes from classification of 96755 MexA-MexB-OprM particles

The presented 2D classes are a selection from the averaged 2D projections. Different orientations could be discriminated starting with the first class of the last row which correspond to a top view, with the first class of the first row, the second class from the first, third, fourth and fifth row correspond to intermediate views. The remaining classes are side views.

An initial model is calculated from a particle subset of the 2D classes and low-pass-filtered to 60 Å limiting reference bias during 3D classification (Figure 43).

The initial model is used to perform a 3D classification in 10 classes on the set of 96755 particles. The 10 volumes show similar features except the 6.1% class which is removed because of its distorted shape. The new particle set comprising 90,853 particles is submitted to a 3D auto-refinement process with no symmetry imposed and yield to a 3D reconstruction at 6.9 Å for particles binned by 2. The set of unbinned particles is then submitted to particle polishing (correcting beam-induced motion and radiation-damage weighting) (Li *et al.*, 2013). The 3D refinement and post-processing steps yield to a reconstruction of the MexA-MexB-OprM complex at 3.5 Å overall resolution with C1 symmetry imposed. This density map also called *first reference structure* is considered as the reference map for further image processing.

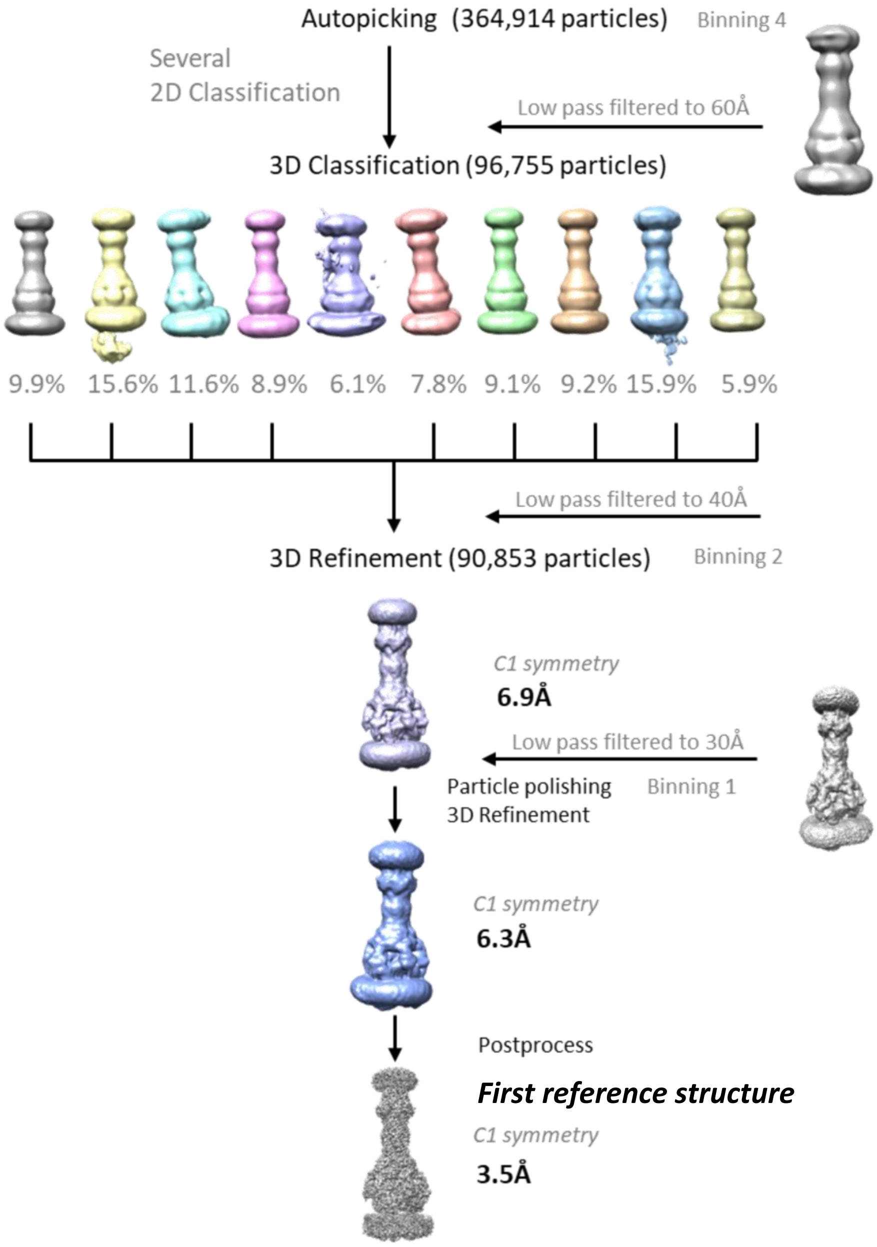

Figure 43- Image processing workflow from particle picking to the first refined 3D reconstruction

The workflow illustrates the stepwise procedure of image analysis starting from autopicking which consists in selecting all the particles on the micrographs. Next, several steps of 2D classification and 3D classification are performed aiming at particle sorting “good” from “bad” particles. The steps of 3D refinement allow improving particle alignment for the 3D reconstruction. The step of particle polishing is performed to correct locally the drift and the signal to noise ratio of each particle. A new corrected particle dataset is further used to calculate a volume at 6.3 Å resolution using 3D refinement and further improved at 3.5 Å resolution by a postprocessing step (knowing that the pixel size is 1.36 Å).

1.1. 3D reconstruction of tripartite MexA-MexB-OprM with a focus on OprM

A visual inspection of the first reference structure shows a trimeric organisation of MexB, a hexamer of MexA and OprM. On OprM part, the reconstruction exhibits six segments anchored into lipid Nanodisc suggesting an apparent six-fold symmetry for OprM (Figure 44). Providing that OprM is a trimer, the 3D structure of OprM is incorrect, probably because particles have not been sorted out properly.

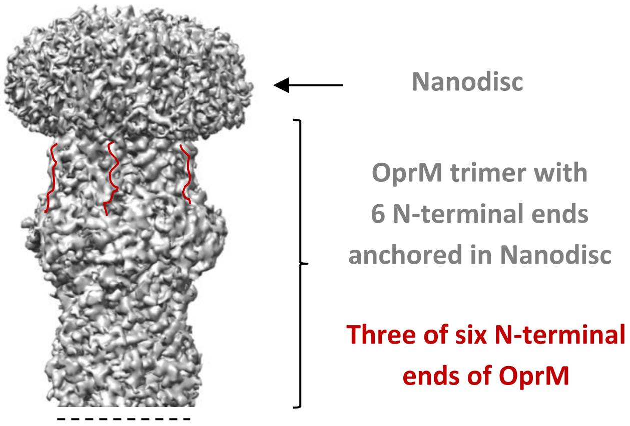

Figure 44- Visual inspection of OprM-ND in the *first reference structure*

OprM enshrined into Nanodisc exhibit six N-terminal ends highlighted with red revealing an incoherence with the trimeric structure of OprM.

The sorting out of particles is exclusively focused on the OprM part by using a specific operation named “masked 3D classification without alignment” (Figure 45). A mask is generated from the *first reference structure* using the volume erase function in Chimera (Mask #1). The particles are sorted out in four classes representing 40.8%, 47.5%, 10.5% and 1.2% of the total set of particles.

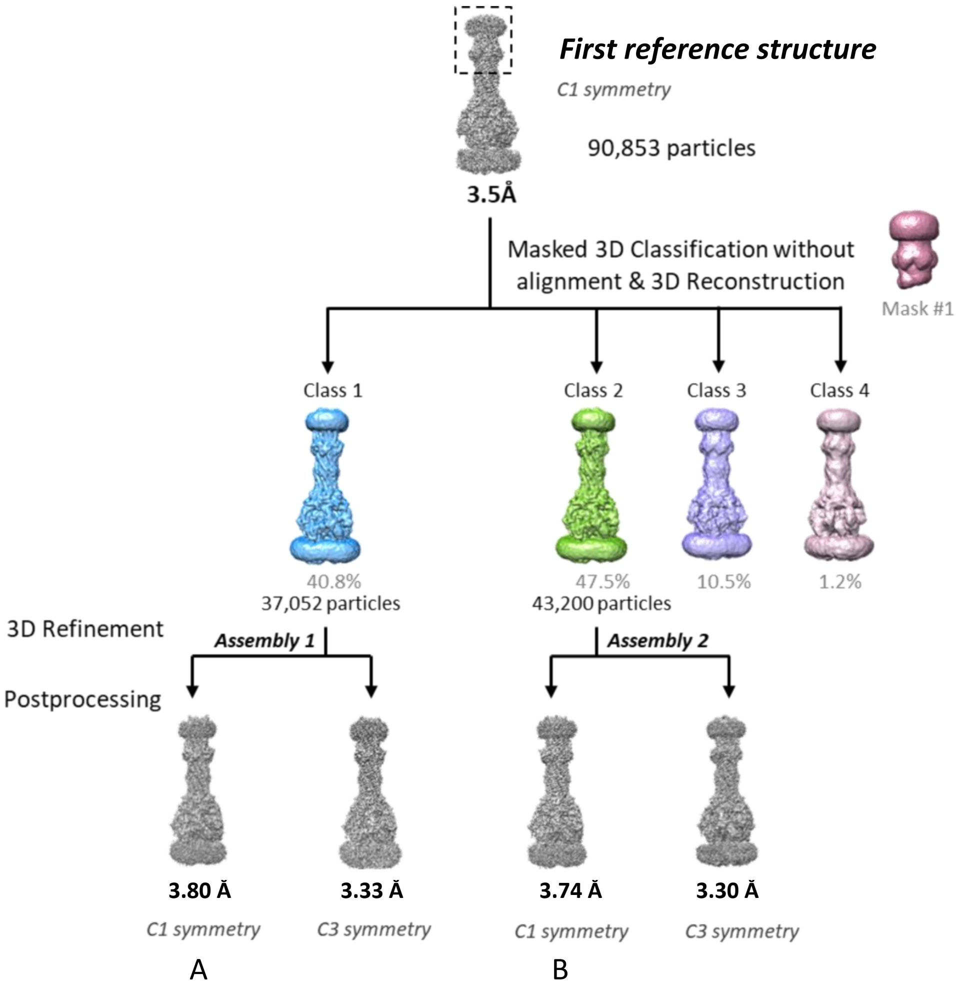

Figure 45- 3D reconstruction of two assemblies of MexA-MexB-OprM pump

The particle sorting in 3D classification with a focus on the OprM allows reconstructing two MexA-MexB-OprM assemblies containing 37,052 and 43,200 particles at 3.8 Å (A) and 3.74 Å (B) respectively.

Two main 3D classes, further processed by 3D refinement, reveal two different assemblies named Assembly 1 and Assembly 2 at 3.8 Å (Figure 45 A) and 3.74 Å resolution (Figure 45 B) without imposed symmetry. The resolution is estimated using the Fourier shells correlation coefficient with a cutoff at 0.143 (Figure 46 C and F). Inspection of the Euler angle distribution (Figure 46 B and E) shows an overall coverage of the reconstruction sphere which indicates that there is not induced bias in the reconstruction. The local resolution calculated with ResMap (Swint-Kruse and Brown, 2005) on the overall structure indicates that the protein partners of the efflux pump are resolved in the resolution range of 3.5-5.5 Å (Figure 46 A and D). The best resolved structural features correspond to three components, OprM, MexA, MexB while the two Nanodiscs, including the density of MSP proteins, are poorly resolved. This is likely due to a variable size.

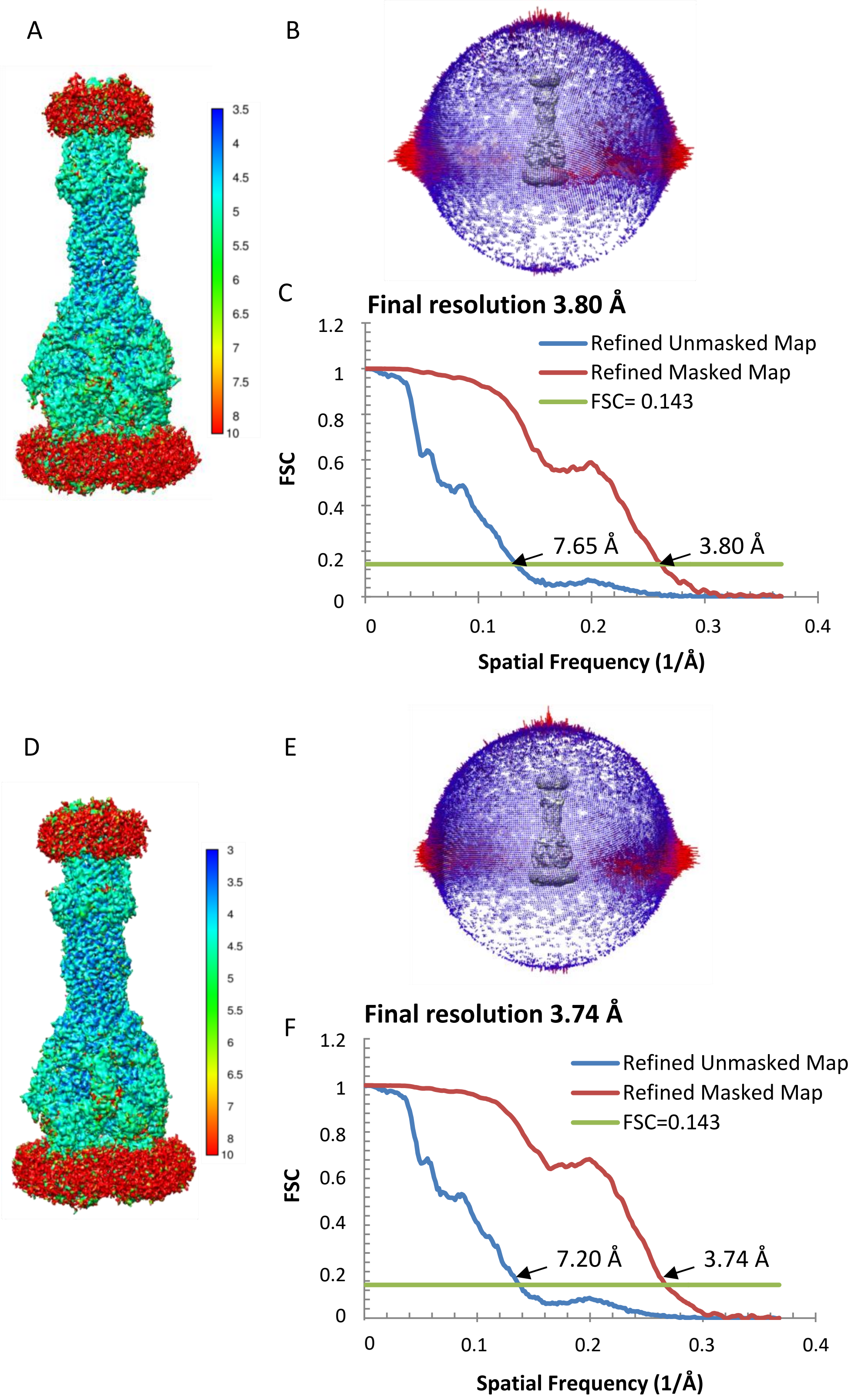

Figure 46- Resmap representations of the two assemblies of MexA-MexB-OprM pump

Local resolution determined by ResMaps of the density maps of the assembly 1 (A) at a global resolution of 3.8 Å and the assembly 2 (D) at a global resolution of 3.74 Å. The particle distribution over 360° is represented by the Euler angle distribution map (B and E). The resolution of the assemblies (unmasked and masked refined density maps) is estimated by the Fourier Shell Correlation (FSC) with a cutoff at 0.143 (C and E).

The two efflux systems are characterized by their difference in OprM positioning. Actually, the OprM of the Assembly 2 is rotated by 60° compared to the Assembly 1 with respect to the MexB (Figure 47).

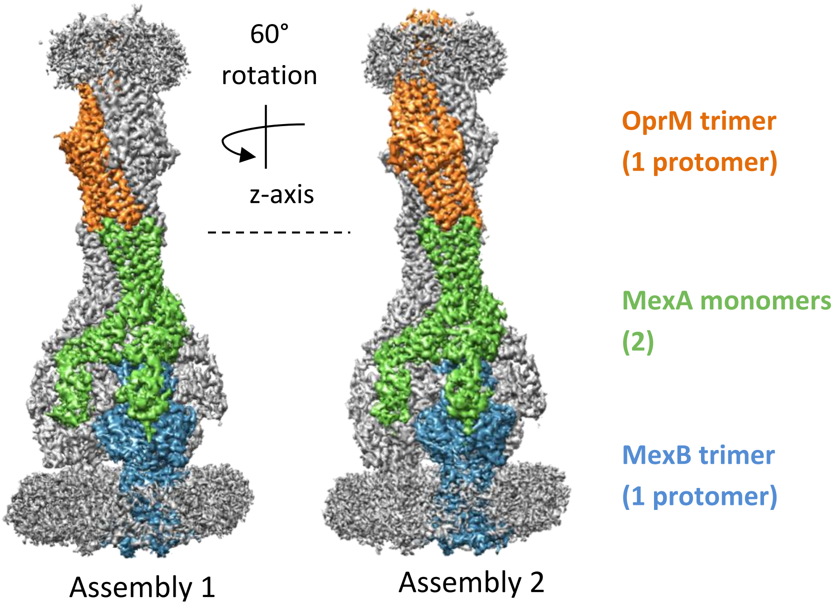

Figure 47- OprM position with respect to MexB in Assembly 1 and Assembly 2

3D reconstructions of Assembly 1 and Assembly 2 are segmented to reveal the three partners of the efflux system. OprM protomer is coloured in orange, two MexA monomers in green and MexB protomer in blue. OprM of the Assembly 2 is rotated by 60° compared to the Assembly 1 with respect to the MexB.

1.2. 3D reconstruction of tripartite MexA-MexB-OprM with C3 imposed symmetry

Considering the protein structures and their assembling in tripartite efflux system, a strategy of imposing C3 symmetry will enhance the structural features of the trimeric OprM and the 6 MexA monomers, and improve structural details of OprM-MexA interaction. However, MexB being described as an asymmetric trimer, the C3 symmetry will symmetrize also MexB. Its asymmetry will then be lost.

The Assembly 1 and Assembly 2 are determined with imposed C3 symmetry at 3.33 Å and 3.30 Å resolution respectively (Figure 48). Resmap representations show a homogeneous resolution of 3 to 4 Å resolution for the whole structure except for the nanodiscs.

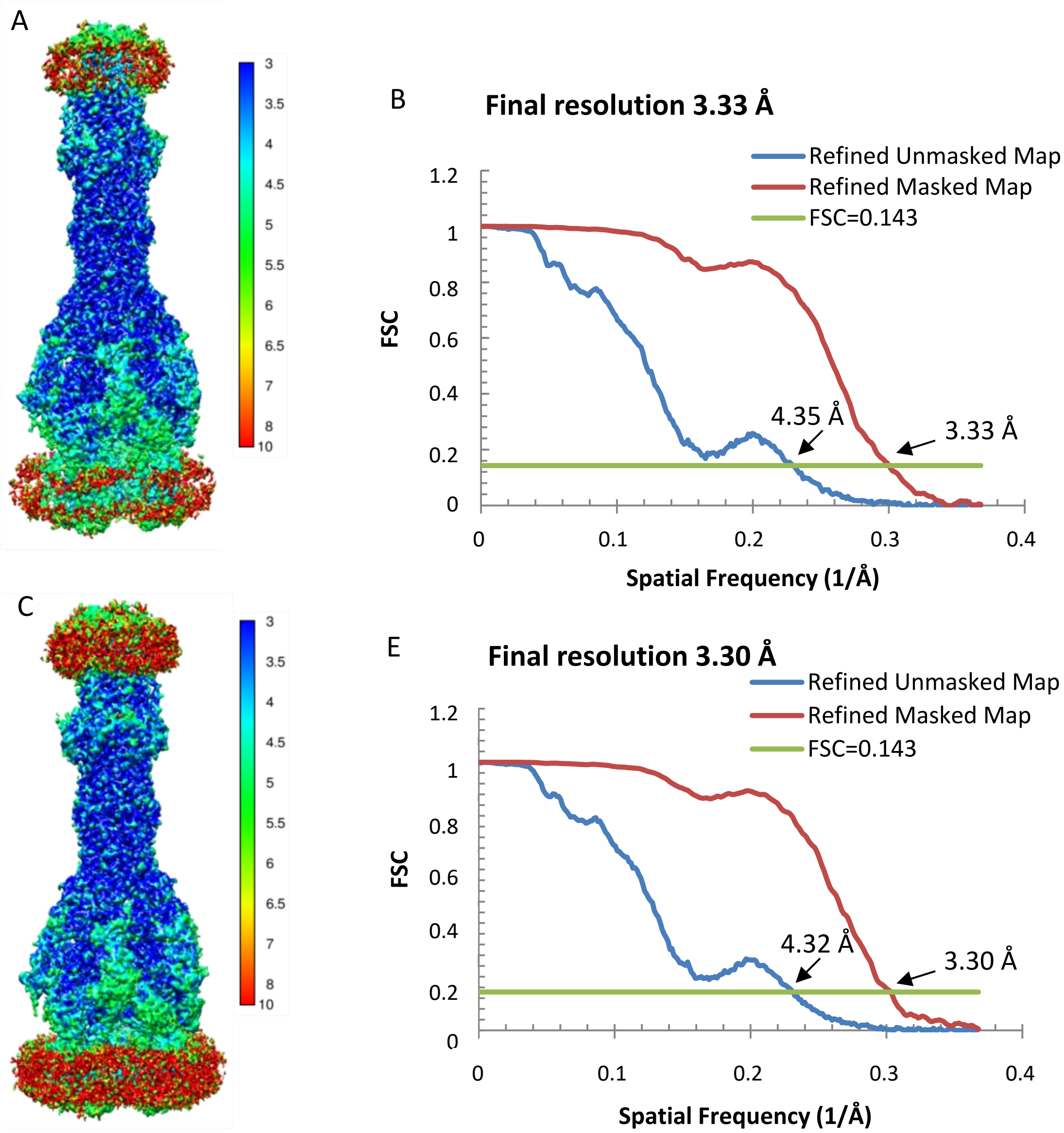

Figure 48- Resmap representations of the two assemblies of MexA-MexB-OprM pump with C3 symmetry

Local resolution determined by ResMaps of the density maps of the assembly 1 (A) at a global resolution of 3.33 Å and the assembly 2 (D) at a global resolution of 3.30 Å. The particle distribution over 360° is represented by the Euler angle distribution map (B and E). The resolution of the assemblies (unmasked and masked refined density maps) is estimated by the Fourier Shell Correlation (FSC) with a cutoff at 0.143 (C and E).

1.2.1. Atomic model built from cryo-EM MexA-MexB-OprM efflux systems

The Assembly 1 and Assembly 2 reconstructed with imposed C3 symmetry are used to build-up the near-atomic model of the entire efflux system MexA-MexB-OprM (Figure 49). These near-atomic structures provide details on protein-protein interactions of the different partners. The X-ray structures used for model construction are MexA (2V4D), MexB (2V50) and OprM (4Y1K). The near-atomic model construction is performed using Chimera, COOT and Phenix for the refinement. This work has been done in collaboration with Dr Isabelle Broutin (Paris Descartes). In brief, the crystal structures are fitted into the cryoEM map in Chimera. Then a manual matching for each amino acid is operated in COOT allowing to account with the conformational changes. Finally, the atomic model is refined in Phenix. The model presented below corresponds to the Assembly 1. Six molecules of MexA interact with the trimer of OprM. Because each subunit of OprM has an internal repeat, it can bind two MexA molecules. Also six molecules of MexA interact with the three subunits of MexB. Due to their interaction with each MexB subunit, one molecule of MexA contacts MexB surface (named MexA-intra) and the other is positioned at the interface of the MexB subunits (named MexA-inter). In addition, the complete structure of MexA is resolved now. Indeed, the full MP domain and the N-terminal of MexA have been modelled.

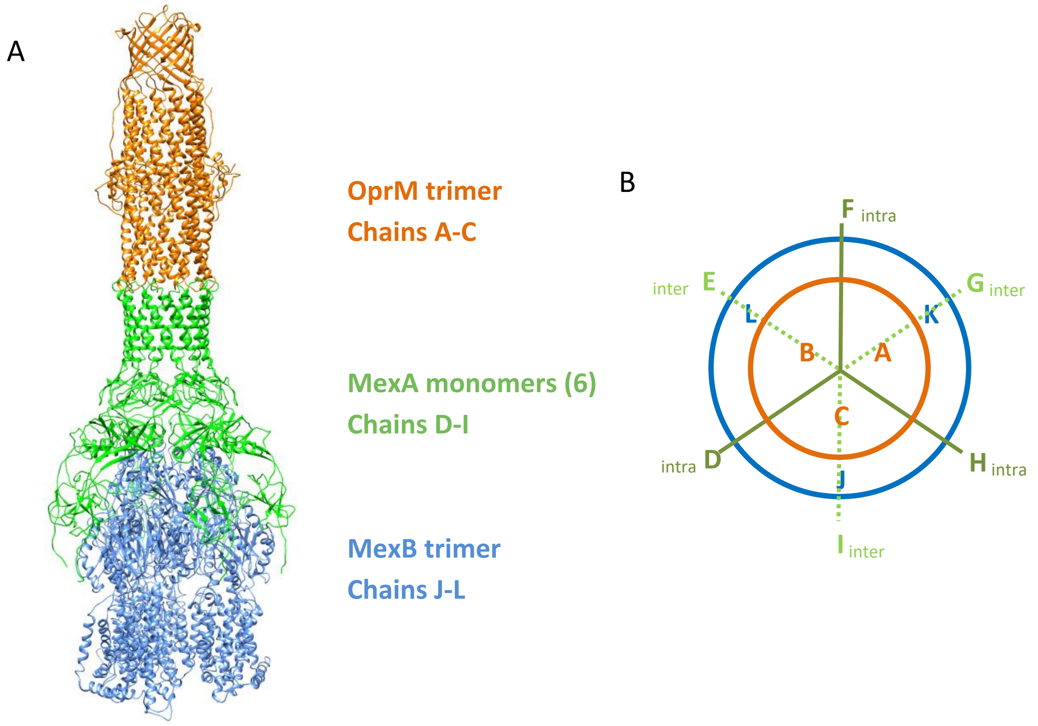

Figure 49- Atomic model of MexA-MexB-OprM pump corresponding to the Assembly 1

The atomic model of the MexA-MexB-OprM pump (A) is composed of OprM trimer in orange for the chain A to C and 6 MexA monomers in green for the chain D to I and MexB trimer in blue for the chains J to L (B). The MexA are characterized by their positioning with respect to MexB as inter- MexB (chains E, I and G) or intra-MexB (chains D, H and F).

1.2.2. Tip to tip interactions between OprM and MexA

The near-atomic model reveals a “tip-to-tip” interaction of the channel protein OprM and the 6 adaptor proteins MexA. The interaction is characterised by a helix-turn-helix (HTH) motif between both protein types (Figures 49 A, 50 inset). For the sake of clarity, I will describe the contact involving the protomer corresponding to the chain C with MexA monomers corresponding to the chains H and I.

The H_7TH_8 of the OprM protomer (chain C) and the HTH of MexA intra (chain H) interact by the three amino acid pairs G199-Q109, V206-S107, A203-Q104 (Figure 45). The H_3TH_4 of the OprM protomer interacts with MexA inter (chain I) in three binding sites by the amino acid pairs G407-Q109, V408-S107, Y411-Q104. In addition to the tip to tip contact, extra contacts are present (for clarity they are not fully described in the figure):

- The OprM protomer (chain C) interacts in H7 with the adjacent MexA intra-protomer (chain D) by the amino acid pairs R403-A105, K402-D103 and T406-R96.
- The adjacent OprM protomer (chain A) interacts with MexA intra-protomer (chain H) by the amino acid pairs R403-A105, K402-D103 and T406-R96.

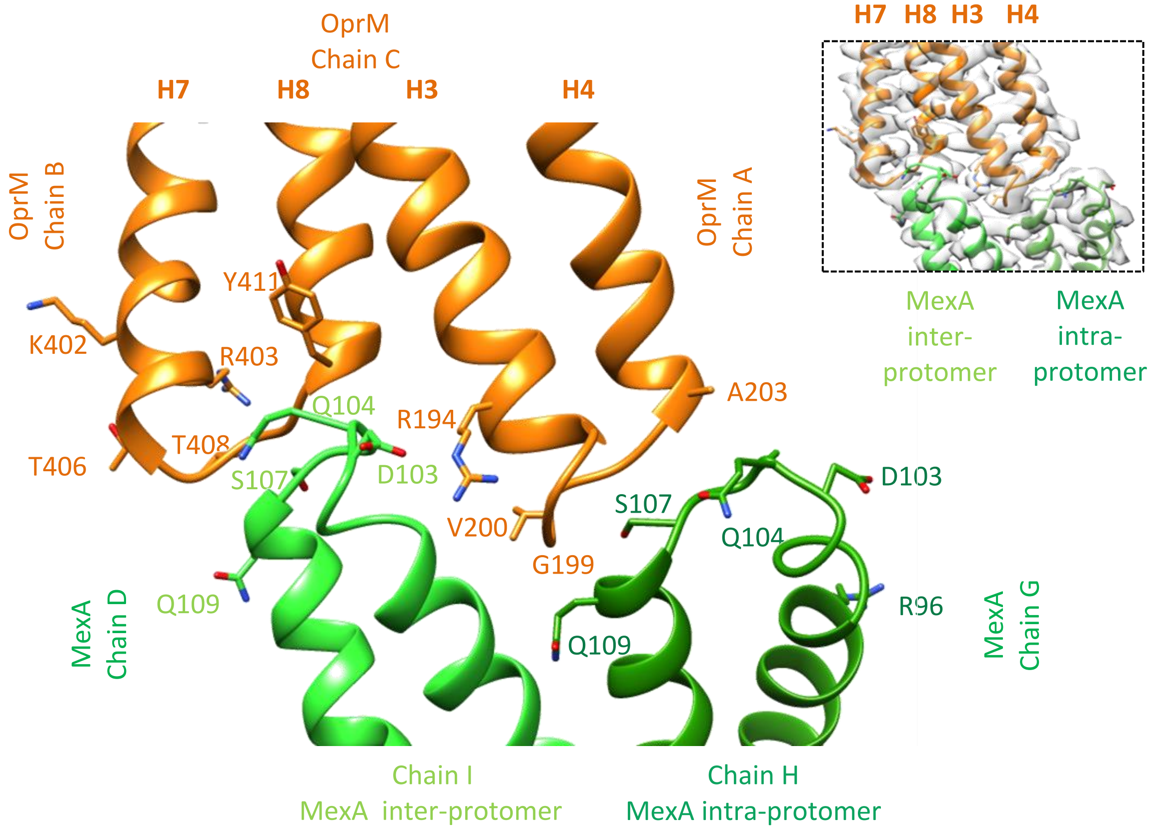

Figure 50- Interaction of OprM protomer with inter- and intra MexA monomers

The ribbon representation of OprM protomer (chain C) and inter- / intra-MexA (chain I, H) highlights the side chains through which the two partners interact. The inset presents the helix-turn-helix interaction of the ribbon atomic structures fitted into the cryo-EM density map.

1.2.3. Comparison of MexA-intra and MexA-inter molecules

The MexA-inter and MexA-intra are superimposed in chimera in order to discriminate structural similarities and differences. As a reminder, they are composed of the four sub-domains (α-helical hairpin, lipoyl domain, β-barrel domain, membrane proximal domains) and in a N-terminal end holding a lipid moiety (Figure 51 A and B). The α-helical hairpin and lipoyl domains show a well superimposition while a shift is observed for β-barrel and membrane proximal domains as well as the N-terminal segment (Figure 51 C). This shift reflects the flexibility of MexA to accommodate the binding on MexB at two different positions.

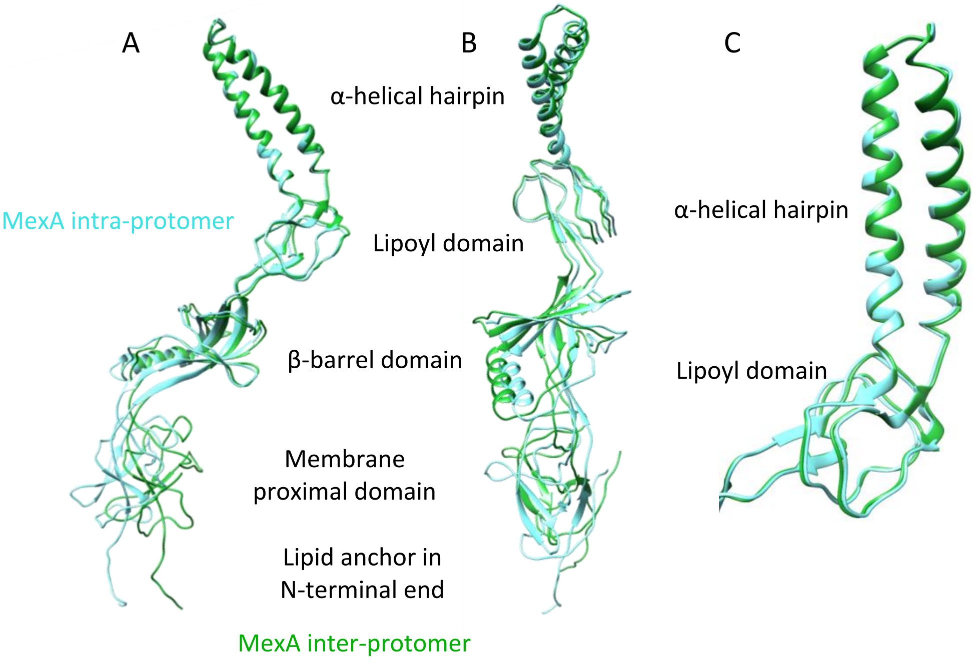

Figure 51- Structure comparison of inter-and intra- MexA molecules

The ribbon representation of superposed inter- and intra- MexA respectively presented in green and light blue from a side view (A and C) and front view (B). The structures are fitted in Chimera with the MatchMarker command.

1.2.4. Interaction of MexA with MexB

MexA-inter interacts with the MexB protomer (chain J) via two domains (Figure 52 A). The β-barrel domain of MexA binds to the DN domain of MexB through the amino acid pairs R34-P255 and G232-K252 (Figure 52 B). The membrane proximal domain of MexA binds to the PN2 domain of MexB through the amino acid pairs Q330-Q319, K280-Y182 and D278-R764 (Figure 52 C).

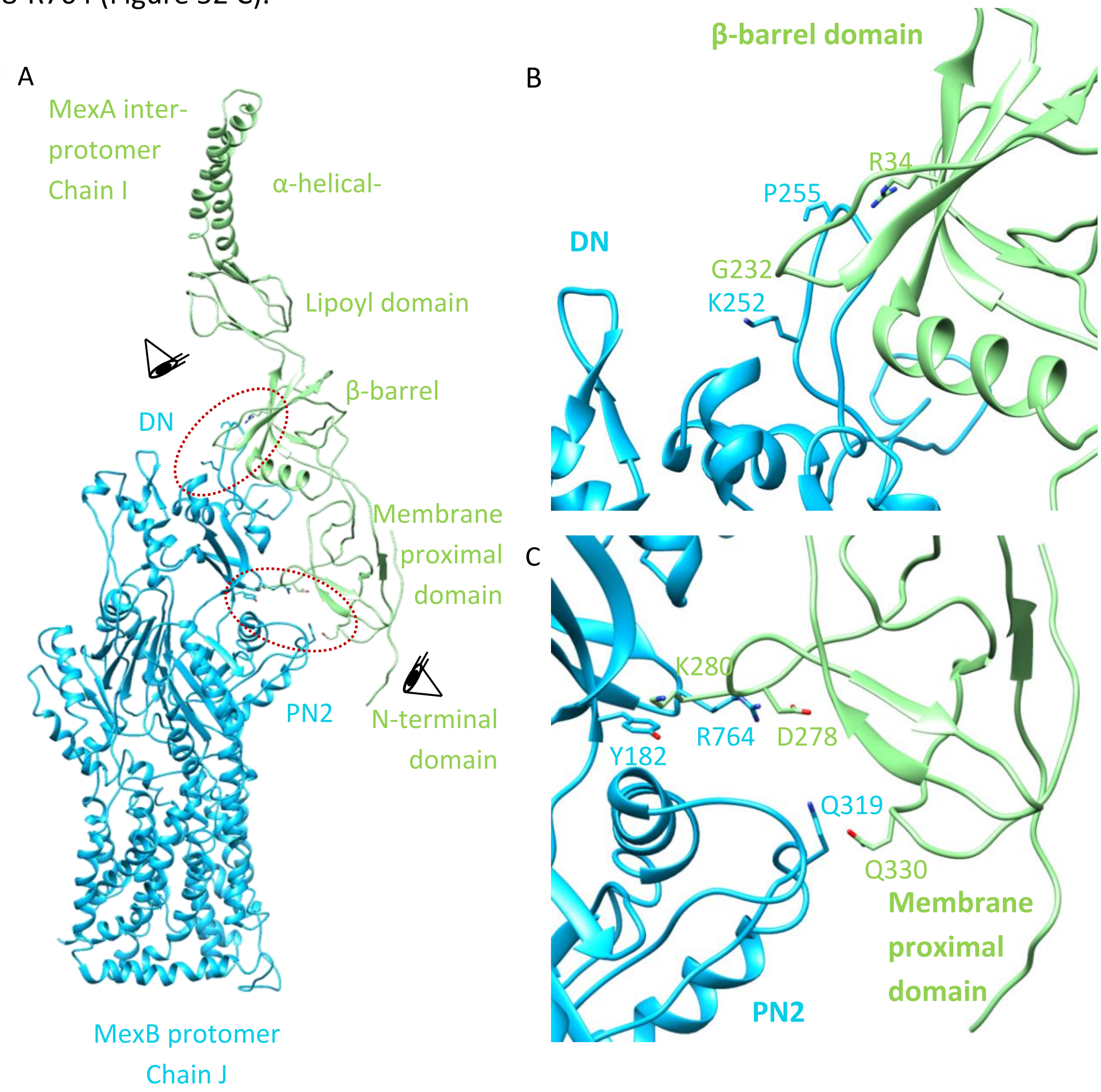

Figure 52- MexA inter- interaction with MexB

The ribbon representation of the MexA inter- interacting with the MexB protomer (chain J). A zoom of the MexA-inter/MexB protein interaction sites is observed from the two viewing points, highlighted by the eye symbols onto arrowed red ellipsis (A). Both zooms (B and C) present interaction sites.

MexA-intra interacts with the MexB protomer via two domains (Figure 53 A). The MexA intra (chain H) interacts with the MexB protomers (chain K) by the β-barrel domain to the DC domain through the amino acid pairs R34-S195, T182-N801, G232-N792, T233-E796 and F254-S195. The membrane proximal domain binds to the PC2 domain through the amino acid pairs through the amino acid pairs E14-K659, G325-K659, Q327-A661 (Figure 53 A). The MexA intra-protomer (chain H) presents a third interaction site by binding the long hairpin of the DN domain from adjacent MexB (chain J) through the amino acid pairs Q272-Q229, Q273-Q229 and Q307-Q229 (Figure 53 A and C).

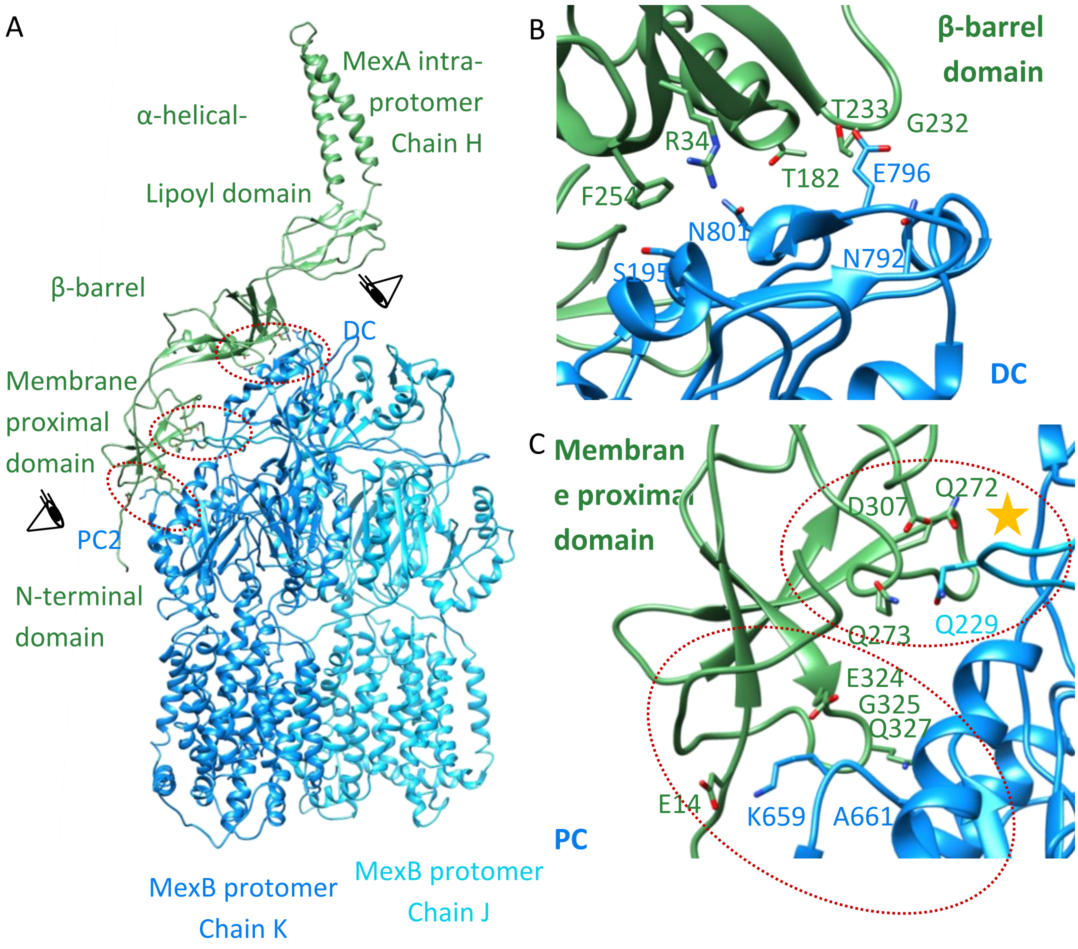

Figure 53- MexA intra- interaction with MexB

Ribbon representation of MexA intra- interacting with the MexB protomers (chain K and J). Three binding sites were highlighted with arrowed red ellipsis (A and C) and the long hairpin of the MexB (chain J) is highlighted by a yellow star (C).

1.3. *MexA anchored into Nanodiscs*

To get more detailed information on the MexA anchored into the Nanodisc (Figure 45), I perform a masked 3D classification without alignment focused on MexA moiety, using a similar approach as for the OprM-ND part. Therefore, the mask is generated using an extended part around MP domain (Mask #3). The set of 90,853 particles is sorted out into 5 classes among which one class contains almost all the particles. This class shows thin densities of MexA that protrude from the six MP domains and extend up to the Nanodisc (Figure 54). This result indicates clearly that all the MexA molecules are anchored into the Nanodisc.

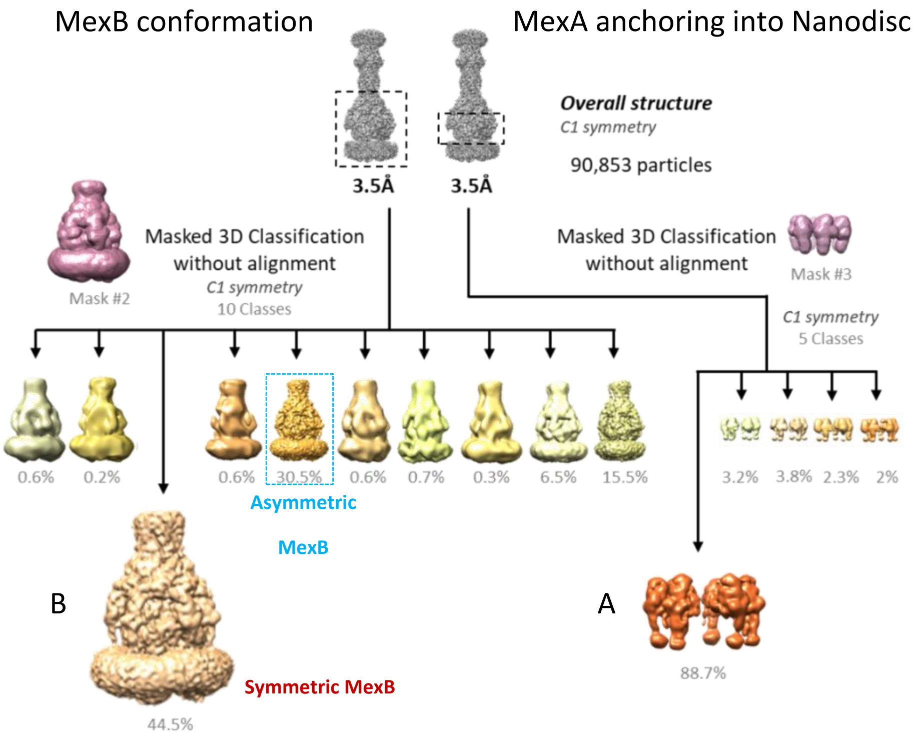

Figure 54- Investigation of partial cryo-EM density maps with focus on MexA and on MexA-B

The investigation of MexA N-terminal positioning into the Nanodisc is performed as previously by masked 3D classification from the reference structure. The number of MexA anchored into the Nanodisc is determined by sorting the integral particles in masked three-dimensional classification without alignment and masking the MP domain and N-terminal domain of MexA. The main class presents 6 intact N-terminal domains (A). The discrimination of different conformational arrangements is achieved by masking on the MexA-MexB-ND and sorting all the particles into 10 classes. 3 major classes are sorted with 44.5% (B), 30.5% and 15.5% of the entire dataset.

1.4. MexB is an asymmetric trimer in the tripartite complex

To get more detailed information on the MexB conformation (Figure 54), I perform a masked 3D classification without alignment focused on MexA-MexB moiety. Therefore, the mask is generated from the reference, by erasing the corresponding part of the OprM-ND (Mask #2). The set of 90,853 particles is sorted out into 10 classes among which three classes contained almost all the particles (Figure 54). The main class with 44.5% of the total particles reveals a MexB in symmetric conformational arrangement in access conformation. The second class with 30.5% of the total particles reveals to be completely asymmetric in access/loose-binding/tight-extrusion/open (LTO) conformation resembling the asymmetric MexB PDB structure 2V50.

The hypothesis is made, that only one conformation of MexB could exist in the *in vitro* reconstructed MexA-MexB-OprM efflux system in the absence of substrate. Thus, to verify this hypothesis, the total set of 90755 particles is submitted to a masked 3D classification without alignment focussing on MexB. The result shows that three classes with the same number of particles have been obtained revealing that MexB is asymmetric in the LTO conformation and that the classes differ by a rotation of 0°, 120° and 240° (Figure 55).

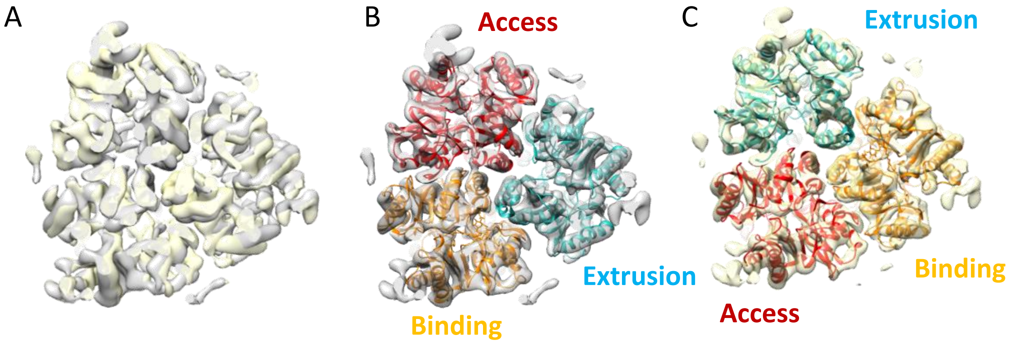

Figure 55- Asymmetric trimer of MexB in the efflux pump MexA-MexB-OprM

Three classes showing asymmetric MexB in three different orientations 0°, 120° and 240° and matching the crystal MexB PDB 2V50 in the access (chain A coloured in red), the binding (chain B coloured in orange) and the extrusion (chain C coloured in blue) conformations.

These are very recent results in the image analysis. The analysis of Assembly 1 and 2 showing an asymmetric MexB are ongoing.

2. Discussion and conclusion onto structural insights and function of the efflux system by comparing the efflux pumps – MexA-MexB-OprM from Pseudomonas aeruginosa and AcrA-AcrB-TolC from Escherichia coli

In the following paragraphs, I will discuss the obtained results from the MexA-MexB-OprM compelex and compare them to the results from the AcrA-AcrB-TolC and AcrA-AcrBZ-TolC efflux systems studied by Wang *et al.*, (2017) .

The cryo-EM sample of the MexA-MexB-OprM efflux pump is prepared in the absence of substrate, in the perspective to study apo-state efflux system. The computational image analysis of the efflux system reveals a fully open channel protein OprM at the periplasmic end. This suggests that the efflux pump is a fully open system in a “resting” state i.e. in the absence of substrate (Figure 56). These results do not agree with the apo-state presented by Wang *et al.*, (2017) .

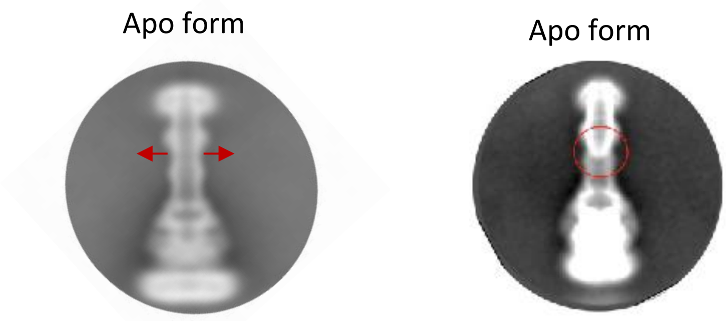

MexA-MexB-OprM
Pseudomonas aeruginosa

AcrA-AcrB-TolC
Escherichia coli

Adapted from Wang *et al.*, 2017

Figure 56- Comparative of apo-state conformation in *P. aeruginosa* and *E. coli*

The representation shows averaged 2D projections of apo-state efflux pump, presenting an open channel for MexA-MexB-OprM complex stabilized by two Nanodiscs and a closed channel for a disulfide-bound AcrA-AcrB-TolC complex stabilized by amphipol (Wang *et al.*, 2017).

Indeed, the AcrA-AcrB-TolC was engineered by over-expressing disulfide-bound AcrA$_{S273C}$ -AcrB$_{S258C}$ and TolC which were co-purified and stabilized by amphipol (Wang *et al.*, 2017). The 2D projection and the 6.5 Å structure revealed a closed channel conformation and was named apo-form by the authors. However, our structure of MexA-MexB-OprM presents an open channel conformation in apo-state, which could suggest, that disulfide-binding of AcrA $_{S273C}$ -AcrB $_{S258C}$ in the AcrA-AcrB-TolC may prevent the opening of the channel protein during the assembly of the tripartite complex.

The channel protein OprM interacts with the adaptor MexA in a “tip-to-tip” interaction (Figures 49, 50, 57). The α-helical hairpins of MexA establish similar contacts with the two HTH of OprM suggesting that the two MexA molecules defined as MexA-inter and MexA- intra do not have a preferential interaction with either H_7TH_8 or H_3TH_4 of OprM. This observation is supported by the existence of two complexes, Assembly 1 and Assembly 2, showing two positions for OprM (corresponding to a 60° rotation with respect to MexB). This means that MexA-intra interacts with H_7TH_8 and H_3TH_4 with the same occurrence. This is also true for MexA-inter (Figure 52). A similar rotation of TolC is also mentioned for AcrA-AcrB-TolC complexes produced in the bacteria, indicating that these two assemblies have a biological relevance and are not artefact products because of *in vitro* conditions.

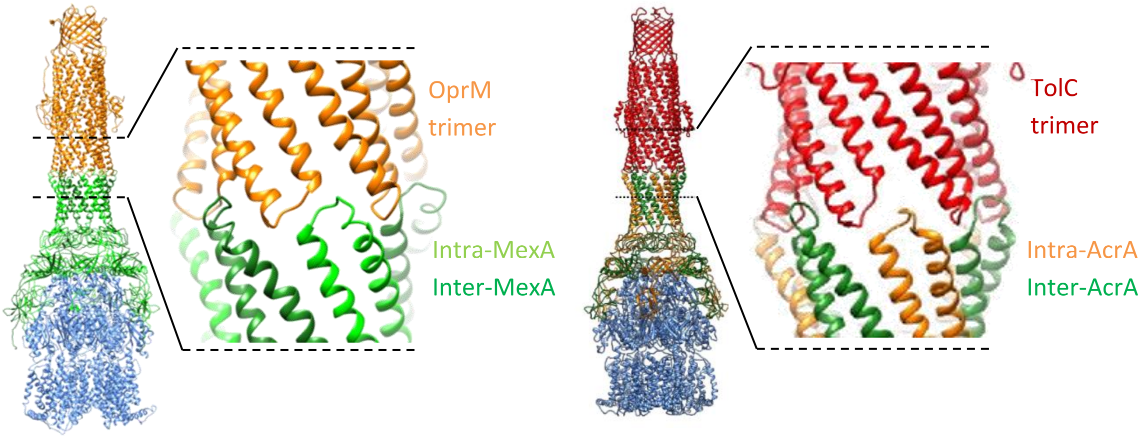

MexA-MexB-OprM
Pseudomonas aeruginosa

AcrA-AcrBZ-TolC puromycin bound
Escherichia coli

Adapted from by Wang *et al.*, 2017

Figure 57- Comparison of MexA-OprM interactions in apo-state and AcrA-TolC interactions in puromycin bound efflux complex

The representation of the near-atomic model of MexA-MexB-OprM and AcrA-AcrBZ-TolC with a focus on the “tip-to-tip” interaction.

The two MexA molecules (MexA-inter-and MexA- intra) have a conformation very similar to the two AcrA molecules interacting with AcrB when engaged in the AcrA-AcrBZ-TolC complexes containing a ligand or an inhibitor as described by Wang *et al.* (2017). Divergences are clearly observed when comparing with AcrA-AcrB-TolC complex in apo-state (Figure 58 A). Superimposition of MexA-MexB-OprM complex and AcrA-AcrB-TolC complex reveals that the nascent ducts built by the MexA/AcrA are similar before diverging in size and shape towards the channel protein (Figure 58 B 1). The duct formed by MexA is tighter (Figure 58 B 2), and is sealed unlike the one formed by AcrA presenting flared α-helical hairpin domains (Figure 58 B 3). It is worth to note that due to the conformation of AcrA, the position of TolC is shifted vertically of about 1 nm and do not superimpose with OprM.

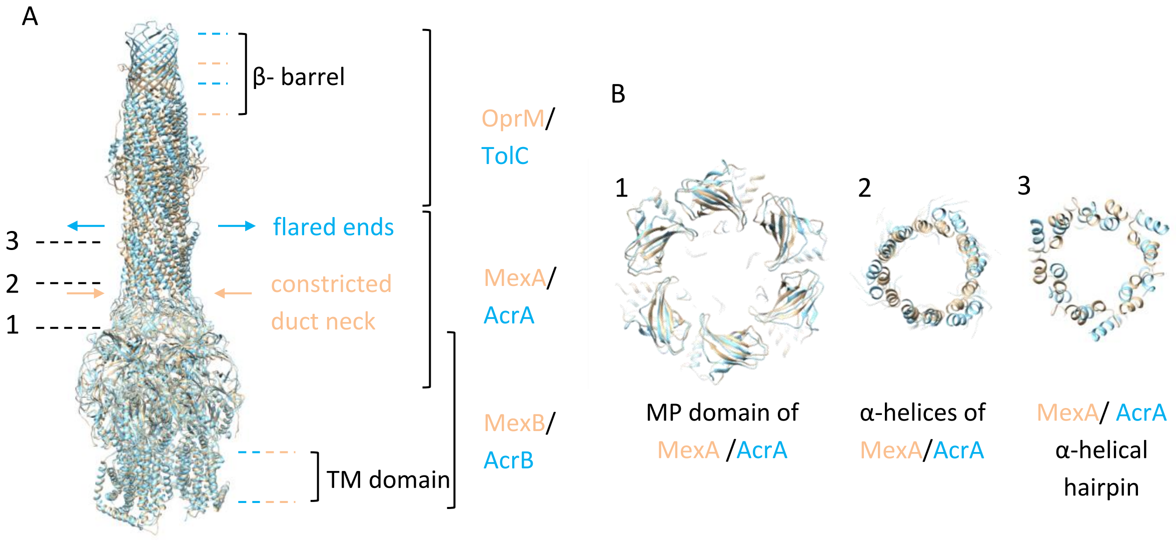

Figure 58 - Comparison of apo-state MexA-MexB-OprM and AcrA-AcrB-TolC

The ribbon representation corresponds to the superimposition of MexA-MexB-OprM (coloured in light orange) and AcrA-AcrB-TolC (coloured in light blue) in apo-state (5V5S). Both near-atomic models were fitted in Chimera with MatchMarker using Needleman-Wunsch alignment algorithm and BLOSUM-80 matrix (A). The horizontal sliced views of the fitted ducts from near-atomic models MexA-MexB-OprM and AcrA-AcrB-TolC present representative structural feature: the MP domain (B1), structure of nascent ducts (B2); α-helices of MexA and AcrA; α-helical hairpin of MexA (B3).

Finally, the structure of MexA-MexB-OprM complex is much more similar to the ligand/inhibitor forms of AcrA-AcrB-TolC complexes than to the so-called apo-form described in (Wang et al., 2017). It is likely that our MexA-MexB-OprM tripartite system assembles in an open conformation, corresponding to a ready to use conformation, and not, as suggested by Wang, that the ligand triggering the opening of the channel. As a reminder, the structure of AcrA-AcrBZ-TolC described by the same group in 2014 (Du *et al.*, 2014) was in an open conformation despite the absence of ligand. Obviously, further investigations are needed for a complete understanding of the assembly process.

General discussion and conclusion

6. General discussion and conclusion

Today, membrane proteins are of great biomedical importance as they represent about half of all drug targets but they represent less than 10 % of the structures in the Protein Data Bank. This low abundance of structures is due to difficulties related to the expression and purification of membrane proteins and to limitations of the techniques used for determining their structure, i.e. X-ray crystallography, nuclear magnetic resonance (NMR) and electron microscopy (EM). For decades, X-ray crystallography provides the vast majority of known atomic-resolution structures of soluble protein. For membrane proteins, X-ray crystallography is hindered by the hydrophobic nature of the membrane-embedded domains of membrane proteins and by the presence of the detergent that limited crystal growth or/and its well-ordered quality. NMR spectroscopy is another well-established technique for protein structure determination at atomic resolution. For NMR studies, proteins have to be isotope-labelled, that is rather challenging for membrane proteins due to their expression level. Commonly, NMR techniques are suitable for small proteins, even though, solid-state NMR has the capability to study membrane proteins reconstituted into lipid bilayers. The crowding of the many signals produced by large proteins remains an issue also for NMR techniques.

The structure determination of membrane proteins by single-particle cryoEM has recently gained substantial attraction as new developments have paved a way to determine the structure of membrane proteins, even at atomic resolution. Single-particle reconstruction is a cryoEM approach that does not require crystals but can produce structures from images of individual molecules in solution. The procedure involves several steps: (i) specimen preparation by vitrification, (ii) imaging in the electron microscope, (iii) picking and windowing the particles, (iv) correction for the contrast transfer function, (v) grouping of the particles into homogeneous 2D classes (2D classification), (vi) reconstruction of an initial 3D map, (vii) grouping of the particles into homogeneous 3D classes (3D classification), (viii) refinement of the density map(s) and finally (ix) map validation and interpretation, which at sufficiently high resolution means the building and validation of an atomic model.

Before discussing all these steps regarding my work, there is an important step dealing with the membrane protein stabilization that is key parameter for having a homogenous population of molecules. Indeed, the first objective of my thesis was the reconstitution of the tripartite efflux complex that is made of three membrane proteins, channel protein OprM, the transporter MexB and adapter protein MexA. Therefore, the stabilization of the component in membrane-mimetic system is obviously of great importance.

6.1 Membrane proteins stabilized in Nanodisc

Traditional membrane mimetics such as micelles or vesicles are proved to be powerful but possess drawbacks. Experimentally, detergent–micelles were not suitable for forming the tripartite complex. Mixing the three purified proteins (OprM, MexA and MexB) together did not lead to the formation of complexes as observed by EM. On the contrary, the formation of the complex can be achieved using vesicles as described by Verchère *et al.* (2014) This experiment teaches us that the lipid bilayers may be an important parameter for forming the complex. Since the use of vesicles is not easy in Single Particle cryoEM, another system has to be employed. The recent design of Nanodisc forming nano-sized particle stabilized by membrane scaffold protein seems to be a better membrane mimetic than detergent as it provides a lipid bilayer environment and homogenous samples. The chapter 2 is dedicated to the reconstitution of the tripartite pump using Nanodiscs. A first method described by Daury *et al.* (2016) consists in mixing MexA in detergent-buffer with OprM and MexB both inserted into Nanodiscs. Though efficient, this method suffers some drawbacks because of the presence of the detergent. The complexes were not stable enough over time, and that was an important limitation when preparing cryoEM grids. To overcome this difficulty, I modified the protocol by inserting MexA and MexB into a Nanodisc in one step. The following step consists in mixing the OprM in Nanodisc with MexA-MexB in Nanodisc in a detergent-free buffer. This protocol is much more suitable for cryoEM study as shown in Chapter 5 with the determination of the near atomic structure of the tripartite complex. It has to be mentioned that both protocols lead to identical assemblies as compared to the structure from Daury *et al.* (2016) and the structure presented in Chapter 5. To conclude for this part, the Nanodisc is well suited for assembling the tripartite complex because it provides the lipid environment required for stabilizing MexA via its lipid anchor at the vicinity of MexB. Beyond the particular aspect of this protein complex, I have worked on a simplified and efficient method for stabilizing membrane proteins with the membrane scaffold protein. The presence of extra lipid is not mandatory, that is a new advance in harnessing the MSP potential to stabilize membrane proteins (Article submitted for publication).

6.2 Preparation of cryo-EM grid

Stabilization of the protein complex being achieved, the next step is the grid preparation. Single-particle EM also has a notable advantage for the study of membrane proteins, as it only requires small amounts of proteins compared to these other structural techniques. Despite of that, the concentration of the tripartite complex was rather low due to a low yield of its assembly. Therefore, I was limited in preparing several cryo-EM grids (that is mandatory for data collection). As presented in Chapter 3, the use of a thin support transparent to electron allows using diluted sample as for negative-staining because the molecules stick to the support. It allows sparing my sample and preparing a large number of grids. The graphene oxide support retains the particles on the grid surface Bokori-Brown *et al.* (2016) with a low affinity. Indeed, the step of removing the excess of sample (blotting step) needs a special care because the entire sample could be easily removed. The advantage of this support is that the molecules can keep different orientations and are also nicely distributed within the ice layer.

6.3 Data collection on high resolution microscopes

The recent introduction of direct electron detector (DDD) cameras for imaging led single-particle cryo-EM in a new era. Because only very low electron doses can be used to image biological samples in ice, it is essential that the detector records the image with excellent signal to noise performance as its detective quantum efficiency (DQE) covers a large spatial frequency range. Another advantage of DDD cameras is their high readout rates, which enable fractionation of a single exposure into a series of frames. Correction for the specimen movements occurring between these frames is computationally compensated thus minimizing image blurring and better preserving high-resolution information.

I have collected data on three high resolution electron microscopes all equipped with DDD cameras (as developed in chapter 4). The collects with Arctica and Polara allow determining a structure of the tripartite complex at 6 to 7 Å resolution. The collect with the Krios provides a much better resolution. Even though the Krios was equipped with the same camera (K2 summit) as the Polara, it additionally possesses an energy filter (GIF Quantum LS Imaging Filter). For our samples it seems, that the combination of electron counting and energy filter, is well adapted to take images with a small defocus. Thus high-resolution information is better preserved, while still providing enough image contrast for particle picking and alignment. Another element that should not be neglected is the number of processed particles. From the last collect, about 90,000 particles were included in the calculation of the 3D reconstruction at 3.5 Å (Chapter 5 first reference structure). This represents a much more important data set than for the two other data collections.

6.4 Image processing and 3D classification

The much better quality of the images also dramatically improves the effectiveness of image-processing steps, such as image alignment and 3D classification, to computationally deal with specimen heterogeneity. Indeed, to produce high-resolution cryo-EM maps, it is critical to separate not only particles in different orientations into different groups but also particles that represent different conformations. 2D classification is very useful to group particle images into homogeneous 2D classes. 2D images and class averages contain limited information, so 2D classification does not allow distinguishing between classes that represent different 3D structures. This is done by 3D classification implemented in RELION2.1 (Scheres, 2012) .

The 3D classification was very efficient for highlighting the presence of two assemblies of our tripartite system (Chapter 5). Assembly 1 and Assembly 2 have been separated by a particular focus on the OprM structure and have a 3.8 Å and 3.74 Å resolution respectively. The OprM of the Assembly 2 is rotated by 60° compared to the Assembly 1 considering MexB in a fixed position. The 3D classification has been useful to reveal the three conformations of MexB trimer in all the images used in the first reference structure.

6.5 3D structure of tripartite complex in lipid environment

A 3D reconstruction of MexA-MexB-OprM sandwiched between two Nanodiscs, is achieved at 3.8 Å resolution. Considering that no substrate was added, the efflux pump shows an apo state conformation with a fully open channel protein OprM. Structural features reveal N-terminal end anchored into Nanodisc for the channel protein OprM and six MexA fusion proteins. Both proteins interact with a “tip-to-tip” connection. The trimeric MexB in the tripartite complex adopts an asymmetric conformation with each subunit being in loose-tight-open (LTO) conformation which suggests that the efflux system is in a ready-to-use conformation. This structure resembles the one of TolC-AcrAB determined in ligand and inhibitor states (Wang *et al.*, 2017) and is different their so-called “apo-form” (see Chapter 5 for details).

This tripartite structure could be integrated into the antibiotic efflux cycle and describes a state that is probably a resting state. The complex forms an open conduit to evacuate the drugs carried by MexB that uses the proton motive force as a source of energy.

The existence of Assembly 1 and Assembly 2 gives some clue on the assembly process. The OprM molecule interacts with the hexamer of MexA. The MexA-intra or MexA-inter have undefined role in the binding of OprM. One aspect that has not been discussed until now is the structure of MexA-MexB in the Nanodiscs. EM characterization of MexA-MexB in Nanodisc does not reveal an assembly like it is observed in the tripartite complex. MexA molecules are seen around MexB but do not show the remarkable hexameric organization revealed in the tripartite complex. One hypothesis could be that the OprM molecule is responsible of the hexameric structure of MexA. Assembly 1 and Assembly 2 support this hypothesis but do not inform if three or six molecules of MexA are needed to catch OprM, and that is a key step. Further experiments are needed to fully decipher the assembly process.

This work opens new perspective for structural studies of other conformational states of the efflux system in "energized" conditions to fulfill our understanding of the efflux cycle mechanism. Moreover, the knowledge of this first tripartite native complex structure constitutes the first step towards the development of molecules capable of blocking the assembly of the complex for therapeutic uses. Indeed, such molecules would inhibit active efflux and restore the lost efficacy of current antibiotics.

Bibliography

Akama, H., Kanemaki, M., Yoshimura, M., Tsukihara, T., Kashiwagi, T., Yoneyama, H., Narita, S., Nakagawa, A., and Nakae, T. (2004a). Crystal Structure of the Drug Discharge Outer Membrane Protein, OprM, of *Pseudomonas aeruginosa*: DUAL MODES OF MEMBRANE ANCHORING AND OCCLUDED CAVITY END. J. Biol. Chem. *279*, 52816–52819.

Akama, H., Matsuura, T., Kashiwagi, S., Yoneyama, H., Narita, S., Tsukihara, T., Nakagawa, A., and Nakae, T. (2004b). Crystal Structure of the Membrane Fusion Protein, MexA, of the Multidrug Transporter in *Pseudomonas aeruginosa*. J. Biol. Chem. *279*, 25939–25942.

Andersen, C., Koronakis, E., Bokma, E., Eswaran, J., Humphreys, D., Hughes, C., and Koronakis, V. (2002). Transition to the open state of the TolC periplasmic tunnel entrance. Proc. Natl. Acad. Sci. U. S. A. *99*, 11103–11108.

Autzen, H.E., Myasnikov, A.G., Campbell, M.G., Asarnow, D., Julius, D., and Cheng, Y. (2018). Structure of the human TRPM4 ion channel in a lipid nanodisc. Science *359*, 228–232.

Banerjee, S., Bartesaghi, A., Merk, A., Rao, P., Bulfer, S.L., Yan, Y., Green, N., Mroczkowski, B., Neitz, R.J., Wipf, P., et al. (2016). 2.3 Å resolution cryo-EM structure of human p97 and mechanism of allosteric inhibition. Science *351*, 871–875.

Bavro, V.N., Pietras, Z., Furnham, N., Pérez-Cano, L., Fernández-Recio, J., Pei, X.Y., Misra, R., and Luisi, B. (2008). Assembly and Channel Opening in a Bacterial Drug Efflux Machine. Mol. Cell *30*, 114–121.

Bavro, V.N., Marshall, R.L., and Symmons, M.F. (2015). Architecture and roles of periplasmic adaptor proteins in tripartite efflux assemblies. Front. Microbiol. *6*.

Bayburt, T.H., and Sligar, S.G. (2002). Single-molecule height measurements on microsomal cytochrome P450 in nanometer-scale phospholipid bilayer disks. Proc. Natl. Acad. Sci. U. S. A. *99*, 6725–6730.

Bayburt, T.H., Grinkova, Y.V., and Sligar, S.G. (2006). Assembly of single bacteriorhodopsin trimers in bilayer nanodiscs. Arch. Biochem. Biophys. *450*, 215–222.

Bokori-Brown, M., Martin, T.G., Naylor, C.E., Basak, A.K., Titball, R.W., and Savva, C.G. (2016). Cryo-EM structure of lysenin pore elucidates membrane insertion by an aerolysin family protein. Nat. Commun. *7*, 11293.

Bolla, J.-M., Alibert-Franco, S., Handzlik, J., Chevalier, J., Mahamoud, A., Boyer, G., Kieć-Kononowicz, K., and Pagès, J.-M. (2011). Strategies for bypassing the membrane barrier in multidrug resistant Gram-negative bacteria. FEBS Lett. *585*, 1682–1690.

Brusaferro, S., Arnoldo, L., Cattani, G., Fabbro, E., Cookson, B., Gallagher, R., Hartemann, P., Holt, J., Kalenic, S., Popp, W., et al. (2015). Harmonizing and supporting infection control training in Europe. J. Hosp. Infect. *89*, 351–356.

Cong, Y., and Ludtke, S.J. (2010). Single particle analysis at high resolution. Methods Enzymol. *482*, 211–235.

Costa, T.R.D., Felisberto-Rodrigues, C., Meir, A., Prevost, M.S., Redzej, A., Trokter, M., and Waksman, G. (2015). Secretion systems in Gram-negative bacteria: structural and mechanistic insights. Nat. Rev. Microbiol. *13*, 343–359.

Crowther, R.A., Amos, L.A., Finch, J.T., De Rosier, D.J., and Klug, A. (1970). Three dimensional reconstructions of spherical viruses by fourier synthesis from electron micrographs. Nature *226*, 421–425.

Dandey, V.P., Wei, H., Zhang, Z., Tan, Y.Z., Acharya, P., Eng, E.T., Rice, W.J., Kahn, P.A., Potter, C.S., and Carragher, B. (2017). Spotiton: New Features and Applications.

Daury, L., Orange, F., Taveau, J.-C., Verchère, A., Monlezun, L., Gounou, C., Marreddy, R.K.R., Picard, M., Broutin, I., Pos, K.M., et al. (2016). Tripartite assembly of RND multidrug efflux pumps. Nat. Commun. *7*, 10731.

Daury, L., Taveau, J.-C., Salvador, D., Glavier, M., and Lambert, O. (2017). Reconstitution of Membrane Proteins into Nanodiscs for Single-Particle Electron Microscopy. In Membrane Protein Structure and Function Characterization: Methods and Protocols, J.-J. Lacapere, ed. (New York, NY: Springer New York), pp. 317–327.

Davin-Regli, A., Bolla, J.-M., James, C.E., Lavigne, J.-P., Chevalier, J., Garnotel, E., and Pages, A.M. and J.-M. (2008). Membrane Permeability and Regulation of Drug “Influx and Efflux” in Enterobacterial Pathogens.

De Rosier, D.J., and Klug, A. (1968). Reconstruction of three dimensional structures from electron micrographs. Nature *217*, 130–134.

Delmar, J.A., and Yu, E.W. (2016). The AbgT family: A novel class of antimetabolite transporters: AbgT Family of Antimetabolite Transporters. Protein Sci. *25*, 322–337.

Delmar, J.A., Su, C.-C., and Yu, E.W. (2014). Bacterial multi-drug efflux transporters. Annu. Rev. Biophys. *43*, 93–117.

Denisov, I.G., Grinkova, Y.V., Lazarides, A.A., and Sligar, S.G. (2004). Directed Self-Assembly of Monodisperse Phospholipid Bilayer Nanodiscs with Controlled Size. J. Am. Chem. Soc. *126*, 3477–3487.

Dezi, M., Fribourg, P.-F., Cicco, A.D., Jault, J.-M., Chami, M., and Lévy, D. (2011). Binding, reconstitution and 2D crystallization of membrane or soluble proteins onto functionalised lipid layer observed in situ by reflected light microscopy. J. Struct. Biol. *174*, 307–314.

Du, D., and Luisi, B.F. (2015). Bacterial multidrug efflux pumps. Antibiot. Antibiot. Resist. 6.

Du, D., Wang, Z., James, N.R., Voss, J.E., Klimont, E., Ohene-Agyei, T., Venter, H., Chiu, W., and Luisi, B.F. (2014). Structure of the AcrAB-TolC multidrug efflux pump. Nature *509*, 512–515.

Dubochet, J., and McDowall, A.W. (1981). Vitrification of Pure Water for Electron Microscopy. J. Microsc. *124*, 3–4.

Dubochet, J., Adrian, M., Chang, J.-J., Homo, J.-C., Lepault, J., McDowall, A.W., and Schultz, P. (1988). Cryo-electron microscopy of vitrified specimens. 100.

Eades, C.P. 12 S. 2017By C., Hughes, S., Heard, K., and Moore, L.S. (2017). Antimicrobial therapies for Gram-positive infections.

Eicher, T., Cha, H., Seeger, M.A., Brandstätter, L., El-Delik, J., Bohnert, J.A., Kern, W.V., Verrey, F., Grütter, M.G., Diederichs, K., et al. (2012a). Transport of drugs by the multidrug transporter AcrB involves an access and a deep binding pocket that are separated by a switch-loop. Proc. Natl. Acad. Sci. *109*, 5687–5692.

Eicher, T., Seeger, M.A., Anselmi, C., Zhou, W., Brandstätter, L., Verrey, F., Diederichs, K., Faraldo-Gómez, J.D., and Pos, K.M. (2014). Coupling of remote alternating-access transport mechanisms for protons and substrates in the multidrug efflux pump AcrB. ELife *3*.

Elkins, C.A., and Nikaido, H. (2003). Chimeric Analysis of AcrA Function Reveals the Importance of Its C-Terminal Domain in Its Interaction with the AcrB Multidrug Efflux Pump. J. Bacteriol. *185*, 5349–5356.

Fernandez-Recio, J., Walas, F., Federici, L., Pratap, J.V., Bavro, V.N., Miguel, R.N., Mizuguchi, K., and Luisi, B. (2004). A model of a transmembrane drug-efflux pump from Gram-negative bacteria. FEBS Lett. *578*, 5–9.

Ferrandez, Y., Monlezun, L., Phan, G., Benabdelhak, H., Benas, P., Ulryck, N., Falson, P., Ducruix, A., Picard, M., and Broutin, I. (2012). Stoichiometry of the MexA-OprM binding, as investigated by blue native gel electrophoresis. Electrophoresis *33*, 1282–1287.

Fischer, N., and Kandt, C. (2011). Three ways in, one way out: Water dynamics in the trans-membrane domains of the inner membrane translocase AcrB. Proteins Struct. Funct. Bioinforma. *79*, 2871–2885.

Fralick, J.A. (1996). Evidence that TolC is required for functioning of the Mar/AcrAB efflux pump of Escherichia coli. J. Bacteriol. *178*, 5803–5805.

Frank, J. (1975). Averaging of low exposure electron micrographs of non-periodic objects. Ultramicroscopy *1*, 159–162.

Gao, H., Zhou, Z., Rawat, U., Huang, C., Bouakaz, L., Wang, C., Cheng, Z., Liu, Y., Zavialov, A., Gursky, R., et al. (2007). RF3 Induces Ribosomal Conformational Changes Responsible for Dissociation of Class I Release Factors. Cell *129*, 929–941.

Ge, Q., Yamada, Y., and Zgurskaya, H. (2009). The C-Terminal Domain of AcrA Is Essential for the Assembly and Function of the Multidrug Efflux Pump AcrAB-TolC. J. Bacteriol. *191*, 4365–4371.

Girard, R., Perraud, M., Herriot, H.E., Prüss, A., Savey, A., Tikhomirov, E., Thuriaux, M., Vanhems, P., and Bernard, U.C. (2002). WORLD HEALTH ORGANIZATION. 72.

Grassucci, R.A., Taylor, D.J., and Frank, J. (2007). Preparation of macromolecular complexes for cryo-electron microscopy. Nat. Protoc. *2*, 3239–3246.

Guan, L., and Nakae, T. (2001). Identification of Essential Charged Residues in Transmembrane Segments of the Multidrug Transporter MexB of Pseudomonas aeruginosa. J. Bacteriol. *183*, 1734–1739.

Hassan, K.A., Liu, Q., Henderson, P.J.F., and Paulsen, I.T. (2015). Homologs of the Acinetobacter baumannii AceI Transporter Represent a New Family of Bacterial Multidrug Efflux Systems. MBio *6*.

Hayashi, K., Nakashima, R., Sakurai, K., Kitagawa, K., Yamasaki, S., Nishino, K., and Yamaguchi, A. (2016). AcrB-AcrA Fusion Proteins That Act as Multidrug Efflux Transporters. J. Bacteriol. *198*, 332–342.

Henderson, R., Baldwin, J.M., Ceskat, T.A., Zemlin, F., Beckmann, E., and Downing, K.H. (1990). Model for the Structure of Bacteriorhodopsin Based on High-resolution Electron Cryo-microscopy. 31.

Higgins, C.F. (1992). ABC Transporters: From Microorganisms to Man. Annu. Rev. Cell Biol. *8*, 67–113.

Higgins, M.K., Bokma, E., Koronakis, E., Hughes, C., and Koronakis, V. (2004). Structure of the periplasmic component of a bacterial drug efflux pump. Proc. Natl. Acad. Sci. U. S. A. *101*, 9994–9999.

Hobbs, E.C., Yin, X., Paul, B.J., Astarita, J.L., and Storz, G. (2012). Conserved small protein associates with the multidrug efflux pump AcrB and differentially affects antibiotic resistance. Proc. Natl. Acad. Sci. U. S. A. *109*, 16696–16701.

Husain, F., Bikhchandani, M., and Nikaido, H. (2011). Vestibules Are Part of the Substrate Path in the Multidrug Efflux Transporter AcrB of Escherichia coli ▿ . J. Bacteriol. *193*, 5847–5849.

Hvorup, R.N., Winnen, B., Chang, A.B., Jiang, Y., Zhou, X.-F., and Saier, M.H. (2003). The multidrug/oligosaccharidyl-lipid/polysaccharide (MOP) exporter superfamily. Eur. J. Biochem. *270*, 799–813.

Jack, D.L., Yang, N.M., and Saier, M.H. (2001). The drug/metabolite transporter superfamily. Eur. J. Biochem. *268*, 3620–3639.

Kanonenberg, K., Schwarz, C.K.W., and Schmitt, L. (2013). Type I secretion systems - a story of appendices. Res. Microbiol. *164*, 596–604.

Kelly, D.F., Dukovski, D., and Walz, T. (2008). Monolayer purification: A rapid method for isolating protein complexes for single-particle electron microscopy. Proc. Natl. Acad. Sci. *105*, 4703–4708.

Kim, J.-S., Jeong, H., Song, S., Kim, H.-Y., Lee, K., Hyun, J., and Ha, N.-C. (2015). Structure of the Tripartite Multidrug Efflux Pump AcrAB-TolC Suggests an Alternative Assembly Mode. Mol. Cells *38*, 180–186.

Koronakis, V., Sharff, A., Koronakis, E., Luisi, B., and Hughes, C. (2000). Crystal structure of the bacterial membrane protein TolC central to multidrug efflux and protein export. Nature *405*, 914–919.

Kostyuchenko, V.A., Chew, P.L., Ng, T.-S., and Lok, S.-M. (2014). Near-Atomic Resolution Cryo-Electron Microscopic Structure of Dengue Serotype 4 Virus. J. Virol. *88*, 477–482.

Lai, L.-Y., Lin, T.-L., Chen, Y.-Y., Hsieh, P.-F., and Wang, J.-T. (2018). Role of the Mycobacterium marinum ESX-1 Secretion System in Sliding Motility and Biofilm Formation. Front. Microbiol. *9*.

Lévy, D., Mosser, G., Lambert, O., Moeck, G.S., Bald, D., and Rigaud, J.-L. (1999). Two-Dimensional Crystallization on Lipid Layer: A Successful Approach for Membrane Proteins. J. Struct. Biol. *127*, 44–52.

Li, X.-Z., and Nikaido, H. (2009). Efflux-Mediated Drug Resistance in Bacteria: an Update. Drugs *69*, 1555–1623.

Li, X., Mooney, P., Zheng, S., Booth, C., Braunfeld, M.B., Gubbens, S., Agard, D.A., and Cheng, Y. (2013). Electron counting and beam-induced motion correction enable near atomic resolution single particle cryoEM. Nat. Methods *10*, 584–590.

Li, X.-Z., Zhang, L., and Poole, K. (1998). Role of the Multidrug Efflux Systems of Pseudomonas aeruginosa in Organic Solvent Tolerance. J. Bacteriol. *180*, 2987–2991.

Lim, S.P., and Nikaido, H. (2010). Kinetic parameters of efflux of penicillins by the multidrug efflux transporter AcrAB-TolC of Escherichia coli. Antimicrob. Agents Chemother. *54*, 1800–1806.

Liu, Y., Gonen, S., Gonen, T., and Yeates, T.O. (2018). Near-atomic cryo-EM imaging of a small protein displayed on a designed scaffolding system. Proc. Natl. Acad. Sci. *115*, 3362–3367.

Lobedanz, S., Bokma, E., Symmons, M.F., Koronakis, E., Hughes, C., and Koronakis, V. (2007). A periplasmic coiled-coil interface underlying TolC recruitment and the assembly of bacterial drug efflux pumps. Proc. Natl. Acad. Sci. U. S. A. *104*, 4612–4617.

Lopez, J., and Feldman, M.F. (2018). Expanding the molecular weaponry of bacterial species. J. Biol. Chem. *293*, 1515–1516.

Matias, V.R.F., Al-Amoudi, A., Dubochet, J., and Beveridge, T.J. (2003). Cryo-Transmission Electron Microscopy of Frozen-Hydrated Sections of Escherichia coli and Pseudomonas aeruginosa. J. Bacteriol. *185*, 6112–6118.

Merk, A., Bartesaghi, A., Banerjee, S., Falconieri, V., Rao, P., Davis, M.I., Pragani, R., Boxer, M.B., Earl, L.A., Milne, J.L.S., et al. (2016). Breaking Cryo-EM Resolution Barriers to Facilitate Drug Discovery. Cell *165*, 1698–1707.

Mikolosko, J., Bobyk, K., Zgurskaya, H.I., and Ghosh, P. (2006). Conformational Flexibility in the Multidrug Efflux System Protein AcrA. Struct. Lond. Engl. 1993 *14*, 577–587.

Monlezun, L., Phan, G., Benabdelhak, H., Lascombe, M.-B., Enguéné, V.Y.N., Picard, M., and Broutin, I. (2015). New OprM structure highlighting the nature of the N-terminal anchor. Front. Microbiol. *6*.

Murakami, S., Nakashima, R., Yamashita, E., and Yamaguchi, A. (2002). Crystal structure of bacterial multidrug efflux transporter AcrB. Nature *419*, 587–593.

Murakami, S., Nakashima, R., Yamashita, E., Matsumoto, T., and Yamaguchi, A. (2006). Crystal structures of a multidrug transporter reveal a functionally rotating mechanism. Nature *443*, 173–179.

Nagano, K., and Nikaido, H. (2009). Kinetic behavior of the major multidrug efflux pump AcrB of Escherichia coli. Proc. Natl. Acad. Sci. U. S. A. *106*, 5854–5858.

Nakashima, R., Sakurai, K., Yamasaki, S., Nishino, K., and Yamaguchi, A. (2011). Structures of the multidrug exporter AcrB reveal a proximal multisite drug-binding pocket. Nature *480*, 565–569.

Narita, S., Eda, S., Yoshihara, E., and Nakae, T. (2003). Linkage of the efflux-pump expression level with substrate extrusion rate in the MexAB–OprM efflux pump of Pseudomonas aeruginosa. Biochem. Biophys. Res. Commun. *308*, 922–926.

Nikaido, H. (2018). RND transporters in the living world. Res. Microbiol.

Nikaido, H., and Pagès, J.-M. (2012). Broad Specificity Efflux pumps and Their Role in Multidrug Resistance of Gram Negative Bacteria. FEMS Microbiol. Rev. *36*, 340–363.

Nikaido, H., and Takatsuka, Y. (2009). Mechanisms of RND multidrug efflux pumps. Biochim. Biophys. Acta BBA - Proteins Proteomics *1794*, 769–781.

Noble, A.J., Dandey, V.P., Wei, H., Brasch, J., Chase, J., Acharya, P., Tan, Y.Z., Zhang, Z., Kim, L.Y., Scapin, G., et al. (2017). Routine single particle CryoEM sample and grid characterization by tomography. 42.

Ntsogo Enguéné, V.Y., Verchère, A., Phan, G., Broutin, I., and Picard, M. (2015). Catch me if you can: a biotinylated proteoliposome affinity assay for the investigation of assembly of the MexA-MexB-OprM efflux pump from Pseudomonas aeruginosa. Front. Microbiol. *6*, 541.

Pagès, J.-M., James, C.E., and Winterhalter, M. (2008). The porin and the permeating antibiotic: a selective diffusion barrier in Gram-negative bacteria. Nat. Rev. Microbiol. *6*, 893–903.

Pages, J.-M., Lavigne, J.-P., Leflon-Guibout, V., Marcon, E., Bert, F., Noussair, L., and Nicolas-Chanoine, M.-H. (2009). Efflux Pump, the Masked Side of ß-Lactam Resistance in Klebsiella pneumoniae Clinical Isolates. PLoS ONE *4*.

Palmer, T., and Berks, B.C. (2012). The twin-arginine translocation (Tat) protein export pathway. Nat. Rev. Microbiol. *10*, 483–496.

Palovcak, E., Wang, F., Zheng, S.Q., Yu, Z., Li, S., Bulkley, D., Agard, D.A., and Cheng, Y. (2018). A simple and robust procedure for preparing graphene-oxide cryo-EM grids.

Pao, S.S., Paulsen, I.T., and Saier, M.H. (1998). Major Facilitator Superfamily. MICROBIOL MOL BIOL REV *62*, 34.

Pei, X.-Y., Hinchliffe, P., Symmons, M.F., Koronakis, E., Benz, R., Hughes, C., and Koronakis, V. (2011). Structures of sequential open states in a symmetrical opening transition of the TolC exit duct. Proc. Natl. Acad. Sci. U. S. A. *108*, 2112–2117.

Phan, G., Benabdelhak, H., Lascombe, M.-B., Benas, P., Rety, S., Picard, M., Ducruix, A., Etchebest, C., and Broutin, I. (2010). Structural and Dynamical Insights into the Opening Mechanism of P. aeruginosa OprM Channel. Structure *18*, 507–517.

Piddock, L.J.V. (2006). Multidrug-resistance efflux pumps - not just for resistance. Nat. Rev. Microbiol. *4*, 629–636.

Poole, K. (2007). Efflux pumps as antimicrobial resistance mechanisms. Ann. Med. *39*, 162–176.

Pos, K.M. (2009). Drug transport mechanism of the AcrB efflux pump. Biochim. Biophys. Acta BBA - Proteins Proteomics *1794*, 782–793.

Raka, L., Zoutman, D., Mulliqi, G., Krasniqi, S., Dedushaj, I., Raka, N., Ahmeti, S., Shala, M., Vishaj, A., and Elezi, Y. (2006). Prevalence of nosocomial infections in high-risk units in the university clinical center of Kosova. Infect. Control Hosp. Epidemiol. *27*, 421–423.

Rawling, E.G., Brinkman, F.S.L., and Hancock, R.E.W. (1998). Roles of the Carboxy-Terminal Half of Pseudomonas aeruginosa Major Outer Membrane Protein OprF in Cell Shape, Growth in Low-Osmolarity Medium, and Peptidoglycan Association. J. Bacteriol. *180*, 3556–3562.

Ritchie, T.K., Grinkova, Y.V., Bayburt, T.H., Denisov, I.G., Zolnerciks, J.K., Atkins, W.M., and Sligar, S.G. (2009). Reconstitution of Membrane Proteins in Phospholipid Bilayer Nanodiscs. In Methods in Enzymology, (Elsevier), pp. 211–231.

Scheres, S.H.W. (2010). Classification of Structural Heterogeneity by Maximum-Likelihood Methods. In Methods in Enzymology, (Elsevier), pp. 295–320.

Scheres, S.H.W. (2012). A Bayesian View on Cryo-EM Structure Determination. J. Mol. Biol. *415*, 406–418.

Scheres, S.H.W., Gao, H., Valle, M., Herman, G.T., Eggermont, P.P.B., Frank, J., and Carazo, J.-M. (2007). Disentangling conformational states of macromolecules in 3D-EM through likelihood optimization. Nat. Methods *4*, 27–29.

Seeger, M.A., Schiefner, A., Eicher, T., Verrey, F., Diederichs, K., and Pos, K.M. (2006). Structural Asymmetry of AcrB Trimer Suggests a Peristaltic Pump Mechanism. Science *313*, 1295–1298.

Seeger, M.A., von Ballmoos, C., Eicher, T., Brandstätter, L., Verrey, F., Diederichs, K., and Pos, K.M. (2008a). Engineered disulfide bonds support the functional rotation mechanism of multidrug efflux pump AcrB. Nat. Struct. Mol. Biol. *15*, 199–205.

Seeger, M.A., Diederichs, K., Eicher, T., Brandstätter, L., Schiefner, A., Verrey, F., and Pos, K.M. (2008b). The AcrB efflux pump: conformational cycling and peristalsis lead to multidrug resistance. Curr. Drug Targets *9*, 729–749.

Sennhauser, G., Amstutz, P., Briand, C., Storchenegger, O., and Grütter, M.G. (2006). Drug Export Pathway of Multidrug Exporter AcrB Revealed by DARPin Inhibitors. PLoS Biol. *5*, e7.

Sennhauser, G., Bukowska, M.A., Briand, C., and Grütter, M.G. (2009). Crystal Structure of the Multidrug Exporter MexB from Pseudomonas aeruginosa. J. Mol. Biol. *389*, 134–145.

Sigworth, F.J. (1998). A Maximum-Likelihood Approach to Single-Particle Image Refinement. J. Struct. Biol. *122*, 328–339.

Sigworth, F.J., Doerschuk, P.C., Carazo, J.-M., and Scheres, S.H.W. (2010). An Introduction to Maximum-Likelihood Methods in Cryo-EM. In Methods in Enzymology, (Elsevier), pp. 263–294.

Simon, A., Gounou, C., Tan, S., Tiefenauer, L., Di Berardino, M., and Brisson, A.R. (2013). Free-standing lipid films stabilized by Annexin-A5. Biochim. Biophys. Acta BBA - Biomembr. *1828*, 2739–2744.

Su, C.-C., Li, M., Gu, R., Takatsuka, Y., McDermott, G., Nikaido, H., and Yu, E.W. (2006). Conformation of the AcrB Multidrug Efflux Pump in Mutants of the Putative Proton Relay Pathway. J. Bacteriol. *188*, 7290–7296.

Su, C.-C., Long, F., Zimmermann, M.T., Rajashankar, K.R., Jernigan, R.L., and Yu, E.W. (2011). Crystal structure of the CusBA heavy-metal efflux complex of Escherichia coli. Nature *470*, 558–562.

Sugawara, E., Nestorovich, E.M., Bezrukov, S.M., and Nikaido, H. (2006). *Pseudomonas aeruginosa* Porin OprF Exists in Two Different Conformations. J. Biol. Chem. *281*, 16220–16229.

Swint-Kruse, L., and Brown, C.S. (2005). Resmap: automated representation of macromolecular interfaces as two-dimensional networks. Bioinformatics *21*, 3327–3328.

Symmons, M.F., Bokma, E., Koronakis, E., Hughes, C., and Koronakis, V. (2009). The assembled structure of a complete tripartite bacterial multidrug efflux pump. Proc. Natl. Acad. Sci. *106*, 7173–7178.

Symmons, M.F., Marshall, R.L., and Bavro, V.N. (2015). Architecture and roles of periplasmic adaptor proteins in tripartite efflux assemblies. Front. Microbiol. *6*.

Takatsuka, Y., and Nikaido, H. (2006). Threonine-978 in the Transmembrane Segment of the Multidrug Efflux Pump AcrB of Escherichia coli Is Crucial for Drug Transport as a Probable Component of the Proton Relay Network. J. Bacteriol. *188*, 7284–7289.

Takatsuka, Y., Chen, C., and Nikaido, H. (2010). Mechanism of recognition of compounds of diverse structures by the multidrug efflux pump AcrB of Escherichia coli. Proc. Natl. Acad. Sci. U. S. A. *107*, 6559–6565.

Tamura, N., Murakami, S., Oyama, Y., Ishiguro, M., and Yamaguchi, A. (2005). Direct Interaction of Multidrug Efflux Transporter AcrB and Outer Membrane Channel TolC Detected via Site-Directed Disulfide Cross-Linking. Biochemistry *44*, 11115–11121.

Taylor, K.A., and Glaeser, R.M. (2008). Retrospective on the early development of cryoelectron microscopy of macromolecules and a prospective on opportunities for the future. J. Struct. Biol. *163*, 214–223.

Thanassi, D.G., Cheng, L.W., and Nikaido, H. (1997). Active efflux of bile salts by Escherichia coli. J. Bacteriol. *179*, 2512–2518.

Tikhonova, E.B., and Zgurskaya, H.I. (2004). AcrA, AcrB, and TolC of Escherichia coli Form a Stable Intermembrane Multidrug Efflux Complex. J. Biol. Chem. *279*, 32116–32124.

Tikhonova, E.B., Dastidar, V., Rybenkov, V.V., and Zgurskaya, H.I. (2009). Kinetic control of TolC recruitment by multidrug efflux complexes. Proc. Natl. Acad. Sci. U. S. A. *106*, 16416–16421.

Tikhonova, E.B., Yamada, Y., and Zgurskaya, H.I. (2011). Sequential mechanism of assembly of multidrug efflux pump AcrAB-TolC. Chem. Biol. *18*, 454–463.

Törnroth-Horsefield, S., Gourdon, P., Horsefield, R., Brive, L., Yamamoto, N., Mori, H., Snijder, A., and Neutze, R. (2007). Crystal Structure of AcrB in Complex with a Single Transmembrane Subunit Reveals Another Twist. Structure *15*, 1663–1673.

Touzé, T., Eswaran, J., Bokma, E., Koronakis, E., Hughes, C., and Koronakis, V. (2004). Interactions underlying assembly of the Escherichia coli AcrAB–TolC multidrug efflux system. Mol. Microbiol. *53*, 697–706.

Tseng, T.T., Gratwick, K.S., Kollman, J., Park, D., Nies, D.H., Goffeau, A., and Saier, M.H. (1999). The RND permease superfamily: an ancient, ubiquitous and diverse family that includes human disease and development proteins. J. Mol. Microbiol. Biotechnol. *1*, 107–125.

Unwin, P.N.T., and Henderson, R. (1975). Molecular structure determination by electron microscopy of unstained crystalline specimens. J. Mol. Biol. *94*, 425–440.

Vaccaro, L., Koronakis, V., and Sansom, M.S.P. (2006). Flexibility in a Drug Transport Accessory Protein: Molecular Dynamics Simulations of MexA. Biophys. J. *91*, 558–564.

Vargiu, A.V., and Nikaido, H. (2012). Multidrug binding properties of the AcrB efflux pump characterized by molecular dynamics simulations. Proc. Natl. Acad. Sci. U. S. A. *109*, 20637–20642.

Verchère, A., Dezi, M., Broutin, I., and Picard, M. (2014). In vitro Investigation of the MexAB Efflux Pump From Pseudomonas aeruginosa. J. Vis. Exp.

Vogt, A.D., Pozzi, N., Chen, Z., and Di Cera, E. (2014). Essential role of conformational selection in ligand binding. Biophys. Chem. *0*, 13–21.

Wandersman, C., and Delepelaire, P. (1990). TolC, an Escherichia coli outer membrane protein required for hemolysin secretion. Proc. Natl. Acad. Sci. U. S. A. *87*, 4776–4780.

Wang, Z., Fan, G., Hryc, C.F., Blaza, J.N., Serysheva, I.I., Schmid, M.F., Chiu, W., Luisi, B.F., and Du, D. (2017). An allosteric transport mechanism for the AcrAB-TolC multidrug efflux pump. ELife *6*.

Weeks, J.W., Celaya-Kolb, T., Pecora, S., and Misra, R. (2010). AcrA suppressor alterations reverse the drug hypersensitivity phenotype of a TolC mutant by inducing TolC aperture opening. Mol. Microbiol. *75*, 1468–1483.

Yamaguchi, A., Nakashima, R., and Sakurai, K. (2015). Structural basis of RND-type multidrug exporters. Front. Microbiol. *6*.

Yamanaka, H., Tadokoro, S., Miyano, M., Takahashi, E., Kobayashi, H., and Okamoto, K. (2007). Studies on the region involved in the transport activity of Escherichia coli TolC by chimeric protein analysis. Microb. Pathog. *42*, 184–192.

Yoneyama, H., Maseda, H., Kamiguchi, H., and Nakae, T. (2000). Function of the Membrane Fusion Protein, MexA, of the MexA, B-OprM Efflux Pump in *Pseudomonas aeruginosa* without an Anchoring Membrane. J. Biol. Chem. *275*, 4628–4634.

Yoshimura, F., Zalman, L.S., and Nikaido, H. (1983). Purification and properties of Pseudomonas aeruginosa porin. J. Biol. Chem. *258*, 2308–2314.

Yum, S., Xu, Y., Piao, S., Sim, S.-H., Kim, H.-M., Jo, W.-S., Kim, K.-J., Kweon, H.-S., Jeong, M.-H., Jeon, H., et al. (2009). Crystal Structure of the Periplasmic Component of a Tripartite Macrolide-Specific Efflux Pump. J. Mol. Biol. *387*, 1286–1297.

Zgurskaya, H.I. (2009). Multicomponent drug efflux complexes: architecture and mechanism of assembly. Future Microbiol. *4*, 919–932.

Zgurskaya, H.I., and Nikaido, H. (1999). Bypassing the periplasm: Reconstitution of the AcrAB multidrug efflux pump of Escherichia coli. Proc. Natl. Acad. Sci. U. S. A. *96*, 7190–7195.

Zgurskaya, H.I., and Nikaido, H. (2000). Multidrug resistance mechanisms: drug efflux across two membranes. Mol. Microbiol. *37*, 219–225.

Zhang, K. (2016). Gctf: Real-time CTF determination and correction. J. Struct. Biol. *193*, 1–12.

Annexes

Annexe 1- Textbook

Chapter 17

Reconstitution of Membrane Proteins into Nanodiscs for Single-Particle Electron Microscopy

**Laetitia Daury, Jean-Christophe Taveau, Dimitri Salvador,
Marie Glavier, and Olivier Lambert**

Abstract

The structure determination of integral membrane protein (IMP) in lipid environment is particularly challenging. Among emerging methods for exchanging detergent required for IMP purification by original compounds, the use of lipid nanodisc preserves a lipid environment. Compared with the classical method of proteoliposome formation, the nanodisc technology provides a better control of IMP molecules inserted in lipid membrane, therefore giving access to structural methodologies developed for soluble proteins. Here, we present the reconstitution of OprM membrane protein into nanodisc associated with a step of size-exclusion chromatography, an approach applicable to prepare IMPs for subsequent visualization by single-particle electron microscopy.

Key words Membrane protein, Nanodisc, Electron microscopy, Single-particle analysis, Multidrug efflux pump

1 Introduction

For electron microscopy (EM) and other experimental methods investigating the structure and function of integral membrane proteins (IMPs), a challenge is their extraction from their native cellular membranes to obtain a water-soluble, monodisperse, and stable IMP. In the purification step, the IMPs have been removed from the membrane usually by amphiphilic detergents. Recent methodologies have been proposed to exchange or remove the free detergent monomer and micelles by various compounds including amphiphilic polymers (amphipol) [1], small lipid nanodiscs [2], engineered β-sheet peptides [3], or non-exchangeable detergent [4]. Even though the choice of these compounds is related to the purpose of the experiments, the advantage of the nanodisc is such that it well mimics a lipid environment, unlike the others. Based on nascent discoidal HDL particles, nanodiscs (ND) are self-assembled systems of lipid bilayers (8–16 nm in diameter),

Jean-Jacques Lacapere (ed.), *Membrane Protein Structure and Function Characterization: Methods and Protocols*,
Methods in Molecular Biology, vol. 1635, DOI 10.1007/978-1-4939-7151-0_17, © Springer Science+Business Media LLC 2017

stabilized in solution by two amphipathic helical scaffold proteins [2, 5, 6]. Since 2002, a large variety of integral membrane proteins have been incorporated into NDs such as ion channels, transporters, receptors including G protein-coupled receptor, membrane enzymes. Nowadays, ND is an attractive membrane model system for biophysical and biochemical studies of membrane proteins [7]. Their functions and also interactions with ligands, proteins, and lipids have been investigated using techniques such as surface plasmon resonance, mass spectrometry, NMR, SAXS, and EM. The use of ND and single-particle analysis appears as a new trend in membrane protein structure.

In this chapter, OprM represents a typical case to illustrate the use of ND technology. OprM is an external membrane channel (50 kDa) assembled in a trimer forming an exit duct. It belongs to the prototypic bacterial MexAB-OprM multidrug efflux system that actively expels toxic substances and antibiotic out of the cell and strongly contributes to bacterial antibiotic resistance [8] of *Pseudomonas aeruginosa*—a Gram-negative bacterium—causing opportunistic infections in immuno-compromised patients and exhibiting natural and acquired resistance to diverse antibiotics. For several years, we have been working on strategies for the reconstitution of OprM [9–12] in a lipid environment. During the reconstitution process OprM molecules adopt an up-and-down orientation with respect to the lipid membrane, as many other MPs, leading to the formation of small stacks of two-dimensional (2D) arrays [9]. Using cryo electron tomography and single-particle analysis we have been able to study the overall organization of OprM membrane proteins within these stacks [12]. However, the formation of stacks precludes further other biochemical/biophysical studies of OprM. It is possible to circumvent the formation of stacks by the use of ND. Unlike liposome, NDs are very small membrane models suitable to master the reconstitution of membrane proteins. The purpose of the present methodological work, as summarized in Fig. 1, is the use of ND technology followed by size-exclusion chromatography for EM characterization of single-membrane proteins in lipid membrane. We report on the insertion of OprM in ND (OprM-ND), amenable for structural investigations.

2 Materials

1. Detergent: Octyl β-D-glucopyranoside (βOG) and sodium cholate hydrate (Sigma, Saint-Louis, Missouri, USA).
2. Proteins extraction buffer A: 20 mM Tris/Cl pH 8, 10% glycerol (v/v), 15 mM imidazole, 2.5% βOG (w/v).

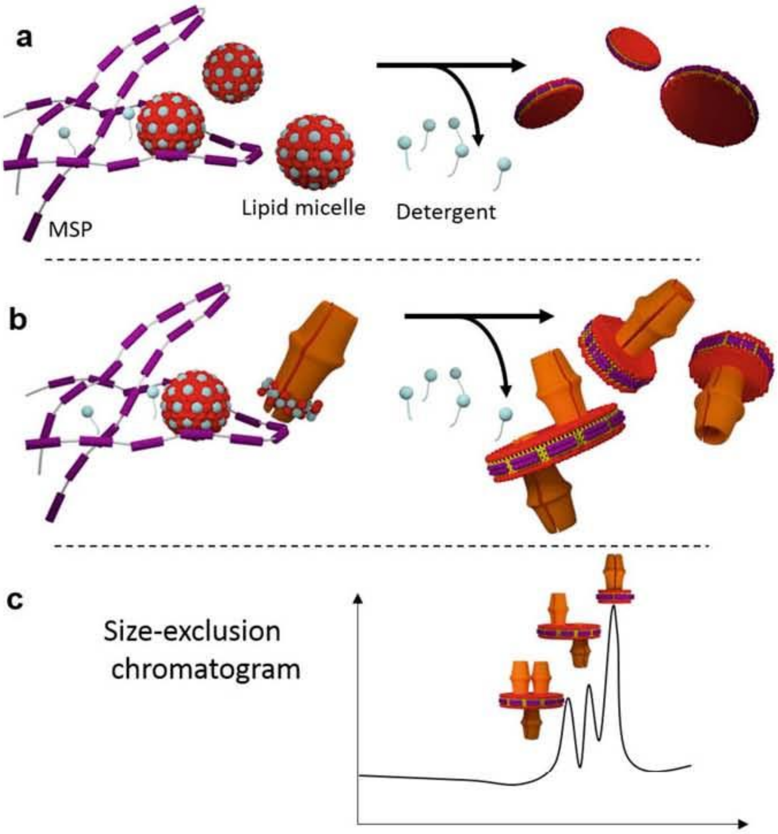

Fig. 1 General scheme of the procedure for the reconstitution of membrane protein in nanodisc (ND) for single-particle electron microscopy analysis. (**a**) Reconstitution of ND. From MSP and lipid/detergent micelles, detergent removal leads to the formation of flat lipid ND. (**b**) Reconstitution of IMP into ND. IMP in detergent is added to the mixture in (**a**). After detergent removal, one or few copies of IMP are inserted into ND. (**c**) The separation/purification of the various species is performed by size-exclusion chromatography (SEC)

3. Lipid: 1-palmitoyl-2-oleoyl-*sn*-glycero-3-phosphocholine (POPC) (Avanti Polar Lipids, Alabaster, AL, USA).
4. Reconstitution buffer (100 mM NaCl, 10 mM Tris/Cl, pH 7.4).
5. Affinity purification: nickel-charged affinity Ni-NTA agarose resin and Polypropylene columns (Invitrogen, Carlsbad, CA, USA). Washing buffer 1: 40 mM Tris/Cl, 0.3 M NaCl, 1% Triton X-100, pH 8.0; Washing buffer 2: 40 mM Tris/Cl, 0.3 M NaCl, 50 mM Na-cholate, 60 mM imidazole, pH 8.0; Washing buffer 3: 40 mM Tris/Cl, 0.3 M NaCl, 100 mM imidazole, pH 8.0. Elution buffer: 40 mM Tris/Cl, 0.3 M NaCl, 0.4 M imidazole.

6. Dialysis buffer MSP: 20 mM Tris/Cl, 0.1 M NaCl, 0.5 mM EDTA, pH 7.4 at 4 °C.
7. Dialysis buffer OprM: 20 mM Tris–HCl pH 8.0, 200 mM NaCl, 10% glycerol (v/v), and 0.9% βOG (w/v).
8. Detergent removal: SM2 Biobeads (Bio-Rad, Hercules, CA, USA).
9. Plasmid: pMSP1D1 from pET28a (Addgene, Cambridge, MA, USA).
10. Bacteria: BL21-Gold (DE3) Competent *E. coli* cells (Agilent Technologies, Santa Clara, CA, USA).
11. Resuspension buffer: 20 mM phosphate buffer, pH 7.4 containing 1 mM Phenylmethylsulfonyl fluoride.
12. Reconstitution solution: 10 mM Tris/Cl, pH 7.4, 100 mM NaCl, 0.9% βOG and 15 mM Na-cholate.
13. Gel filtration: AKTAmicro with a Superdex 200 PC 3.2/30 column (GE Healthcare, Little Chalfont, Great Britain).
14. SEC buffer: 10 mM Tris/Cl, pH 7.4 and 100 mM NaCl.
15. Specimen preparation for TEM, carbon cupper grid (Cu 300 mesh, Agar Scientific, Stansted, Great Britain) and a glow discharge apparatus for carbon treatment (Elmo, Cordouan Technologies, Pessac, France).
16. Transmission electron microscope: FEI F20 (equipped with Field Emission Gun, FEG) operated at 200 kV, and a camera 2 k × 2 k (Gatan, Inc., Pleasanton, CA).
17. Computer for image analysis: standard workstation.

3 Methods

3.1 Lipid Preparation

1. Dissolve POPC lipids in chloroform, dry onto a glass tube under steady flow of nitrogen, and expose to vacuum for 1 h.
2. Suspend the lipid film in the reconstitution buffer and subject to five rounds of sonication for 30 s each.
3. Lipid concentration was quantified by phosphate analysis.

3.2 Protein Purifications

The MSP1D1 membrane scaffold protein expressed and purified from bacteria [13], was used to make OprM nanodiscs (*see* **Note 1**). Briefly, MSP1D1 is obtained as follows:

1. *E. coli* strain BL21 Gold (DE3) is transformed with pMSP1D1 plasmid.
2. Inoculate 5 mL of Luria Broth (LB) medium containing kanamycin (30 mg/L) with a single colony from a freshly streaked

plate and incubate at 37 °C with shaking at 200 rpm until the OD600 is approximately 0.4–0.6.

3. Add the starting culture to 200 mL of LB containing kanamycin (30 mg/L) and incubate at 37 °C with shaking at 200 rpm until the OD600 is approximately 1.5.
4. Add 1 mM IPTG for 2 h at 37 °C under shaking at 200 rpm.
5. Harvest the cells by centrifugation at 4000 × *g* for 30 min. The cell pellet is stored at −80 °C.
6. The bacteria cell pellet is resuspended in resuspension buffer. After the cells are completely resuspended, add 1% Triton X-100, deoxyribonuclease I (25 mg/L), and 50 mM imidazole.
7. Three 1 min rounds sonication permit to lyse the cells.
8. The lysate is then clarified by centrifugation at 30,000 × *g* for 30 min.
9. The lysate is loaded on a nickel-charged affinity Ni-NTA agarose resin in a polypropylene column, equilibrated with 40 mM phosphate buffer, pH 7.4.
10. Incubate for 2 h at 4 °C on a rotating wheel. The column is washed once with washing buffers 1, 2, and 3.
11. MSP1D1 is eluted with elution buffer. 0.5 mL fractions are collected and protein is checked on SDS-PAGE.
12. The fractions containing MSP1D1 are pooled, the sample is dialyzed against dialysis buffer MSP overnight, and stored with 0.01% NaN_3 one week at 4 °C or at −80 °C for long-term storage (*see* **Note 2**).

For OprM membrane protein, purification starts as a standard scheme, with the total solubilization of protein-enriched membranes by detergent. Then, after several purification steps, the protein is purified at a high concentration and maintained soluble in the presence of detergent. The expression and purification of OprM transmembrane proteins follow this standard method [9]. Briefly,

1. The membrane envelopes from broken *E. coli* cells were solubilized in protein extraction buffer A overnight at 20 °C.
2. The solubilized membrane proteins were loaded onto a Ni-NTA resin column and then were eluted with a linear gradient of imidazole (60–500 mM).
3. The fractions containing the OprM protein were pooled and concentrated to 5 mg/mL.
4. Finally, OprM was exchanged for suitable buffer by dialysis against dialysis buffer OprM.

OprM is trimeric in solution and forms a cylindrical structure composed of a transmembrane β barrel and 12 long α helices protruding to the solvent.

3.3 Reconstitution of OprM into Nanodisc

OprM is inserted into nanodiscs (OprM-ND) according to the standard protocol [13, 14] (*see* **Note 3**). Briefly, OprM-ND is obtained as follows:

1. OprM solution is mixed with POPC solution and MSP solution at a final 36:1:0.4 lipids/MSP/protein molar ratio in reconstitution solution for 1 h incubation on ice.
2. Add 200 mg wet SM2 Bio-beads (BB) per ml (corresponding to a ratio BB/detergent of 2 w/w), to remove detergent with gentle agitation to keep the beads suspended, overnight at 4 °C.
3. Add a second amount of BB for 4 h to remove the residual detergent.
4. Then pipette off the supernatant and store at 4 °C for further analysis (*see* **Note 4**).

3.4 Preparation of Negatively Stained Samples

1. The carbon grid is placed inside a glow discharge apparatus to render carbon hydrophilic. Typically, the grid is submitted to a faint red/blue glow for ~40 s under a low pressure of 3×10^{-1} mbar.
2. The sample is then deposited on the carbon side for 30 s and the excess is then removed by touching the edge of the grid with a filter paper.
3. Immediately pipette 5 μL of 2% uranyl acetate solution on the top of the sample and leave it for 2 min. Then remove the excess removed by touching the edge of the grid with a filter paper.
4. Air-dry the grid and store in a plastic box up to EM observation (*see* **Note 5**).

3.5 Electron Microscopy Observation

1. Insert the grid into the electron microscope.
2. At low magnification (×300), search for a homogeneous distribution of the sample and of stain as well.
3. On the selected squares, record the images in the low dose mode condition (Fig. 2). Briefly, the region of interest (ROI) is defined in search mode (~ ×3000). The "low dose" setting enables exposing the ROI only for recording the image (exposure mode × 50,000), the defocus setting being adjusted out the ROI with the focus mode (×50,000).

3.6 Protein Purification by Size Exclusion Chromatography

To sort out the population of OprM-ND according to the number of molecules per ND, the OprM-ND sample was subjected to size exclusion chromatography (SEC) using a Superdex 200 PC 3.2/30 column at a flow rate of 0.03 mL/min (Fig. 3).

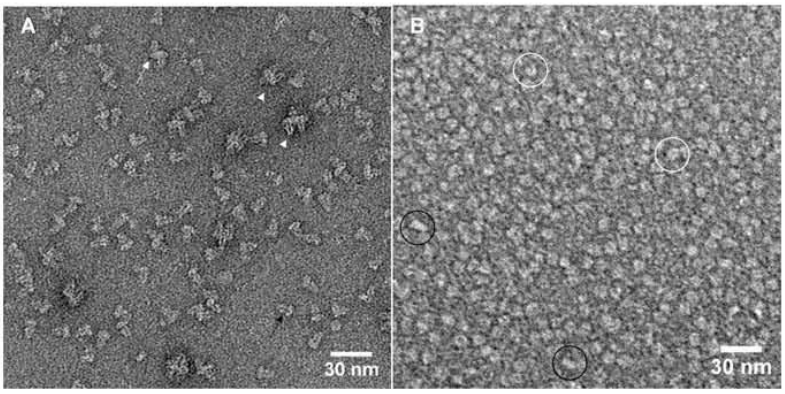

Fig. 2 Negative-stained electron microscopy of OprM molecules inserted in ND (OprM-ND). (**a**) Typical EM image of OprM inserted into ND. OprM molecules are viewed with their long axis preferentially oriented parallel to the carbon support. NDs contain one (*black arrow*), two (*white arrow*), and three OprM molecules (*white arrowheads*), exhibiting a certain reconstitution heterogeneity. (**b**) EM image of reconstitution of ND without the addition of IMP showing top views (*white circles*) and side views (*black circles*). Scale bars 30 nm

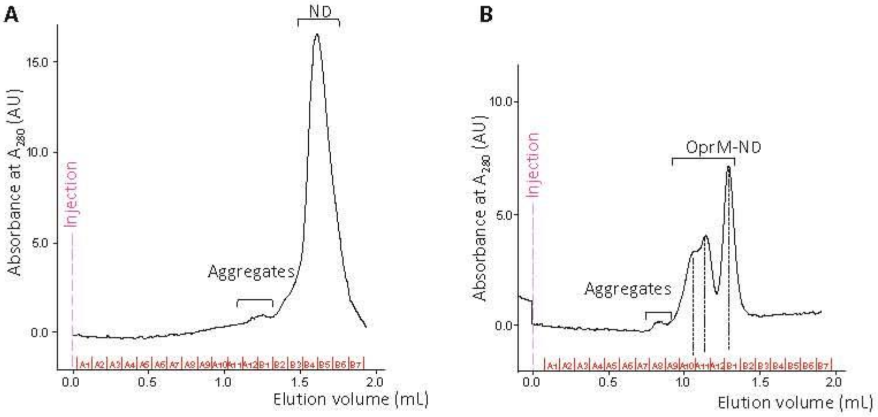

Fig. 3 Separation of OprM-ND population by SEC. (**a**) Elution profile from ND reconstitution with MSP. After detergent removal, the sample was injected onto a Superdex 200 PC 3.2/30 at a flow rate of 0.03 mL/min. The main peak (B4-B5 fractions) corresponds to NDs. (**b**) Elution profile of OprM-ND after assembly. After detergent removal, the sample was injected onto a Superdex 200 1 PC 3.2/30 column at a flow rate of 0.03 mL/min. Separated peaks corresponding to OprM-ND population were obtained and subsequently characterized by EM. *Dashed lines* in panel (**b**) indicate the fractions (A10, A11, B1) analyzed by EM in Fig. 4

1. Pre-equilibrate the column with 1 mL of SEC buffer.
2. Inject 60 μL OprM-ND sample.
3. Elute with 1.5 mL of SEC buffer.
4. Elution profile of protein was followed at 280 nm.
5. Peak fractions (100 μL) were collected and analyzed by EM.

3.7 2D Single-Particle Image Analysis

The single-particle analysis consists in (1) extracting subimages (particles), (2) aligning them (rotation and translation), and (3) calculating averages of homogeneous populations. As these procedures are intensively used in single-particle methods, we recommend the use of software usually devoted for these tasks. Here, examples of commands of SPIDER [15] are presented but other software like EMAN2 [16] can be used (Fig. 4).

1. *Extraction of subimages.* This initial step consists in selecting from the EM micrographs subimages containing each, one particle. For the sake of convenience during the 2D alignment process, the extracted subimages must be squared. For proteins exhibiting an elongated shape (like OprM), a larger bounding box is required. Particles are selected automatically using either the EMAN Boxer automatic selection tool (e2boxer.py) or any picking tools supporting Difference of Gaussians (DoG) filter that is very suitable to pick particles on negative staining micrographs (*see* **Note 6**). The output of this step is a collection of subimages, each containing one particle.
2. *2D Alignment of the subimages.* This step relies on a rotational and a translational alignment of the subimages using a so-called Reference-free alignment method. The latter consists in an iterative process using a floating temporary reference to align the images. Since this reference is always recalculated, it does not deeply influence the alignment process. In SPIDER, the commands AP RA (rotational alignment) and AP SA (translational alignment) are repeated during eight cycles.
3. *Principal component analysis.* This step consists in the classification of aligned subimage collection to sort out homogeneous populations. It is first done by running a Principal Component Analysis (PCA) using the command CA S in SPIDER and by setting the option PCA.
4. *Cluster generation with K-means. K*-means is a statistical method enabling extracting K homogeneous clusters from a data collection (*see* **Note 7**). In the negative staining EM project, the number of clusters (*K* number) is estimated such as a cluster contains 50–100 subimages. For example, for a set of 500 aligned particles, K must be set to 10. In SPIDER, the command CL KM takes as input the IMC file previously generated during the PCA step and by setting an appropriate K number.
5. *Average computation from the homogeneous clusters.* Finally, for each cluster created during the *K*-means step, an average image is calculated using the SPIDER command AS S.

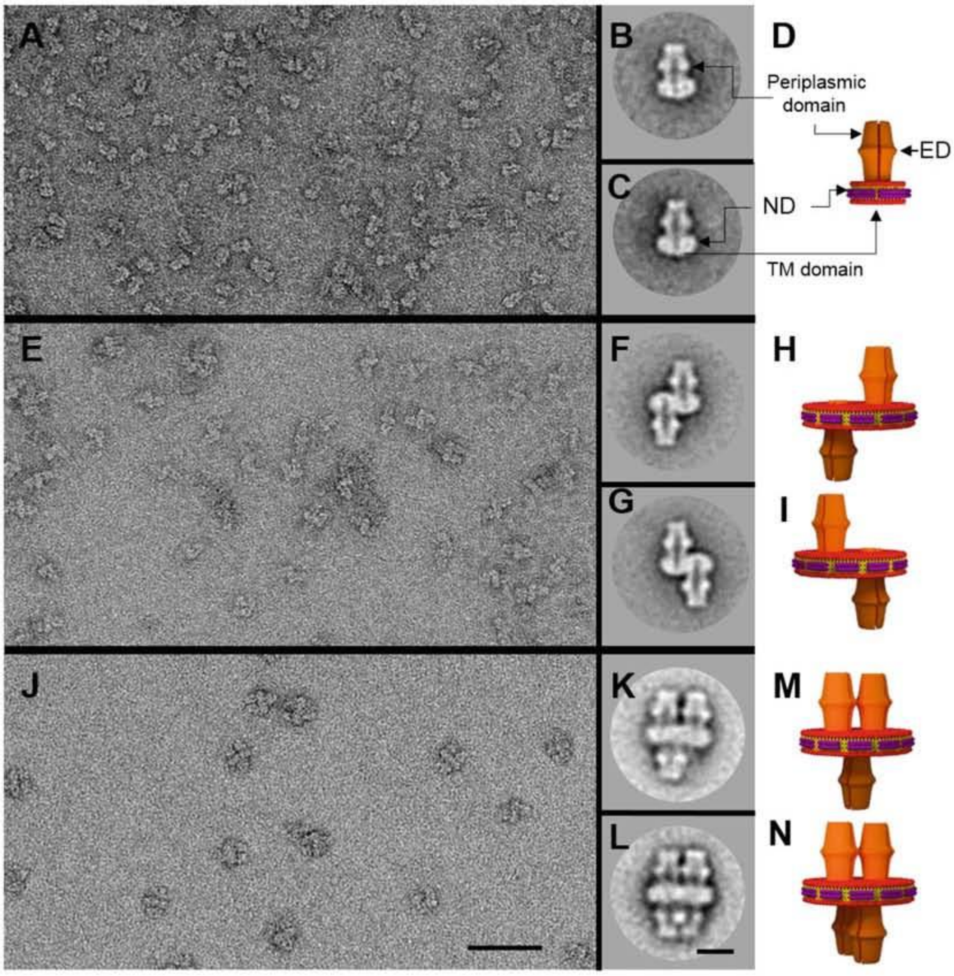

Fig. 4 EM analysis of OprM-ND fractions. *Upper row* (*A–D*) EM of B1 fraction. (*A*) Negative-stained micrograph. (*B*, *C*) Two typical image averages calculated from 76 (*B*) and 57 images (*C*) respectively (over a total of 4750 selected particles) showing one OprM molecule per ND. OprM-ND revealed a 11 nm in diameter ND spanned by a duct formed by the transmembrane β-barrel domain (TM), visible due to the presence of uranyl acetate within the β-barrel and, followed by the 10-nm-long periplasmic domain including the equatorial domain (ED) (*D*). *Middle row* (*E–I*) EM of A11 fraction. (*E*) Negative-stained micrograph exhibiting a vast majority of two OprM molecules per ND. (*F*, *G*) Among 404 selected particles, averages of two clusters of 105 (*F*) and 132 images (*G*) respectively differing in a 180° rotation about a vertical axis. The two OprM molecules are inserted on opposite sides of ND, as schematically drawn in (*H*) and (*I*). *Lower row* (*J–N*) EM of A10 fraction. (*J*) Negative-stained micrograph exhibiting a majority of OprM-ND containing several OprM molecules. (*K*, *L*) From 774 selected particles, typical average images of 59 (*K*) and 60 images (*L*) revealing OprM-ND containing three and four OprM molecules respectively as schematically drawn in (*M*) and (*N*)

4 Notes

1. Among the available MSPs, MSP1D1 is the shortest. The others have extra α helices designed to increase the ND diameter to accommodate large IMPs. The choice of MSP should be guided by the diameter of the transmembrane part of IMP. As a simple rule, the size of the latter should be less than that of ND made with the selected MSP. For OprM the β barrel domain is about 7 nm while ND are 9–10 nm in diameter.
2. Long-time conservation of MSP: Our recommendation to maintain an optimal efficacy of ND production is to use MSP as fresh as possible. From our feedback, MSP stock at −80 °C was useable for only three months. Beyond this delay, the quality of ND production starts to decrease.
3. In practice, as shown here, ND diameters have been remarkably expended by the incorporation of more than one molecule per ND, exhibiting a more extended conformational adaptability than the one described in [3]. Therefore in addition to the MSP length, its conformational flexibility is also a parameter to deal with for membrane protein reconstitution into ND.
4. Long-time preservation of OprM-ND: When OprM was reconstituted in ND, it can be stored over months at 4 °C without notable protein destabilization or aggregation. Protein in ND looks apparently very stable and possibly more than in detergent.
5. According to the literature, the production of ND only containing lipids is very reproducible with a regular diameter. The insertion of an integral membrane protein imposes additional constraints on ND diameter. ND diameter is slightly larger in the presence of MP exhibiting a conformational adaptability of MSP.
6. The automatic picking works well when the sample is well spread on the EM grid, meaning that the particles should not be close to each other. When the automatic picking fails, the particle selection should be done manually.
7. Defining the optimal *K* number may require several attempts. It is recommended to perform several times the "cluster generation" step with different *K* values. Clusters should exhibit discernible features or different orientations of the particle.

Acknowledgments

The authors would like to thank Drs. Isabelle Broutin and Martin Picard for providing purified OprM protein sample. Celine